REPUBLIC OF TURKEY
YILDIZ TECHNICAL UNIVERSITY
GRADUATE SCHOOL OF NATURAL AND APPLIED SCIENCES

LINEAR MATRIX INEQUALITY BASED ROBUST CONTROL FOR MULTI DEGREES OF FREEDOM HYBRID ELECTROMAGNETIC VIBRATION ISOLATION

Barış Can YALÇIN

DOCTOR OF PHILOSOPHY THESIS
Department of Mechatronics Engineering
Program of Mechatronics Engineering

Advisor
Assoc. Prof. Dr. Kadir ERKAN

October, 2019

REPUBLIC OF TURKEY
YILDIZ TECHNICAL UNIVERSITY
GRADUATE SCHOOL OF NATURAL AND APPLIED SCIENCES

LINEAR MATRIX INEQUALITY BASED ROBUST CONTROL FOR MULTI DEGREES OF FREEDOM HYBRID ELECTROMAGNETIC VIBRATION ISOLATION

A thesis submitted by Barış Can YALÇIN in partial fulfillment of the requirements for the degree of **DOCTOR OF PHILOSOPHY** is approved by the committee on 24.10.2019 in Department of Mechatronics Engineering, Program of Mechatronics Engineering.

Assoc. Prof. Dr. Kadir ERKAN
Yildiz Technical University
Advisor

Approved By the Examining Committee

Assoc. Prof. Dr. Kadir ERKAN, Advisor
Yildiz Technical University   _____

Asst. Prof. Dr. Hüseyin ÜVET, Member
Yildiz Technical University   _____

Prof. Dr. Selim SİVRİOĞLU, Member
Gebze Technical University   _____

Asst. Prof. Dr. Muhammet GARİP, Member
Yildiz Technical University   _____

Asst. Prof. Dr. Korhan KAYIŞLI, Member
Nişantaşı University   _____

I hereby declare that I have obtained the required legal permissions during data collection and exploitation procedures, that I have made the in-text citations and cited the references properly, that I haven't falsified and/or fabricated research data and results of the study and that I have abided by the principles of the scientific research and ethics during my Thesis Study under the title of Linear Matrix Inequality based Robust Control for Multi Degrees of Freedom Hybrid Electromagnetic Vibration Isolation supervised by my supervisor, Assoc. Prof. Dr. Kadir ERKAN. In the case of a discovery of false statement, I am to acknowledge any legal consequence.

Barış Can YALÇIN

Signature

Dedicated to my family

ACKNOWLEDGEMENTS

I am grateful to my family, who has provided me through moral and emotional support in my life. I am also grateful to my friends and Ph.D. advisor who have supported me along the way.

<div align="right">Barış Can YALÇIN</div>

TABLE OF CONTENTS

LIST OF SYMBOLS

$\mathcal{H}_2$ 2-Norm of Relevant System in Frequency Domain

$\mathcal{H}_\infty$ The Maximum Singular Value of $G(j\omega)$ for $\omega \geq 0$.

LIST OF ABBREVIATIONS

CDM   Coefficient Diagram Method

DoF   Degree of Freedom

FEM   Finite Element Method

LMI   Linear Matrix Inequality

PD   Proportional-Derivative

PID   Proportional-Integral-Derivative

IPD   Integral-Proportional-Derivative

LIST OF FIGURES

LIST OF TABLES

Linear Matrix Inequality based Robust Control for Multi Degrees of Freedom Hybrid Electromagnetic Vibration Isolation

Barış Can YALÇIN

Department of Mechatronics Engineering
Doctor of Philosophy Thesis

Advisor: Assoc. Prof. Dr. Kadir ERKAN

Vibration isolation systems based on hybrid electromagnets, consisting of electromagnets and permanent magnets, have potential usage in many industrial fields, such as clean room design, stewart platform design, transportation, semiconductor manufacturing, suspension systems, and robotic surgery etc. due to providing mechanical contact free vibration isolation. Besides, a simple electromagnet has the ability of acting as if it is virtual spring or damping element.

Using permanent magnets in the electromagnet structure has some crucial advantages, such as a minimized volume and a more compact structure. Furthermore, the necessary equalizer force for levitation can be generated by only the permanent magnet(s), which means, by using hybrid electromagnets, magnetic levitation can be achieved with considerably low energy consumption against different disturbance characteristics. This property is called zero-power behavior. However, the main problems of magnetic levitation process is that it has highly nonlinear nature. Even if it can be linearized, it has unstable pole(s), which makes the system vulnerable in terms of stability.

In recent years, linear matrix inequality-based design of controllers has received considerable attention and become very popular due to their ability to satisfy multi-objective requirements. Yet, LMI based $\mathcal{H}_2$ state-feedback controllers, having gap, acceleration, current and voltage values in state-vector, for a 3-DoF vibration isolation stage having 4-pole hybrid electromagnets, have not been investigated so

far. In the thesis, it has been studied whether there is a convex solution space for Lyapunov matrix inequalities to deal with multi-directional mechanic disturbances. LMI type of controller is structured to minimize the influence of both ground and direct disturbances varying at different magnitudes and frequencies on vibration isolation, zero-power, and protection of the levitation purposes. Moreover, the experimental setup used in this thesis has been designed to meet aforementioned purposes. The setup's design parameters of the experimental setup are explicitly given and the effectiveness of the proposed method is shown with the experimental results.

Keywords: Zero-power, pseudo-infinite stiffness, magnetic levitation, vibration isolation, linear matrix inequalities

ÖZET

Çok Serbestlik Dereceli Melez Elektromanyetik Titreşim İzolasyonu için Doğrusal Matris Eşitsizliği Tabanlı Gürbüz Kontrol

Barış Can YALÇIN

Mekatronik Mühendisliği Anabilim Dalı
Doktora Tezi

Danışman: Doç. Dr. Kadir ERKAN

Kalıcı mıknatıs ve elektromıknatıstan oluşan melez elektromıknatıs tabanlı titreşim izolasyon sistemleri, mekanik temassız titreşim izolasyonu özelliğinden ötürü temiz oda tasarımı, stewart platformu tasarımı, taşımacılık, yarı-iletken imalatı, süspansiyon sistemleri, robotik cerrahi vb. bir çok endüstriyel alanda kullanım potansiyeline sahiptir. Dahası, bir elektromıknatıs sanal bir yay ya da sönüm elemanı gibi davranabilme özelliğine sahiptir.

Kalıcı mıknatısları elektromıknatıs yapısında kullanmak ürün hacmini minimize etmek ve ürün yapısını daha kullanışlı hale dönüştürmek gibi bir çok önemli avantajı beraberinde getirmektedir. Dahası, levitasyon için gerekli olan dengeleyici kuvvet de yalnızca kalıcı mıknatıslar tarafından sağlanabilmektedir. Bu durum şu anlama gelmektedir; kalıcı mıknatısların kullanılmasıyla birlikte farklı bozucu karakteristiklerine karşı minimum enerji tüketimi gerçeklenebilir. Bu özellik sıfır-güç davranışı olarak isimlendirilmektedir. Fakat, bu noktadaki temel sorun manyetik levitasyonun yüksek mertebeden doğrusal olmayan doğasıdır. Doğrusallaştırma işlemi uygulansa bile, elde edilen doğrusal model sistemi kararlılık açısından savunmasız bırakan kararsız kutup veya kutuplara sahip olmaktadır.

Geçtiğimiz senelerde, doğrusal matris eşitsizliği tabanlı kontrolcüler kayda değer derecede ilgi görmüş ve bir çok amaca aynı anda hizmet edebilmelerinden ötürü popüler hale gelmiştir. Buna rağmen, hava aralığı, ivme, akım ve voltaj parametrelerini durum olarak kullanan LMI tabanlı $\mathcal{H}_2$ tam durum-geribeslemeli

kontrolcü ile çalışan, 3-serbestlik dereceli 4-kutuplu melez elektromıknatıs içeren titreşim izolasyon sistemleri ile ilgili bir çalışma yapılmamıştır. Tez kapsamında, mekanik çok-yönlü bozucuların bastırılmasında kullanılan ve Lyapunov matris eşitsizlikleri ile tanımlanan parametreler için konveks bir çözüm kümesi olup olmadığı incelenmiştir. LMI tipi kontrolcüler hem zeminden gelen hem de sistemin doğrudan üzerine uygulanan farklı büyüklük ve frekanstaki bozucuların titreşim izolasyonu, sıfır-güç ve levitasyon üzerindeki etkilerini minimize etmek için kullanılmıştır. Dahası, tez kapsamında kullanılan deney seti, yukarıda belirtilen hedefleri karşılamak için tasarlanmıştır. Deney setinin tasarım parametreleri açık bir şekilde verilmiş ve önerilen kontrolcü yapısının etkinliği deneysel sonuçlar ile desteklenmiştir.

Anahtar Kelimeler: Sıfır-güç, sözde-sonsuz sertlik, manyetik levitasyon, titreşim izolasyonu, doğrusal matris eşitsizlikleri

Introduction

1.1   Literature Review

1.1.1   Vibration Isolation Perspective

In the vibration isolation topic, two types of disturbances exist (Hoque et al. 2011), (Md. Emdadul Hoque and Takasaki 2010). First type is *direct disturbance*; it occurs by the force directly applied on the isolator stage. Second type is *ground induced disturbance*; it occurs by the vibrations that come from the ground. These disturbances can somehow be absorbed using passive suspension systems (C. Liu et al. 2015). However, at this point, many performance and sustainability problems may pop up. The main reason is the existence of this inevitable trade-off, since the both disturbances cannot be rejected at the same time by a simple passive suspension system. If a suspension design is stiff enough to handle direct disturbances, ground disturbance isolation performance of the system decreases. If a suspension design is soft enough to suppress ground disturbances, it is not able to cope with direct disturbances. In the light of above discussions, an active suspension system is needed to achieve satisfactory disturbance attenuation performance (Shahadat et al. 2010).

Consider the system shown in Fig.1.1 below. The spring hangs in a streched position because of the mass. When an external downward force is applied to the mass, the spring moves downward. This is the definition of positive stiffness. A hybrid electromagnet system can be controlled as if it is a spring which performs negative stiffness behavior as shown in Fig.1.2. When external downward force is applied to the levitated mass, vertical position change is measured by a sensor, and electromagnets are driven based on a specific control law. So far, the definition of negative stiffness and how to obtain it by using a hybrid electromagnet are explained. The question is; how can negative stiffness be used for vibration isolation purpose? This question is answered in the system shown in Fig. 1.3 below. A spring that shows positive stiffness behavior is serially connected to a spring that shows negative stiffness behavior.

Equivalent spring coefficient in Fig. 1.3 is equal to;
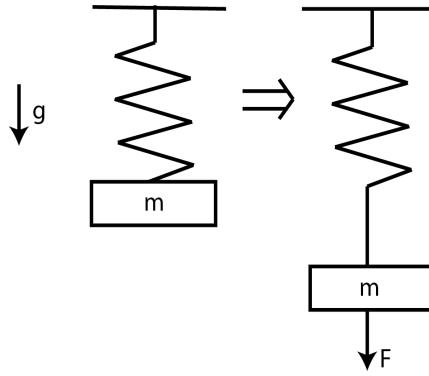
Figure 1.1 Positive stiffness
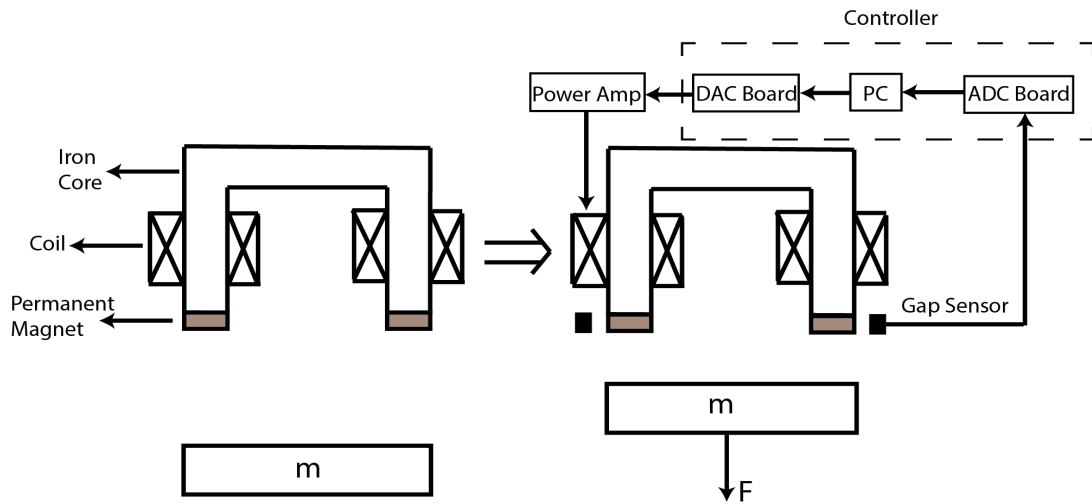
Figure 1.2 Negative stiffness
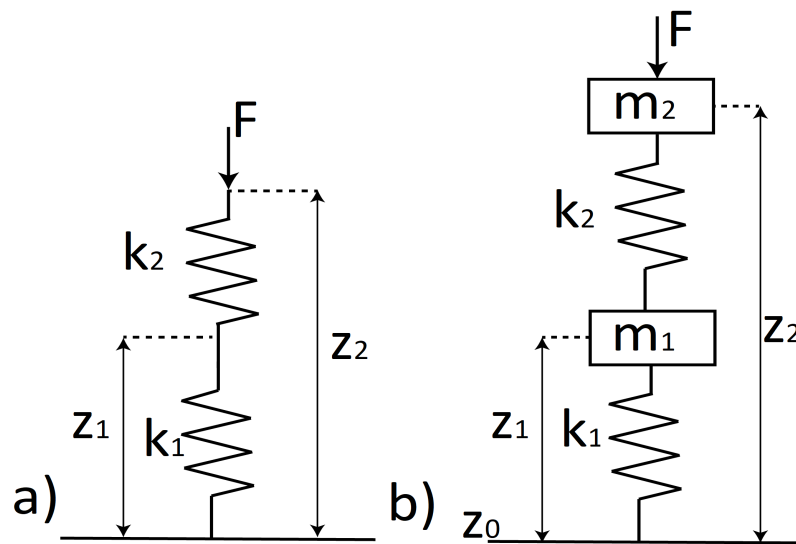
Figure 1.3 Obtaining infinite stiffness in theory

$$k_e = \frac{k_1 k_2}{k_1 + k_2} \tag{1.1}$$

For

$$k_1 = -k_2 \tag{1.2}$$

Equivalent spring coefficient becomes;

$$k_e = \infty \tag{1.3}$$

At this point, a simple question pops up, what would be the states of a levitation system acting as if it were a negative stiffness spring. This issue has been made clear in Section 2, Subsection 2.3.1.

Permanent magnets behave as if they were additional current-source equivalents (Zhu et al. 2015). However, electromagnet and permanent magnet models both have highly nonlinear natures (Ahn, Hwang, and Nguyen 2017), which means that; the whole system may show undesired performance under varying magnitude and frequency disturbances. Disturbances enforce the levitation gap moves away from its linearization or operating point. Unless the levitation gap is ensured, the system tends to fall down or stick up. Consequently, the performance requirements, such as vibration isolation and zero-power property, cannot be satisfied as well, unless there is an advanced controller structure.

1.1.2 Classical Maglev Systems

For classical maglev systems, stabilization for position control can partially be achieved by using a PD-type controller. However, employment of a PD controller is a primitive approach since this type of controller adds a zero to the closed-loop transfer function which makes the system positive phase. When a system becomes positive phase, it amplifies all high-frequency inputs to the infinity. Furthermore, tracking performance of a PD-type controller is not satisfying. Because of these reasons, a more qualified controller structure is needed (Unni et al. 2016), (Adina et al. 2016).

There are other types of controller structures that may be applicable to resolve the outlined issues. Even though sliding-mode-based controllers may be seen as one of the good alternatives , it suffers from the chattering effect. Robust control strategies, such as super-twisting algorithm of second-order sliding mode control or backstepping sliding mode control, can greatly weaken the system chattering (Chunfang and Jian 2012), (Chiang et al. 2013). However, these algorithms mostly reduce the linearized

working space of the maglev system and require high-frequency sampling time with precise measurements.

To investigate possible advantages and disadvantages of using sliding mode control for a classical maglev system, a simulation study about first-order integral sliding mode control of a magnetically levitated 4-pole hybrid electromagnet was conducted by (Ertugrul and Erkan 2016). For reference tracking performance, it was observed that high overshoot and settling time occurred, while the system became robust against unmodelled uncertainties and external disturbances. Noise rejection is another problem for highly nonlinear maglev applications. Even though simulations may give excellent noise rejection outputs, experimental results mostly do not show the same performance.

Lack of well-organized techniques and demand for high computation capacity are the drawbacks of fuzzy logic originated approaches (Erkan and Koseki 2006), (Su and Li 2016), (A. Kumar and Kumar 2015), (Nath, Samantaray, and Chaudhury 2015). Adaptive and optimal robust control techniques without toolboxes require high mathematical skills and are not eligible for field engineers, since the industry is still inclined towards classical control design (Baig and Mahmood 2016), (Rodriguez, Siguerdidjane, and Ortega 2000), (Sarmad et al. 2016), (Zhang, Xian, and Ma 2015), (Ahsan, Masood, and Wali 2013).

The well-known PID controller structure can stabilize the system with relatively satisfying tracking performance, but employment of classical PID structure on the forward path transfer function introduces a closed-loop zero near the origin, which results in a large overshoot appearing at the output (Singh and V. Kumar 2015), (Atlihan, Bucak, and K. Erkan 2015), (Verma, Yadav, and Nagar 2015). This problem can be eliminated by using the I-PD configuration of PID structure (Atlihan, Bucak, and K. Erkan 2015).

CDM is an algebraic design applied to polynomial structure of the system on the parameter space, where a specific visual diagram is used to present and interpret the essential data. The basic idea of this method is to use the stability index and the equivalent time constant derived from the characteristic polynomial as the design basis (Coelho, Boaventura-Cunha, and Moura Oliveira 2015), (Ucar and Hamamci 2000), (Hamamci and Koksal 2003), (K. Erkan, Acarkan, and T. Koseki 2007), (K. Erkan, Okur, et al. 2011).

CDM is advantageous for classical maglev systems. However, due to the following reasons, it is not applicable for advance vibration isolation systems.

(i) Controllers can be designed for only a specific frequency band. Therefore, it is not possible to design $\mathcal{H}_2$ and $\mathcal{H}_\infty$ controllers and observers to deal with wide range of disturbances.

(ii) Modelling multi-input disturbances is hard to achieve.

(iii) Multi-objectivity for specific controller and observer designs is not possible.

To construct an advanced optimal robust controller structure having only positive sides of CDM for a vibration isolation system, LMI based controllers are good alternatives due to their compactness and design capabilities. Nowadays, rule based syntheses of LMIs can easily be modelled as optimality problems and be solved in polynomial time by many algorithms, such as Interior Point Method. Moreover, most of open-source solvers are available on the internet.

1.2 Objective of the Thesis

Single DoF electromagnets have been commonly utilized in many industrial applications to suspend ferromagnetic objects. However, control applications including more than one degree of freedom cannot be possible using a standard single DoF electromagnet (Yakushi, Koseki, and Sone 2000). To deal with this issue, 4-pole electromagnet structure has been proposed by many researches (Liu et al. 2000), (Jiangheng and Koseki 2001). This new electromagnet structure has control capacity in multi-degree of freedom with full redundancy. Each pole can generate electromagnetic force that is necessary for magnetic levitation. Energizing poles in a specific configuration allows any ferromagnetic object to move in a different axis of motion. So that, it is compatible for many engineering applications requiring complex movements.

In last few decades, LMIs have been intensively used as a strong tool in the field of control theory. Many problems, such as $\mathcal{H}_2$ and $\mathcal{H}_\infty$ state feedback and dynamic output feedback controller synthesis (Yalçın, Sever, and Erkan 2018), analysis and design of robustness against parametric uncertainties (Tascikaraoglu 2014), and stability of time delay systems (Hakan Yazici and Parlakci 2012), can all be modelled as multi-objective problems that contain LMIs (Boyd et al. 1994), (Lofberg 2004), (Sturm 1999), (Nesterov and Nemirovskii 1994).

LMIs have recently been used to address few problems in magnetic levitation, such as disturbance rejection for position control of a simple levitated mass (Raja et al. 2015), gain-scheduling control for a magnetically levitated rotor (Wang, Cole, and Keogh

2017). However, a detailed study for a 3-DoF vibration isolation system that can both suppress direct and ground disturbances in LMI framework has not been considered so far. Therefore, for LMI controller design, it is aimed to meet multi-objective requirements which can be summarized as follows;

  (i) The levitation has to be protected while $\mathcal{H}_2$ norm between the disturbances and the levitation has to be minimized.

 (ii) The zero-power property has to be provided while $\mathcal{H}_2$ norm between the disturbances and the zero-power property has to be minimized.

(iii) Pseudo-infinite stiffness has to be created while $\mathcal{H}_2$ norm between the disturbances and pseudo-infinite stiffness has to be minimized.

Also, one should consider that; if the aim is vibration isolation, the three keypoints mentioned above have to be achieved at a wide range of frequency band, which means that; LMIs ensuring a minimized $\mathcal{H}_2$ norm need to be synthesized.

2

Mathematical Modelling of Vibration Isolator Stage

2.1 Hybrid Electromagnet Dynamics for Single Axis Levitation

In the analysis of a single coil, magnetic resistance, hysteresis of the iron core, eddy currents, flux leakage and fringing effects are assumed to be negligible. So that, the electromagnetic force for vertical direction is obtained as follows, (Erkan, Yalçın, and Garip 2017);

$$F_e(z, i) = \epsilon \left(\frac{i + I_m}{z + \ell_m / \mu_r} \right)^2 \tag{2.1}$$

Where, ϵ is the configuration parameter of the electromagnet, i is the coil current, $z = z_2 - z_1$ is the equivalent air gap parameter between the two masses, ℓ_m is the length of permanent magnets, μ_r is the relative permeability of the permanent magnet, I_m is the equivalent current representation of the permanent magnet. Nonlinear behavior of (2.1) is given in Fig. 2.1 by using experimental setup parameters shown in Table 1.
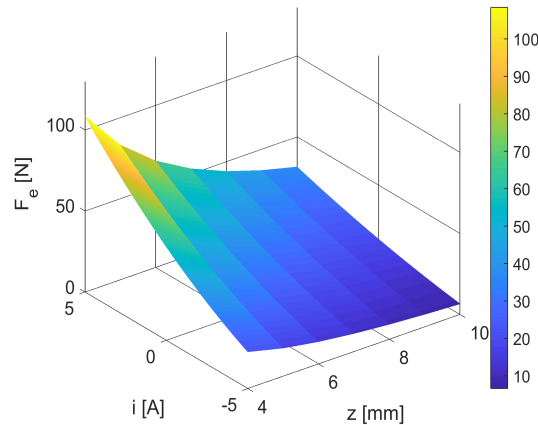
Figure 2.1 Nonlinear behavior of hybrid electromagnet attraction force on vertical motion

The levitation gap used in this study is 6 *mm*, and the zero-power property occurs around 0 *A*. Therefore, the linearization approach is applied to (2.1) around $z_0 = 0.006$ *m* and $i_0 = 0$ *A* as follows;

$$K_{z_0}(z_0, i_0) = \frac{\partial F_e}{\partial z_0} = -2\epsilon \frac{(i_0 + L_m)^2}{(z_0 + \ell_m/\mu_r)^3} \tag{2.2}$$

$$K_{i_0}(z_0, i_0) = \frac{\partial F_e}{\partial i_0} = 2\epsilon \frac{(i_0 + L_m)}{(z_0 + \ell_m/\mu_r)^2} \tag{2.3}$$

K_{z_0} is the gap factor and K_{i_0} is the current factor. Then, (2.1) can be approximated as

$$F_e(z, i) \cong K_{z_0}(z_0, i_0)\triangle z + K_{i_0}(z_0, i_0)\triangle i + F_e(z_0, i_0) \tag{2.4}$$

where z_0 and i_0 are the levitation gap and the coil current values at the linearization point, respectively. Therefore, due to permanent magnet, $F_e(z_0, i_0) = m_2 g$. $\triangle z = z - z_0$ is the difference between the actual levitation gap and the linearization point. According to Newton's second law, the rate of change of momentum of the levitated mass on the vertical axis can be written as follows;

$$m_2 \frac{d^2 z_2}{dt^2} = -F_e(z, i) + m_2 g + F_d \tag{2.5}$$

Here, m_2 is mass of the levitated object, g is the gravitational acceleration constant and F_d is the disturbance. Electrical dynamics of the system is given below.

$$\frac{di}{dt} = \frac{K_V}{L}\frac{dz}{dt} - \frac{R}{L}i + \frac{1}{L}V \tag{2.6}$$

Here R is coil resistance, L is coil inductance, K_V/L is function of the gap factor and current factor as follows; $K_V/L = K_{z_0}(z_0, i_0)/K_{i_0}(z_0, i_0)$.

2.2 Isolator Dynamics

The two mass vibration isolation system combined with a hybrid electromagnet in Fig. 2 was firstly proposed by (Mizuno et al. 2007). In theory, a negative spring that is serially connected to a positive spring becomes a system that has pseudo-infinite stiffness. Therefore, the system shows robust behaviour against direct disturbances, whereas it has minimum oscilattion response against ground disturbances. With current and voltage parameters in state vector, magnetic levitation system can act as if it is negative spring (Mizuno et al. 2007).
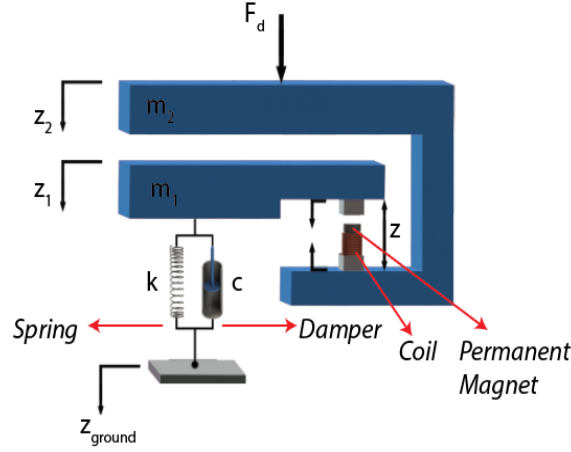
Figure 2.2 Symbolic representation of single DoF, two mass vibration isolation system

$$m_1 \frac{d^2 \triangle z_1}{dt^2} + c \left(\frac{d \triangle z_1}{dt} - \frac{d \triangle z_{ground}}{dt} \right) + k(\triangle z_1 - \triangle z_{ground})$$
$$= K_{z_0} \triangle z + K_{i_0} \triangle i \qquad (2.7)$$

Here, $\triangle z_1$ and $\triangle z_2$ are the relative displacements from linearization point, $\triangle z = \triangle z_2 - \triangle z_1$. On the linearization point, $m_2 g$ term can be canceled by permanent magnet force. Therefore, (2.5) becomes;

$$m_2 \frac{d^2 \triangle z_2}{dt^2} = -K_{z_0} \triangle z - K_{i_0} \triangle i + F_d \qquad (2.8)$$

Here, m_2 is mass of the levitated object, g is the gravitational acceleration constant and F_d is the disturbance, $K_{z_0} = K_{z_0}(z_0, i_0)$ is the gap constant and $K_{i_0} = K_{i_0}(z_0, i_0)$ is the current constant. Electrical dynamics of the system is given below:

$$\frac{d \triangle i}{dt} = \frac{K_{z_0}}{K_{i_0}} \frac{d \triangle z}{dt} - \frac{R}{L} \triangle i + \frac{1}{L} \triangle V \qquad (2.9)$$

2.3   Control-Oriented State-Space Model for Single Axis Levitation

Any linear time-invariant system can be represented by a state-space framework.

$$\frac{dx}{dt} = Ax + B_1 u + B_2 w \qquad (2.10)$$

Here, $A \in \mathbb{R}^{n \times n}$ is the state matrix; $B_1 \in \mathbb{R}^{n \times r}$ is the control input matrix and $B_2 \in \mathbb{R}^{n \times p}$ is the exogenous input matrix which is used to describe effect of external signals such

as disturbance and reference trajectory. The highest order terms in equations (2.7), (2.8) and (2.9) are left alone on the left handside, and derivatives of (2.7), (2.8) are taken due to acceleration state feedback.

$$
\begin{aligned}
\frac{d}{dt}\frac{d^2 \triangle z_1}{dt^2} &= \frac{d}{dt}[-\frac{c}{m_1}\frac{d\triangle z_1}{dt} + \frac{c}{m_1}\frac{d\triangle z_{ground}}{dt} - \frac{k}{m_1}\triangle z_1 \\
&\quad + \frac{k}{m_1}\triangle z_{ground} + \frac{K_{z_0}}{m_1}\triangle z_2 \\
&\quad - \frac{K_{z_0}}{m_1}\triangle z_1 + \frac{K_{i_0}}{m_1}\triangle i] \quad\quad\quad (2.11) \\
\frac{d}{dt}\frac{d^2 \triangle z_2}{dt^2} &= \frac{d}{dt}[-\frac{K_{z_0}}{m_2}\triangle z_2 + \frac{K_{z_0}}{m_2}\triangle z_1 \\
&\quad - \frac{K_{i_0}}{m_2}\triangle i + \frac{1}{m_2}F_d] \quad\quad\quad (2.12) \\
\frac{d\triangle i}{dt} &= \frac{K_{z_0}}{K_{i_0}}\frac{d\triangle z_2}{dt} - \frac{K_{z_0}}{K_{i_0}}\frac{d\triangle z_1}{dt} - \frac{R}{L}\triangle i + \frac{1}{L}\triangle V \quad\quad\quad (2.13)
\end{aligned}
$$

2.3.1 LMI based $\mathcal{H}_2$ Disturbance Rejection with Zero-Power Controller

For obtaining LMI based $\mathcal{H}_2$ disturbance rejection with zero-power controller, state vector $x \in \mathbb{R}^n$ must be determined. The acceleration parameters of mass-1 and mass-2 are desired to asymptotically converge zero, and the system has to show zero-power behavior. Thus, the state vector can be written as

$$
x = \begin{bmatrix} \frac{d(z_{ref}-\triangle z)}{dt} & z_{ref}-\triangle z & \frac{d^2 \triangle z_1}{dt^2} & \frac{d^2 \triangle z_2}{dt^2} & \triangle i & \int(0-V)dt \end{bmatrix}^T \quad\quad (2.14)
$$

In (2.14), z_{ref} is the reference trajectory desired to be tracked by $\triangle z$. Then, the control input vector $u \in \mathbb{R}^r$ and the exogenous input vector $w \in \mathbb{R}^p$ are given as

$$
u = \triangle V, w = \begin{bmatrix} z_{ref} & \frac{d\triangle z_{ground}}{dt} & \frac{d^2 \triangle z_{ground}}{dt^2} & \frac{dF_d}{dt} & \frac{dz_1}{dt} \end{bmatrix}^T \quad\quad (2.15)
$$

By the use of (2.10-2.13), (2.14), and (2.15), the state space matrices are as follows

$$A = \begin{bmatrix} 0 & 0 & 1 & -1 & 0 & 0 \\ 1 & 0 & 0 & 0 & 0 & 0 \\ -\frac{2K_{z0}}{m_1} & 0 & -\frac{c}{m_1} & 0 & \frac{-K_{i0}R}{m_1 L} & 0 \\ \frac{2K_{z0}}{m_2} & 0 & 0 & 0 & \frac{K_{i0}R}{m_2 L} & 0 \\ -\frac{K_{z0}}{K_{i0}} & 0 & 0 & 0 & -\frac{R}{L} & 0 \\ 0 & 0 & 0 & 0 & 0 & 0 \end{bmatrix} \tag{2.16}$$

$$B_1 = \begin{bmatrix} 0 & 0 & \frac{K_{i0}}{Lm_1} & \frac{-K_{i0}}{Lm_2} & \frac{1}{L} & -1 \end{bmatrix}^T \tag{2.17}$$

$$B_2 = \begin{bmatrix} 0 & 0 & 0 & 0 & 0 \\ 0 & 0 & 0 & 0 & 0 \\ 0 & \frac{k}{m_1} & \frac{c}{m_1} & 0 & -\frac{k}{m_1} \\ 0 & 0 & 0 & \frac{1}{m_2} & 0 \\ 0 & 0 & 0 & 0 & 0 \\ 0 & 0 & 0 & 0 & 0 \end{bmatrix} \tag{2.18}$$

$$y = C_1 x + D_{11} u + D_{12} w = x \tag{2.19}$$

Here, $C_1 \in \mathbb{R}^{h \times n}$, $D_{11} \in \mathbb{R}^{h \times r}$ and $D_{12} \in \mathbb{R}^{h \times p}$ are measured output matrices with appropriate dimensions.

$$C_1 = I_{6 \times 6} \tag{2.20}$$

$$D_{11} = 0_{6 \times 1}, D_{12} = 0_{6 \times 5}, \tag{2.21}$$

In the controller design, effect of the exogenous inputs on some certain output variables is required to be minimized. The certain output variables are named as controlled outputs and shown as $\bar{z} \in \mathbb{R}^m$.

$$\bar{z} = C_2 x + D_{21} u + D_{22} w \tag{2.22}$$

Here, $C_2 \in \mathbb{R}^{m \times n}$, $D_{21} \in \mathbb{R}^{m \times r}$ and $D_{22} \in \mathbb{R}^{m \times p}$ are controlled output matrices with appropriate dimensions. Controlled outputs vector is supposed to be chosen carefully to satisfy performance requirements. Firstly, it is desired that mass-2 must be unaffected by disturbances to ensure vibration isolation property. Secondly, the levitation gap has to be protected to stay within linearized operating point. Finally, produced control signal and current variable need to be minimized to achieve zero-power property in both the absence and the presence of disturbances. Therefore,

the controlled output vector is written down as follows;

$$\bar{z} = \left[\begin{array}{c} \frac{d^2 \triangle z_2}{dt^2} + \triangle i + \int (0 - V) dt \end{array} \right] \tag{2.23}$$

$$C_2 = \left[\begin{array}{cccccc} 0 & 0 & 0 & 1 & 1 & 1 \end{array} \right] \tag{2.24}$$

$$D_{21} = 0, D_{22} = 0_{1x5} \tag{2.25}$$

2.4 4-Pole Hybrid Electromagnet Structure

Three virtual winding currents are defined as i_z , i_α , and i_β . These parameters represent a sort of average current working for only one axis (z , α, or β). This assumption gives an opportunity for controlling each degree of freedom while controlling i_1 , i_2 , i_3 , and i_4 independently.
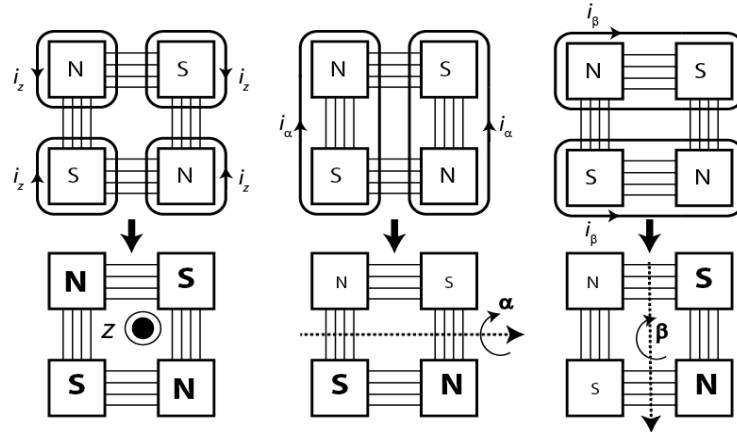
Figure 2.3 Energizing coils

Controlling the system for translational movement along positive z, i_1 , i_2 , i_3 , and i_4 have to be positive and their average value is calculated in (2.26).

Controlling the system for rotational movement around positive α, i_1 and i_4 have to be negative, while i_2 and i_3 have to be positive and their average value is calculated in (2.27).

Controlling the system for rotational movement around positive β, i_1 and i_2 have to be negative, while i_3 and i_4 have to be positive and their average value is calculated in (2.28).

$$i_z = \frac{1}{4}(i_1 + i_2 + i_3 + i_4) \tag{2.26}$$

$$i_\alpha = \frac{1}{4}(-i_1 + i_2 + i_3 - i_4) \tag{2.27}$$

$$i_\beta = \frac{1}{4}(-i_1 - i_2 + i_3 + i_4) \tag{2.28}$$

$$\begin{bmatrix} i_1 \\ i_2 \\ i_3 \\ i_4 \end{bmatrix} = \begin{bmatrix} 1 & -1 & -1 \\ 1 & 1 & -1 \\ 1 & 1 & 1 \\ 1 & -1 & 1 \end{bmatrix} \begin{bmatrix} i_z \\ i_\alpha \\ i_\beta \end{bmatrix} \tag{2.29}$$

In the second row of Fig. 2.3, it is implied that bold and bigger characters are energized coils; however, the system behaves as if coils are being energized with some virtual winding currents as shown in the first row.

z_1 z_2, z_3 and z_4 are translational air gaps parameters of coils, α and β are rotational air gap parameters.

$$z = \frac{1}{4}(z_1 + z_2 + z_3 + z_4) \tag{2.30}$$

$$\alpha = \frac{1}{2b}\left(\frac{z_1 + z_4}{2} - \frac{z_2 + z_3}{2}\right) \tag{2.31}$$

$$\beta = \frac{1}{2b}\left(\frac{z_1 + z_2}{2} - \frac{z_3 + z_4}{2}\right) \tag{2.32}$$

(2.4) evolves for each axis.

$$F_z(z, i_z) \cong K_{z_0}(z_0, i_{z0})\triangle z + K_{i_{z0}}(z_0, i_{z0})\triangle i_z + F_e(z_0, i_{z0}) \tag{2.33}$$

$$T_\alpha(\alpha, i_\alpha) \cong K_{\alpha_0}(\alpha_0, i_{\alpha0})\triangle\alpha + K_{i_{\alpha0}}(\alpha_0, i_{\alpha0})\triangle i_\alpha + T_\alpha(\alpha_0, i_{\alpha0}) \tag{2.34}$$

$$T_\beta(\beta, i_\beta) \cong K_{\beta_0}(\beta_0, i_{\beta0})\triangle\beta + K_{i_{\beta0}}(\beta_0, i_{\beta0})\triangle i_\beta + T_\beta(\beta_0, i_{\beta0}) \tag{2.35}$$

2.5   4-Pole Hybrid Electromagnet Geometry

FEM Analysis has been conducted to determine geometric parameters in Fig. 2.5. To do that, ANSYS Maxwell with ANSYS Genetic Algorithm Optimization Toolbox have been used (Rosu et al. 2018), (PADT, Miller, and Strain 2016). The levitated mass is considered to be 5 kg and coils are considered to be 200-$turn$. Electromagnet's geometric parameters and linearization point for (2.1) are optimized to provide necessary levitation force without magnetic saturation.
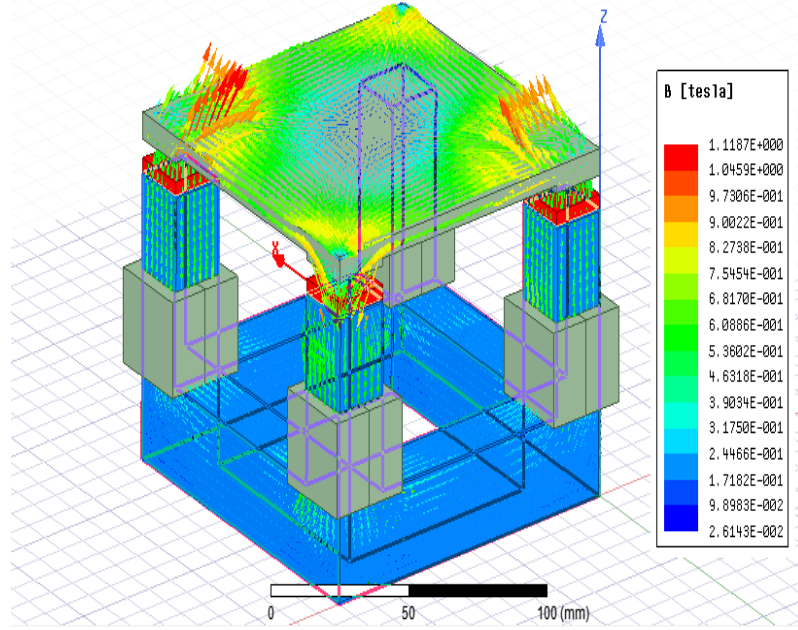
Figure 2.4 FEM Analysis

During the scenarios with vibrations or without vibrations, magnetic saturation should not exist. Otherwise, hybrid electromagnet cannot produce the necessary force for suspending the ferromagnetic object. Detalied analysis results showing force - levitation gap - current, torque - levitation gap - current and magnetic field - levitation gap - current relations are given by Table A.1, Table A.2 and Table A.3, respectively, in Appendix-A. Due to the geometric symmetry, T_α and T_β are identical. Therefore, there is only one table including torque in Appendix-A.

Permanent magnets bring considerable cost to levitation systems. Thus, volume of permanent magnets should be as minimal as possible. In this thesis, Nd35 neodymium permanent magnet with 20x20x2 mm^3 volume is chosen for 4-pole hybrid electromagnet structure.

At linearization point, levitation can be achieved by using only permanent magnets to achieve zero-power property. Therefore, linearization point has to be chosen by considering both magnitude of levitated mass and gap sensor constraints. In Fig. 2.6, it can be seen that zero-power property for 50 N load can be obtained around 6 mm.

14
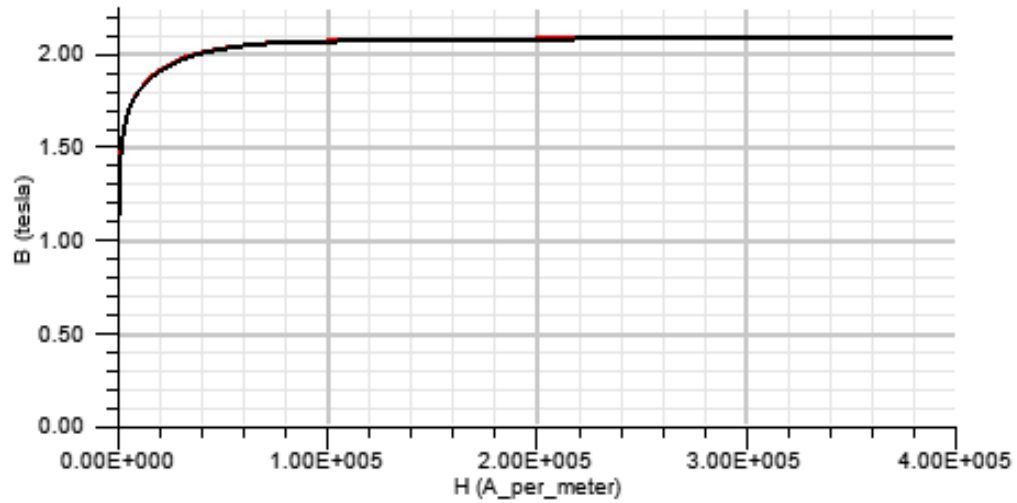
Figure 2.5 B-H curve of stainless steel
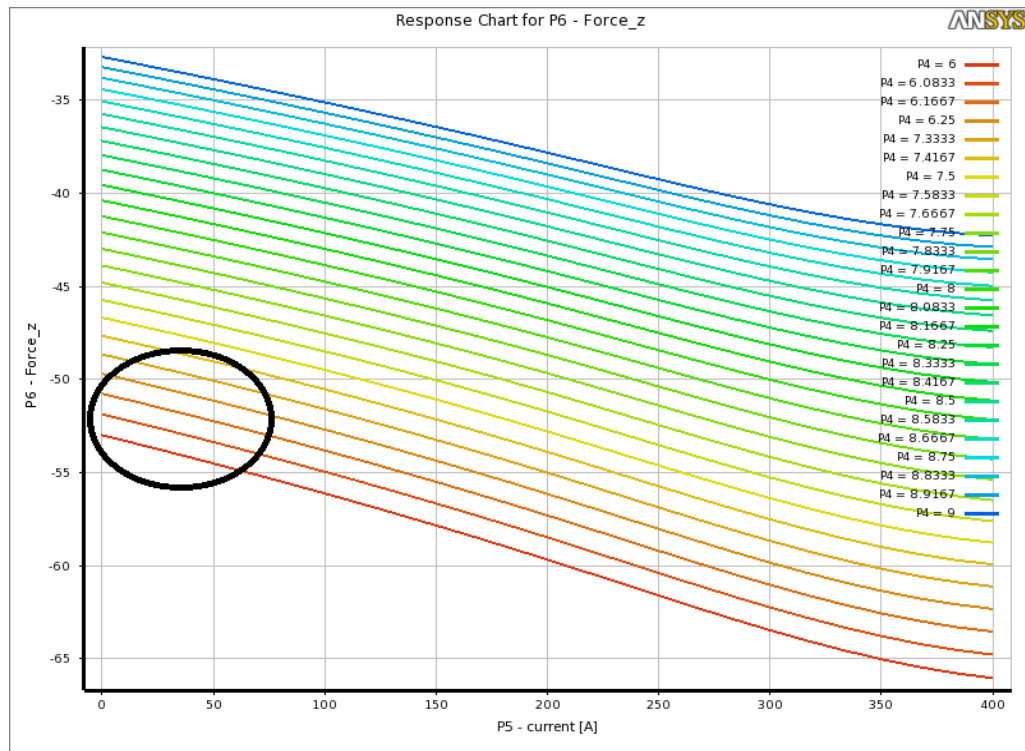
Figure 2.6 Choosing linearization point

Geometric parameters obtained from ANSYS Maxwell with ANSYS Genetic Algorithm Optimization Toolbox are given in Fig. 2.7, Fig. 2.8 and Table 2.1.

Table 2.1 Geometric parameters for 4-pole hybrid electromagnet

Parameter	Value
a	125 mm
b	27 mm
c	50 mm
d	20 mm

15
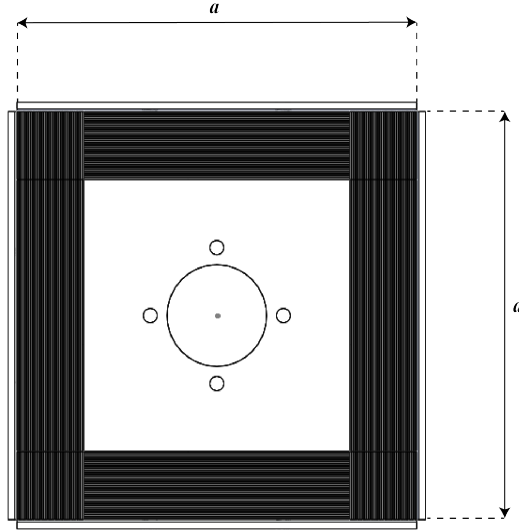
Figure 2.7 Top view of electromagnet
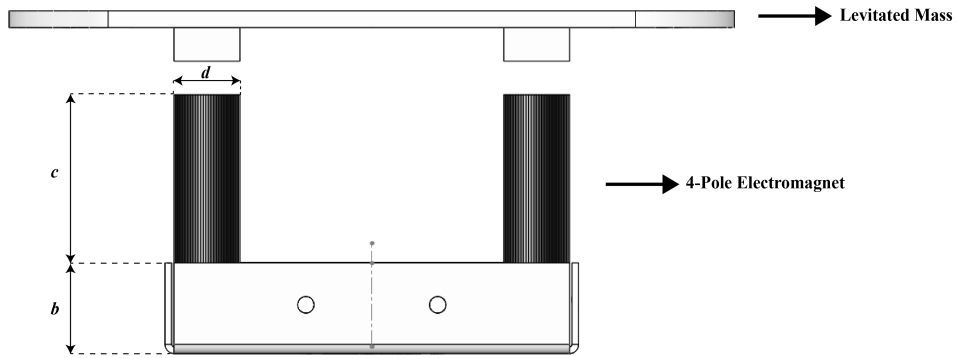
Figure 2.8 Front view of electromagnet

Silicon carbide sheets are assembled to create electromagnet core in Fig. 2.9.
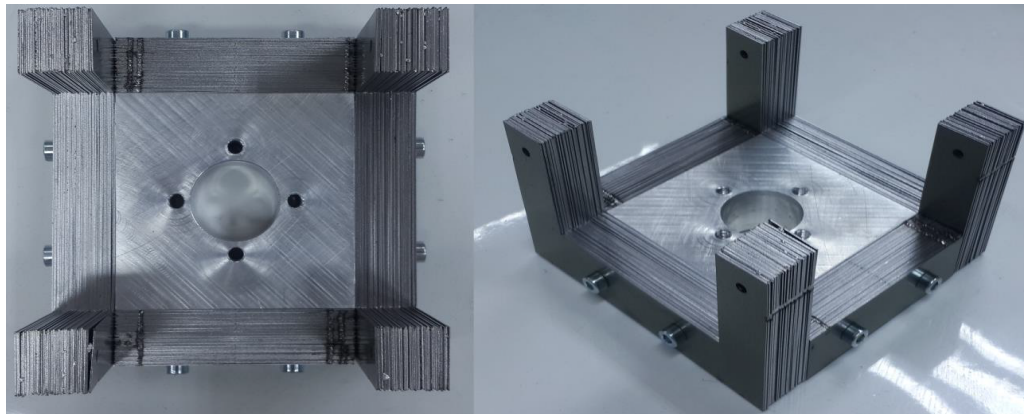
Figure 2.9 Assembled electromagnet core

Another advantage to choose linearization point at which only permanent magnets can provide necessary force to suspend the levitated mass is that; a 4-pole electromagnet can perform 3-DoF motion as mentioned before. During 3-DoF motion, coupling effects occur between axes. These effects are minimized around zero-power point.

FEM analysis result showing this issue is given in Fig. 2.10.
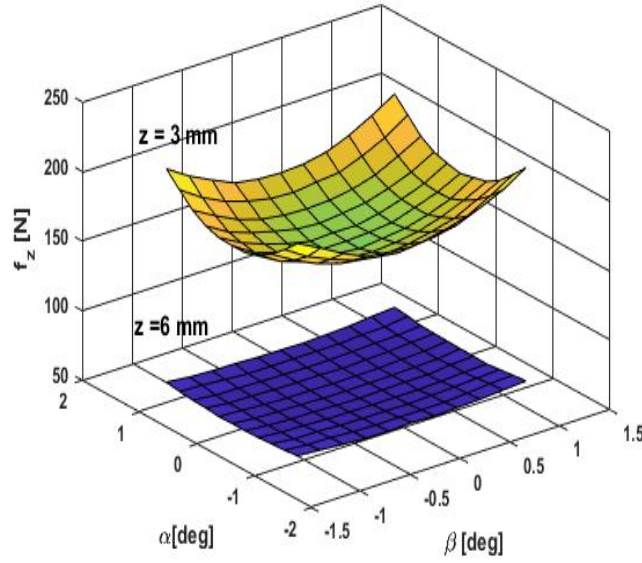
Figure 2.10 Coupling effects

In literature, coefficients in (2.33) is obtained by drop-test experiment. Tangents occurring at dropping instant in current-time and gap-time plots give these coefficients as shown in Fig. 2.11 and Fig. 2.12. In these figures, x and y axis parameters in encircled areas are being evaluated in a linear regression approach to derive a first order linear model. And then, tangent of this first order linear model is calculated to obtain the coefficients. However, conducting experiments to find coefficients in (2.34) and (2.35) are physically not that easy. These coefficients are mostly obtained from FEM analysis as shown in Fig. 2.13 and Fig. 2.14. $K_{i_{\alpha 0}}$ is obtained from (T_α/α), $K_{i_{\alpha 0}}$ is obtained from (T_α/i_α). Whereas, $K_{i_{\beta 0}}$ is obtained from (T_β/β), $K_{i_{\beta 0}}$ is obtained from (T_β/i_β).

Coil calibration have been conducted to obtain sensitive resistance and inductance parameters changing at different current values produced by current driver board.
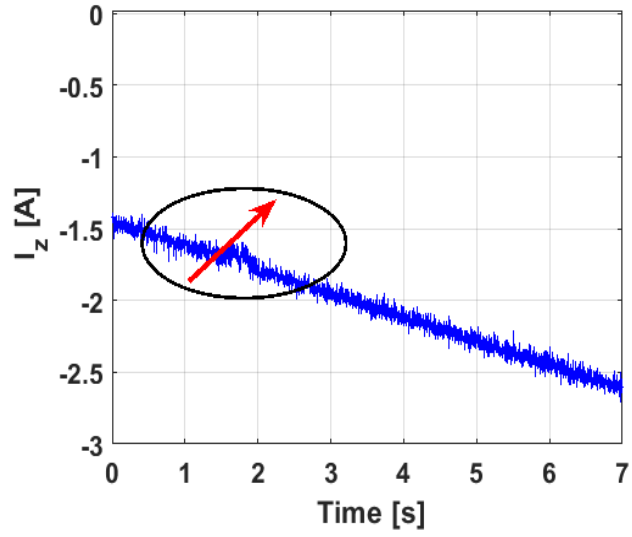
Figure 2.11 Tangent in current-time plot
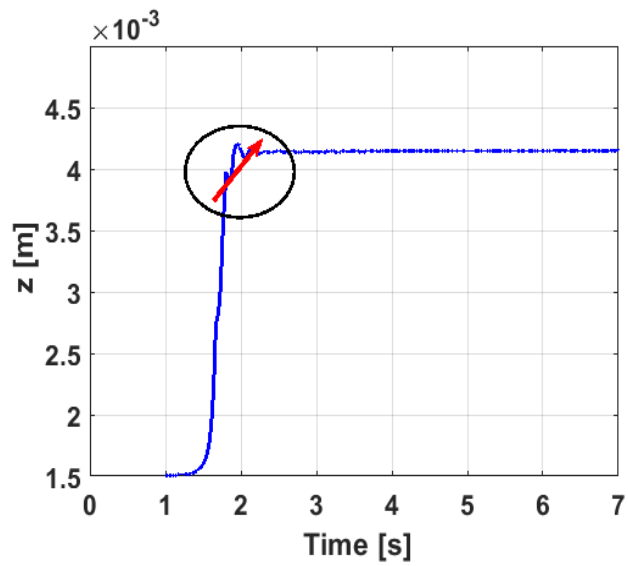
Figure 2.12 Tangent in gap-time plot

Figure 2.13 α axis parameters

18
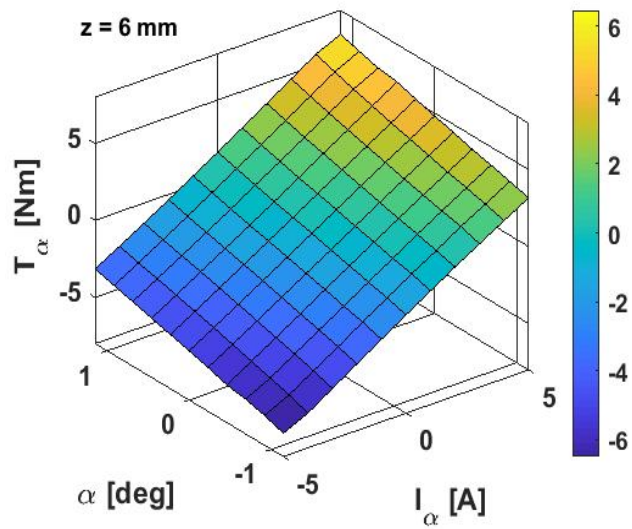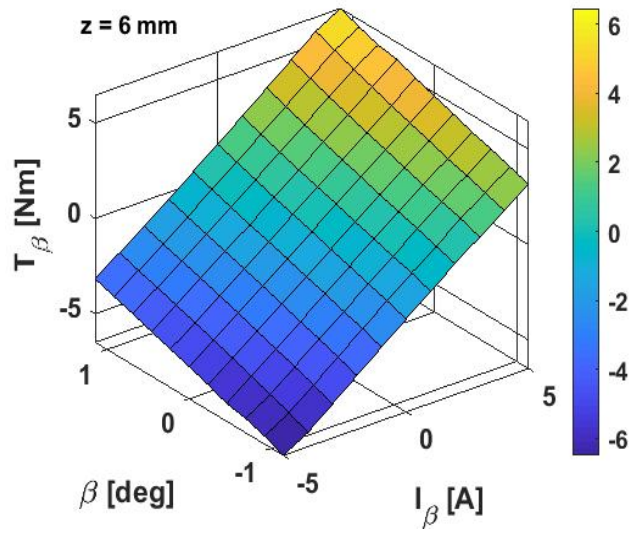
Figure 2.14 β axis parameters
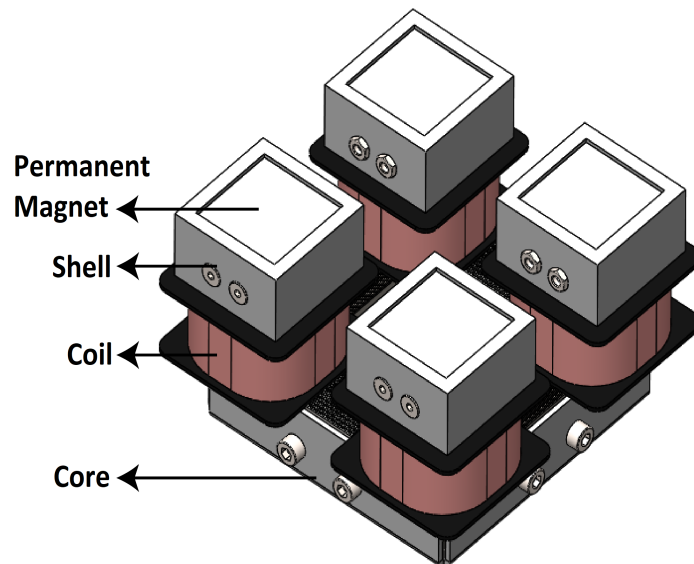
Figure 2.15 4-Pole CAD model
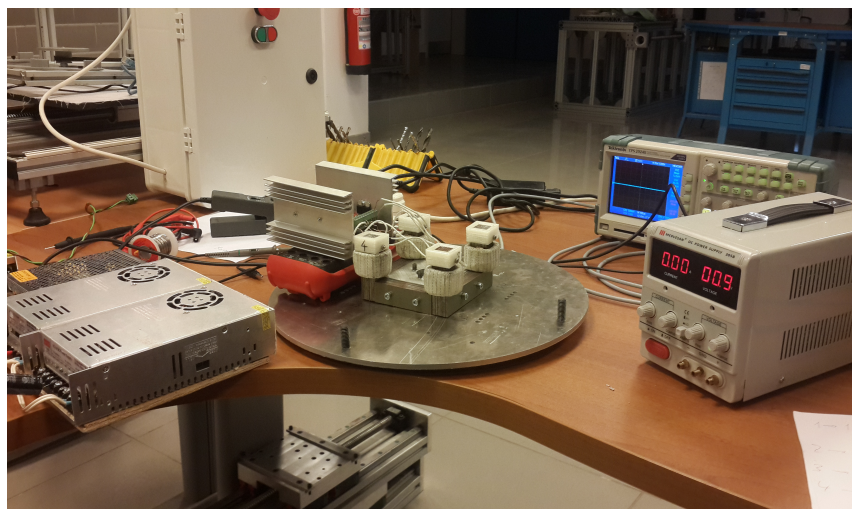
Figure 2.16 Coil calibration
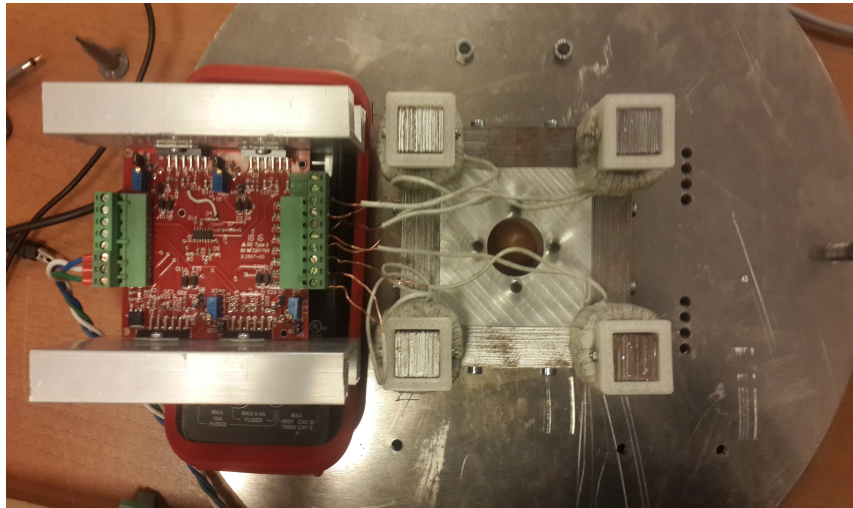
Figure 2.17 Coil testing

3
Experimental Setup

3.1 Hardware

3.1.1 Sensors

The processing board is run at 5 kHz, and some detailed information about sensors can be accessed by (NTComponents 2019), (Micro-Epsilon 2019), (TE 2019) and (DS1007 2019). The specs of the processing board and the sensors are given in Table 3.1, Table 3.2, Table 3.3 and Table 3.4.

Table 3.1 Current sensor specifications

Parameter	Value
Accuracy	± 0.2 %
Sensitivity	25 mV/A
Frequency Bandwidth	0-100 kHz
Linearity Error	<0.1 %
Response Time	<400 ns
Measuring Range	± 80 At

Table 3.2 Gap sensor specifications

Parameter	Value
Measuring Range	4 mm
Start of measuring range (SMR)	0.40 mm
Linearity	± 0.2800%
Output	0.5 - 9 V

Table 3.3 Accelerometer specifications

Parameter	Value
Range	± 2 g
Sensitivity	1000 mV/g
Frequency Response	0-200 Hz
Non-Linearity	± 1 %
Shock Limit	2000 g

Table 3.4 Processor specifications

Parameter	Value
Processor	Dual-core, 2 GHz
Memory	1 GB DRAM, 128 MB Flash Memory

3.1.2   Sensor Board

To have a compact design, a sensor board is placed on the way before the processor. Thus, all sensors can easily be check in case of any malfunction. Moreover, low-pass filters can be adapted to reject electrical noise as well.

Proteus® drawing of sensor board can be seen in Fig. 3.1 and Fig. 3.2.
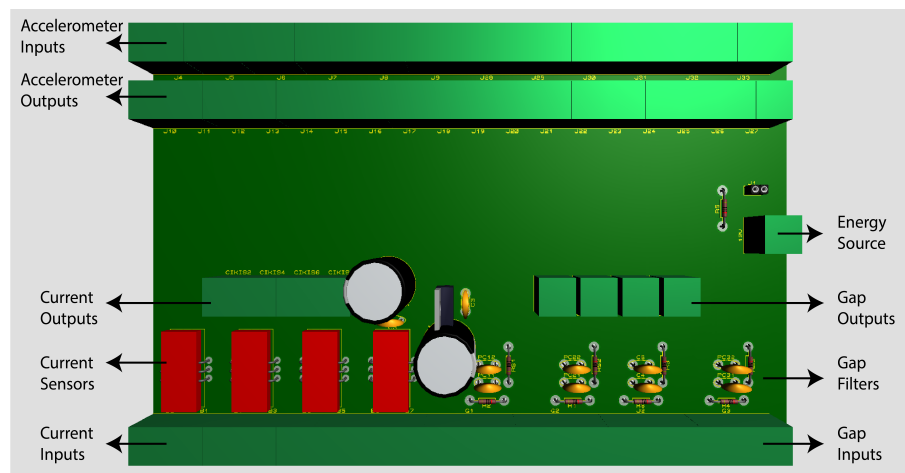
Figure 3.1 Proteus drawing of sensor board front view
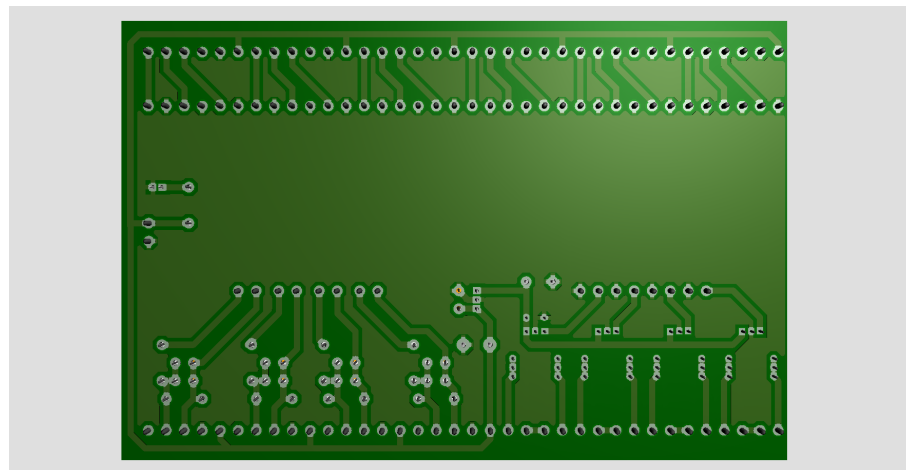
Figure 3.2 Proteus drawing of sensor board back view

3.1.3   Passive Adjustable Damping Element

Besides the damping contribution of springs to the experimental setup, passive adjustable damping elements have been added to the system. This element basically consists of circular permanent magnets, coil and 3d printed framework as shown in

Fig. 3.4 and Fig. 3.5. Its damping coefficient depends on adjustable distance and coil's resistance parameters.

Circular magnet's material is Nd35, and its outer diameter is 25 *mm*, inner diameter is 10 *mm*, and height is 5 *mm*.

Figure 3.3 Circular magnet
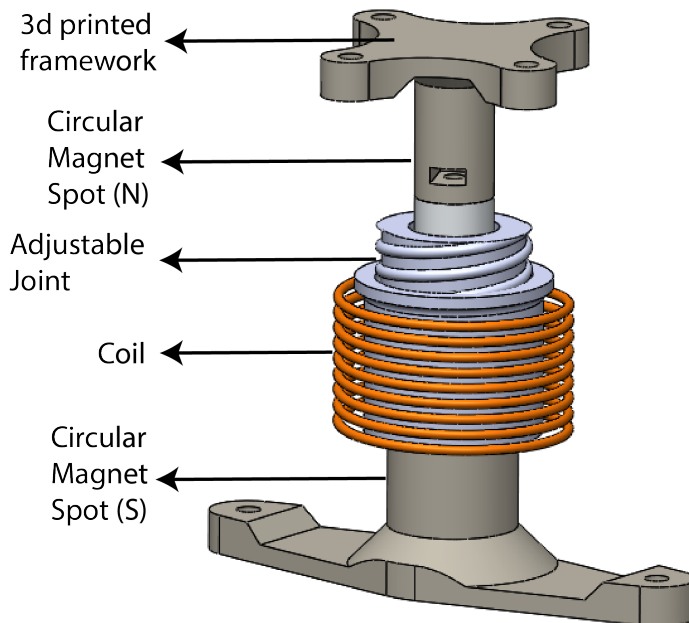
Figure 3.4 Passive damping element CAD isometric view

Adjustable distance can be changed by hand, whereas coil resistance can be changed by an integrated circuit given in Fig. 3.6 and Fig. 3.7.

In the integrated circuit, three different resistance values are designed for each coil. 1k, 3k, and 5k *Ohm*. In Fig. 3.8, these values have been determined by several experiments comparing damping parameters given by FEM results.

Outputs given in this thesis are conducted for 1k *Ohm* resistance. The obtained FEM results show that translational and rotational damping are best fit for 1k *Ohm*
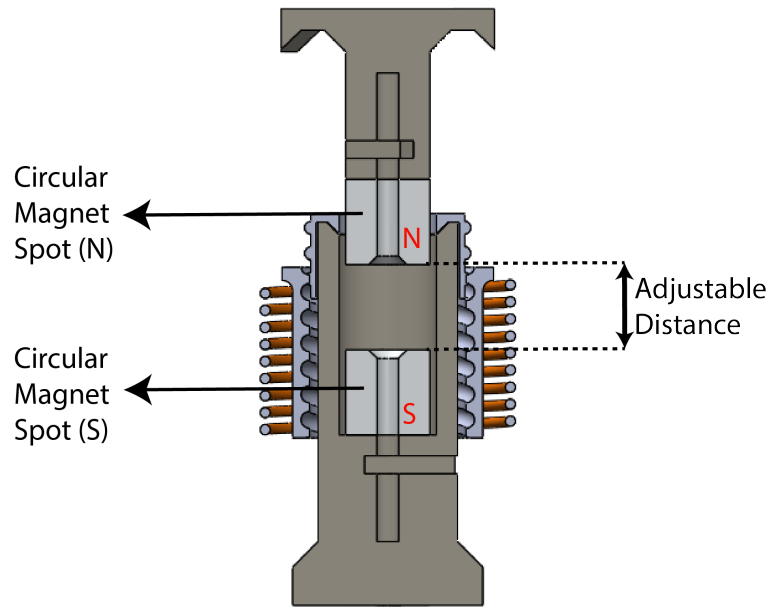
Figure 3.5 Passive damping element CAD section view
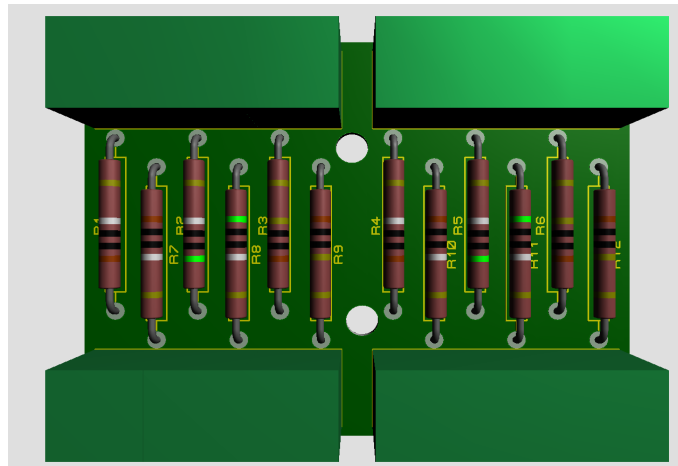
Figure 3.6 Proteus drawing of resistance integrated circuit front view
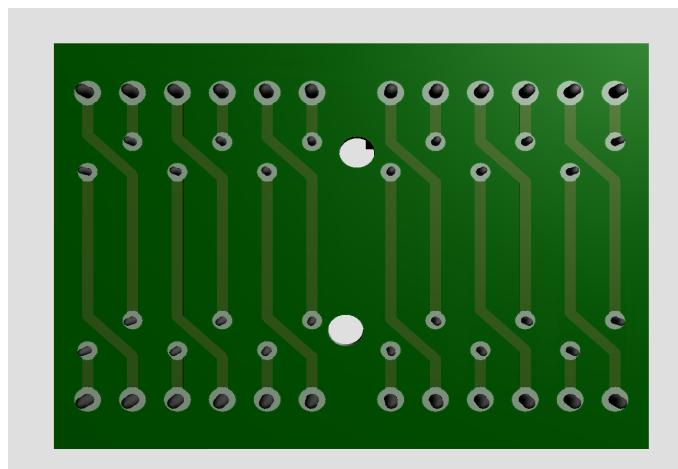
Figure 3.7 Proteus drawing of resistance integrated circuit back view
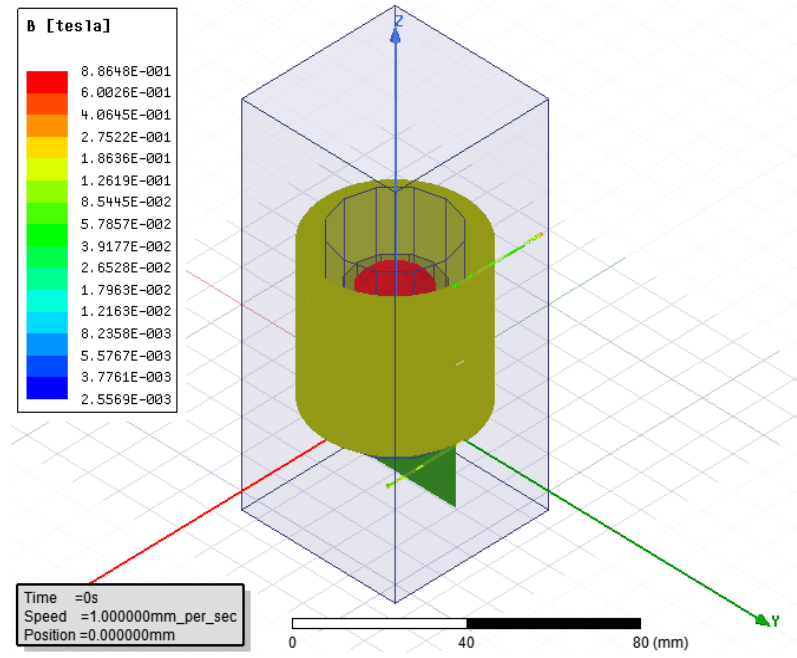
Figure 3.8 Damping element analysis by FEM

resistance. The values found in these figures allow to find overall translational damping value, 3800 Ns/m, by using second order curve fitting and linear regression methods. Rotational dampings can be found by using (2.31) and (2.32) as well. Identical rotational damping parameter for α and β axes is approximately equal to 300 $Nms/°$.

3.2 The Overall System

In Fig. 3.9, the isometric view and the side view of the experimental setup's CAD model can be seen. A1, A2 are accelerometers, S1, S2, S3, S4, S5, S6, S7 and S8 are suspension elements. G1, G2, G3 and G4 are gap sensors. In Fig. 3.10, the experimental setup is given.

Due to comparatively low mass of m_3, its energy storage capability is neglectable. Therefore, upper and lower suspension elements are assumed to be serially connected likewise in Fig. 2.2.

Gap sensor positioning and accelerometer positioning are given in Fig. 3.11 and Fig. 3.12, respectively. in Fig. 3.12, accelerometer center position is O(17 cm,2 cm).

In Table 3.5, the experimental setup's physical parameters are given. The functional structure is given in Fig. 3.13.
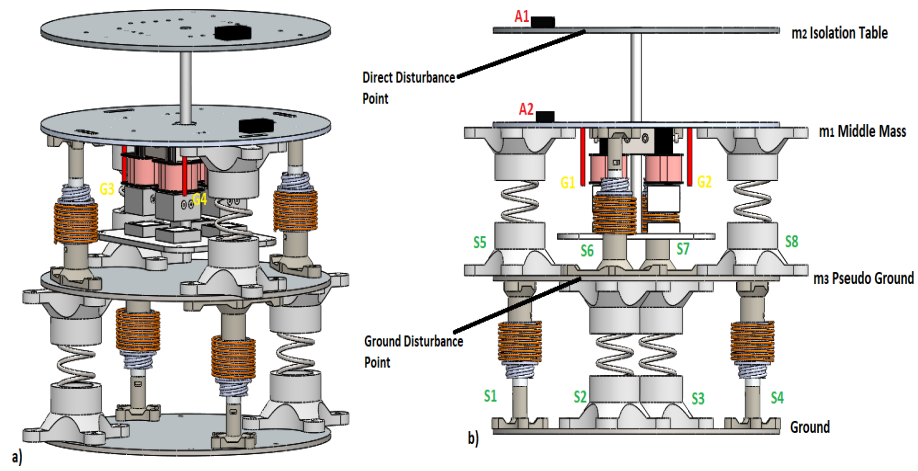
Figure 3.9 a. Isometric view, b. Side view
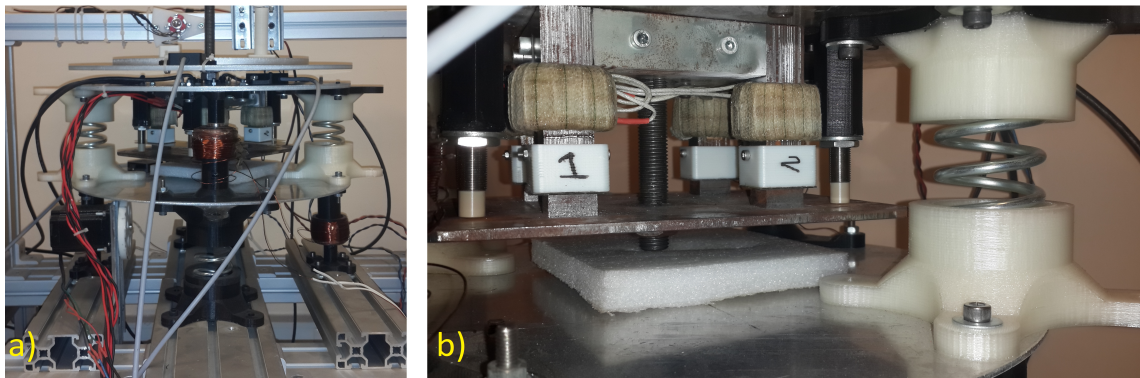
Figure 3.10 The experimental setup, a. Front view, b. Zoomed 4-pole hybrid electromagnet
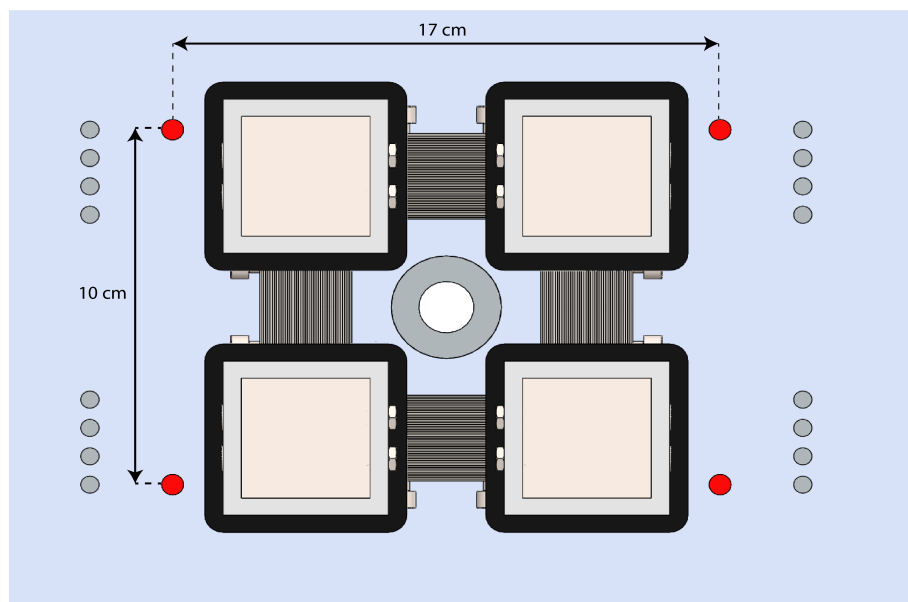
Figure 3.11 Gap sensor positioning
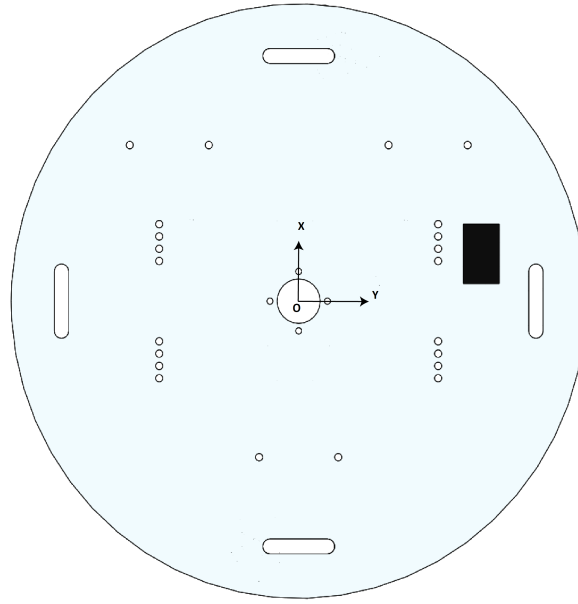
Figure 3.12 Accelerometer positioning

Table 3.5 Physical parameters for each axis

Axis / Parameter	z	α	β
$m_1 / I_1 \, [kg \; or \; kgm^2]$	2	0.15	0.2
$m_2 / I_2 \, [kg \; or \; kgm^2]$	5	0.3	0.4
$R \, [\Omega]$	1.6	1.6	1.6
$L \, [H]$	0.016	0.016	0.016
$k \, [N/m \; or \; Nm/rad]$	140000	100	200
$c \, [Ns/m \; or \; Nms/rad]$	3800	300	300
$K_{z0} \, [N/m \; or \; Nm/rad]$	-1205	-1102	-1205
$K_{i0} \, [N/A \; or \; Nm/A]$	3.92	4.5	4.7
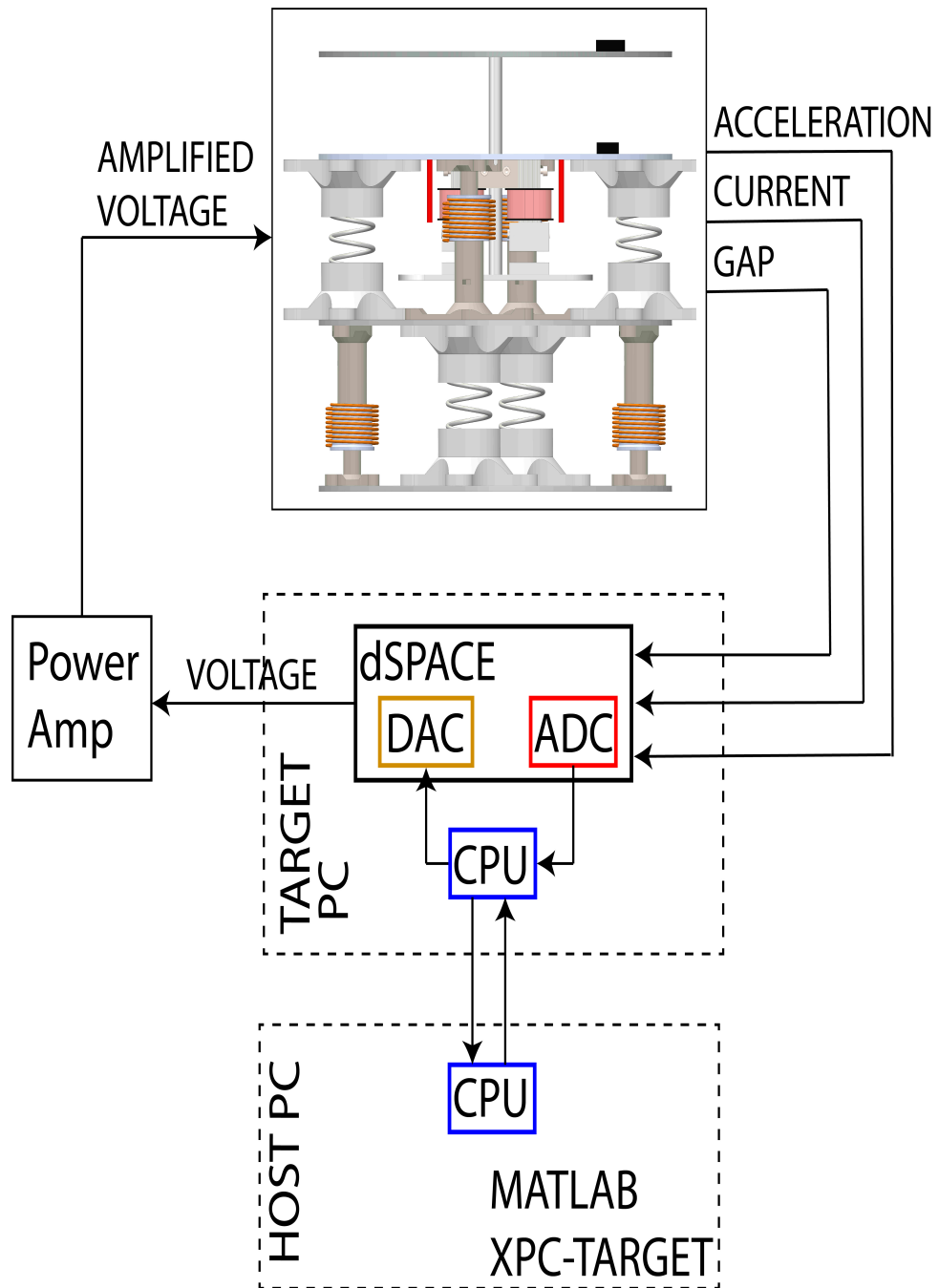
Figure 3.13 The functional structure of the experimental setup

4

Linear Matrix Inequality based $\mathscr{H}_2$ Full State Feedback Controller Syntheses and Experiments

4.1 $\mathscr{H}_2$ Full State-Feedback Controller Syntheses

General optimal control closed-loop scheme is given in Fig. 4.1. For any robustness problem, the main objective is to construct K that can minimize the effect of w parameter on $\bar{z}$ parameter.
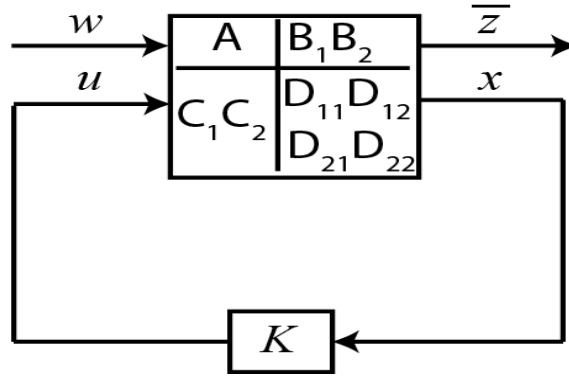
Figure 4.1 General optimal control closed loop scheme

Fig. 4.1 can be rewritten in terms of closed-loop matrices as follows.
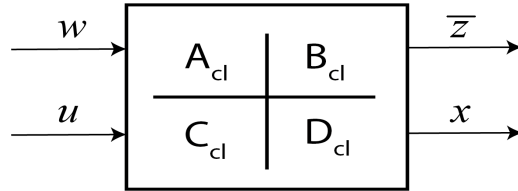
Figure 4.2 General optimal control closed loop scheme in terms of closed-loop matrices

$$u = Kx \qquad (4.1)$$

$$\frac{dx}{dt} = (A + B_1 K)x + B_2 w$$

$$\bar{z} = (C_2 + D_{21}K)x + D_{22}w \tag{4.2}$$

The main requirements can be stated as follows:

(i) The closed loop system (4.2) is asymptotically stable which indicates that all eigenvalues of $A + B_1 K$ have negative real parts.

(ii) Vibration isolation performance is maximized by minimizing the $\mathcal{H}_2$ norm between exogenous input w and the controlled outputs $\bar{z}$.

Theorem 1 (Boyd et al. 1994) : *For a given positive scalar r, the closed loop system (4.2) is asymptotically stable with $\mathcal{H}_2$ norm less than r, if there exist positive definite matrix $Y \in \mathbb{R}^{n \times n}$ and $W \in \mathbb{R}^{m \times n}$ subject to following convex optimization problem*

$$min\, r; s.t. (4.3), (4.4)$$

$$AY + YA + B_1 W + W^T B_1^T + B_2 B_2^T < 0 \tag{4.3}$$

$$Trace(CYC^T) < r \ \ for \ \ r = ||G||_2^2 \tag{4.4}$$

$$Y = Y^T > 0 \tag{4.5}$$

Then

$$K = WY^{-1} \tag{4.6}$$

Considering that these inequalities have to be written for synthesising controller of each axis;

For z translational axis;

$$\min r_z; s.t. (4.7), (4.8)$$

$$A_z Y_z + Y_z A_z + B_{1,z} W_z + W_z^T B_{1,z}^T + B_{2,z} B_{2,z}^T < 0 \tag{4.7}$$

$$Trace(C_z Y_z C_z^T) < r_z \ \ for \ \ r_z = \|G_z\|_2^2 \tag{4.8}$$

$$Y_z = Y_z^T > 0 \tag{4.9}$$

$$K_z = W_z Y_z^{-1} \tag{4.10}$$

For α rotational axis;

$$\min r_\alpha; s.t. (4.11), (4.12)$$

$$A_\alpha Y_\alpha + Y_\alpha A_\alpha + B_{1,\alpha} W_\alpha + W_\alpha^T B_{1,\alpha}^T + B_{2,\alpha} B_{2,\alpha}^T < 0 \tag{4.11}$$

$$Trace(C_\alpha Y_\alpha C_\alpha^T) < r_\alpha \ \ for \ \ r_\alpha = \|G_\alpha\|_2^2 \tag{4.12}$$

$$Y_\alpha = Y_\alpha^T > 0 \tag{4.13}$$

$$K_\alpha = W_\alpha Y_\alpha^{-1} \tag{4.14}$$

For β rotational axis;

$$\min r_\beta; s.t. (4.15), (4.16)$$

$$A_\beta Y_\beta + Y_\beta A_\beta + B_{1,\beta} W_\beta + W_\beta^T B_{1,\beta}^T + B_{2,\beta} B_{2,\beta}^T < 0 \tag{4.15}$$

$$Trace(C_\beta Y_\beta C_\beta^T) < r_\beta \ \ for \ \ r_\beta = ||G_\beta||_2^2 \tag{4.16}$$

$$Y_\beta = Y_\beta^T > 0 \tag{4.17}$$

$$K_\beta = W_\beta Y_\beta^{-1} \tag{4.18}$$

And the general state feedback control schemes for each axis are given as follows;
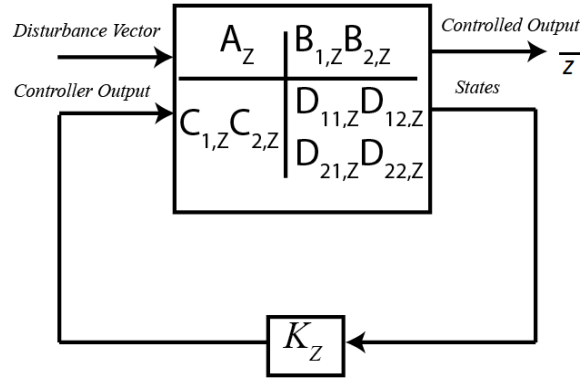
Figure 4.3 General feedback control scheme for z axis
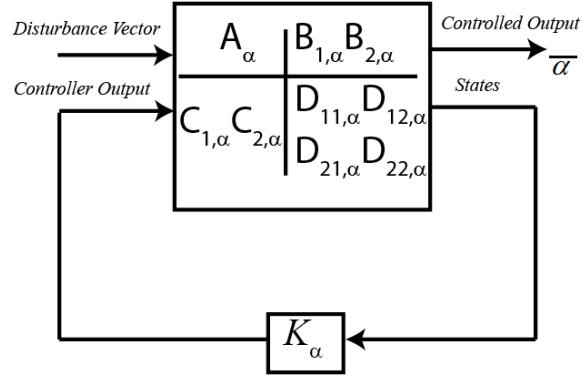
Figure 4.4 General feedback control scheme for α axis
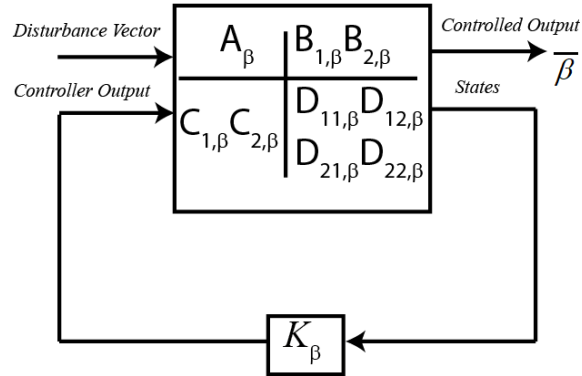
Figure 4.5 General feedback control scheme for β axis

For LMI based $\mathcal{H}_2$ disturbance rejection with zero-power controller given in Section 2, the controller gains can be computed with Theorem 1 by using the YALMIP parser (Lofberg 2004) and SeDuMi solver (Sturm 1999).

$$K_z = \begin{array}{l} 10^4[-1.1684 \quad -0.1578 \quad -0.0152\ldots \\ \ldots 0.1104 \quad\quad 0.0518 \quad -0.1578] \end{array} \tag{4.19}$$

$$K_\alpha = \begin{array}{l} [-110.8518 \quad -23.1467 \quad -43.3302\ldots \\ \ldots 0.4282 \quad 0.5931 \times 10^4 \quad 1.1215] \end{array} \tag{4.20}$$

$$K_\beta = \begin{array}{l} [-16.5492 \quad -5.8538 \quad -9.3606\ldots \\ \ldots 101.1111 \quad 1.5439 \quad 0.1291] \end{array} \tag{4.21}$$

Then, the resulting closed-loop pole placements are given by

$$\sigma_z(A_z + B_{1,z}K_z) = (-102410, -130500, -1121, -121, -32, -21) \tag{4.22}$$

$$\sigma_\alpha(A_\alpha + B_{1,\alpha}K_\alpha) = (-639, -32 \pm 53j, -21 \pm 35j, 0.11) \tag{4.23}$$

$$\sigma_\beta(A_\beta + B_{1,\beta}K_\beta) = (-503 \pm 92j, -16 \pm 52j, -52, 0.15) \tag{4.24}$$

For zero-power case, analytical and experimental bode plots for the closed loop of z translational axis, α rotational axis, β rotational axis are given in Fig. 4.6, Fig. 4.7 Fig. 4.8, Fig. 4.9, Fig. 4.10 and Fig. 4.11, respectively. As can be seen, analytical and experimental magnitude bode plots match and the system converges to robustness while the frequency of the parameters in w vector increase. Especially ground and direct disturbances at comparatively high frequencies have less effect on $\bar{z}$.
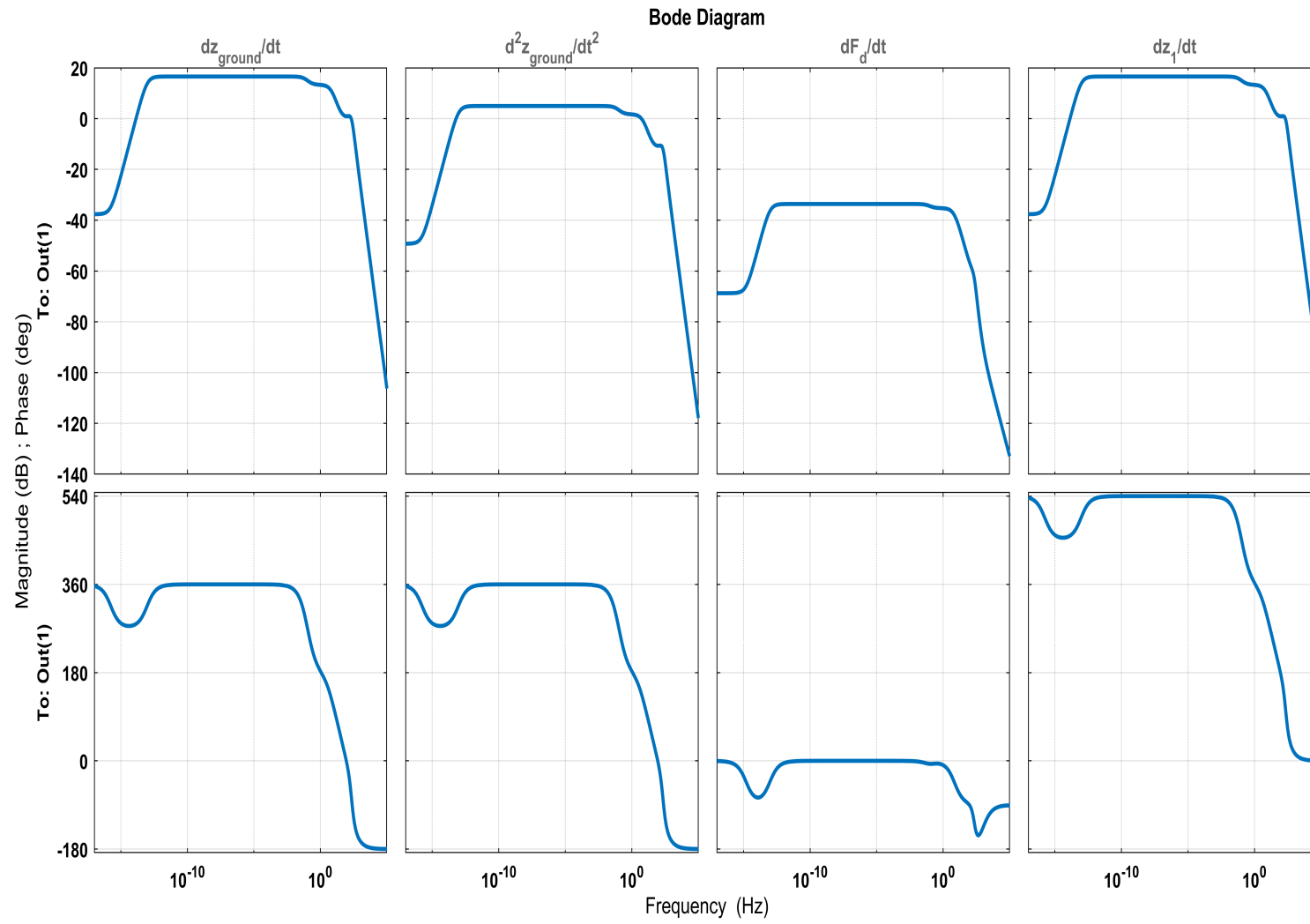
Figure 4.6 Analytical bode plots of z axis
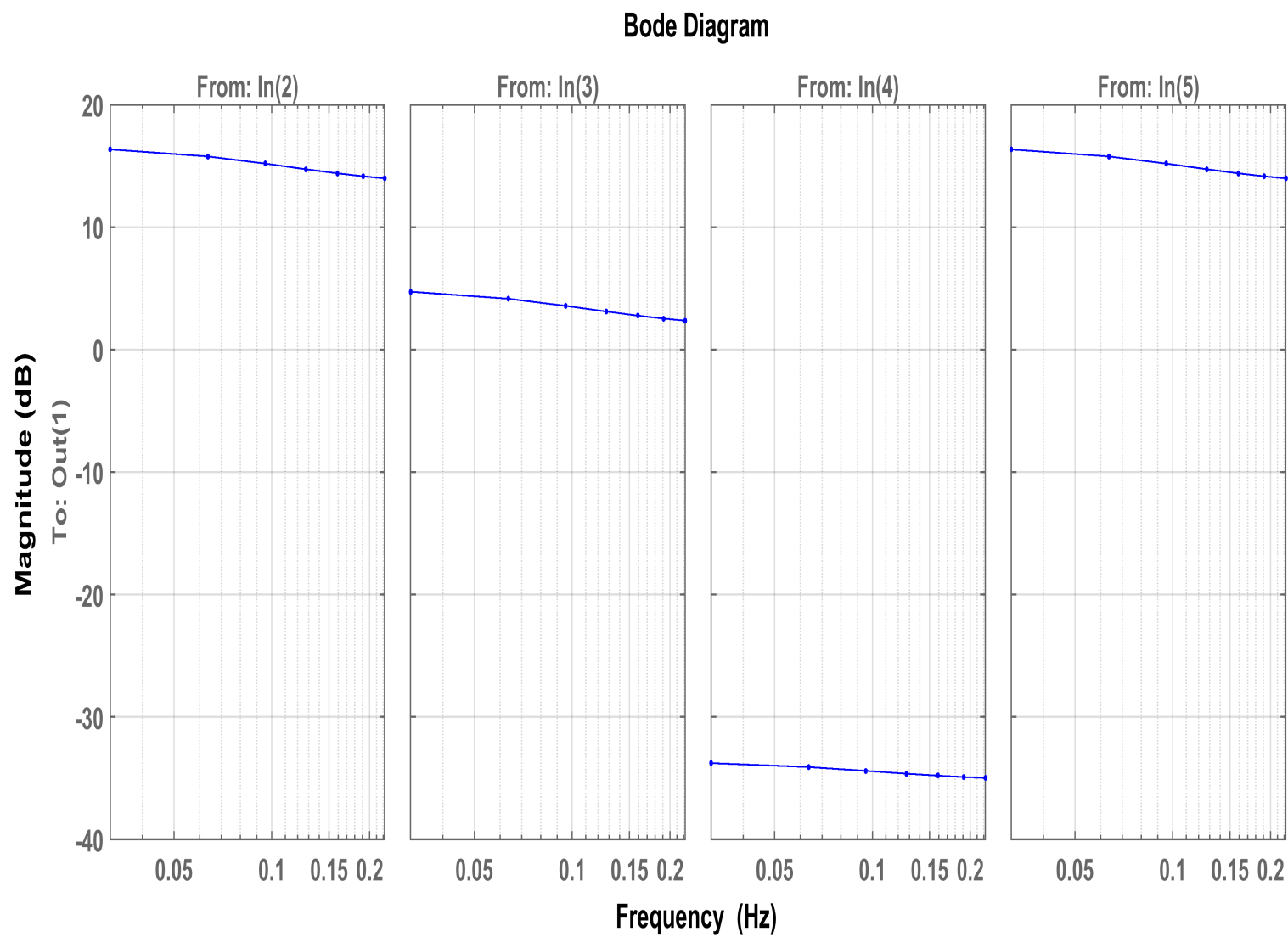
Figure 4.7 Experimental bode plots of z axis
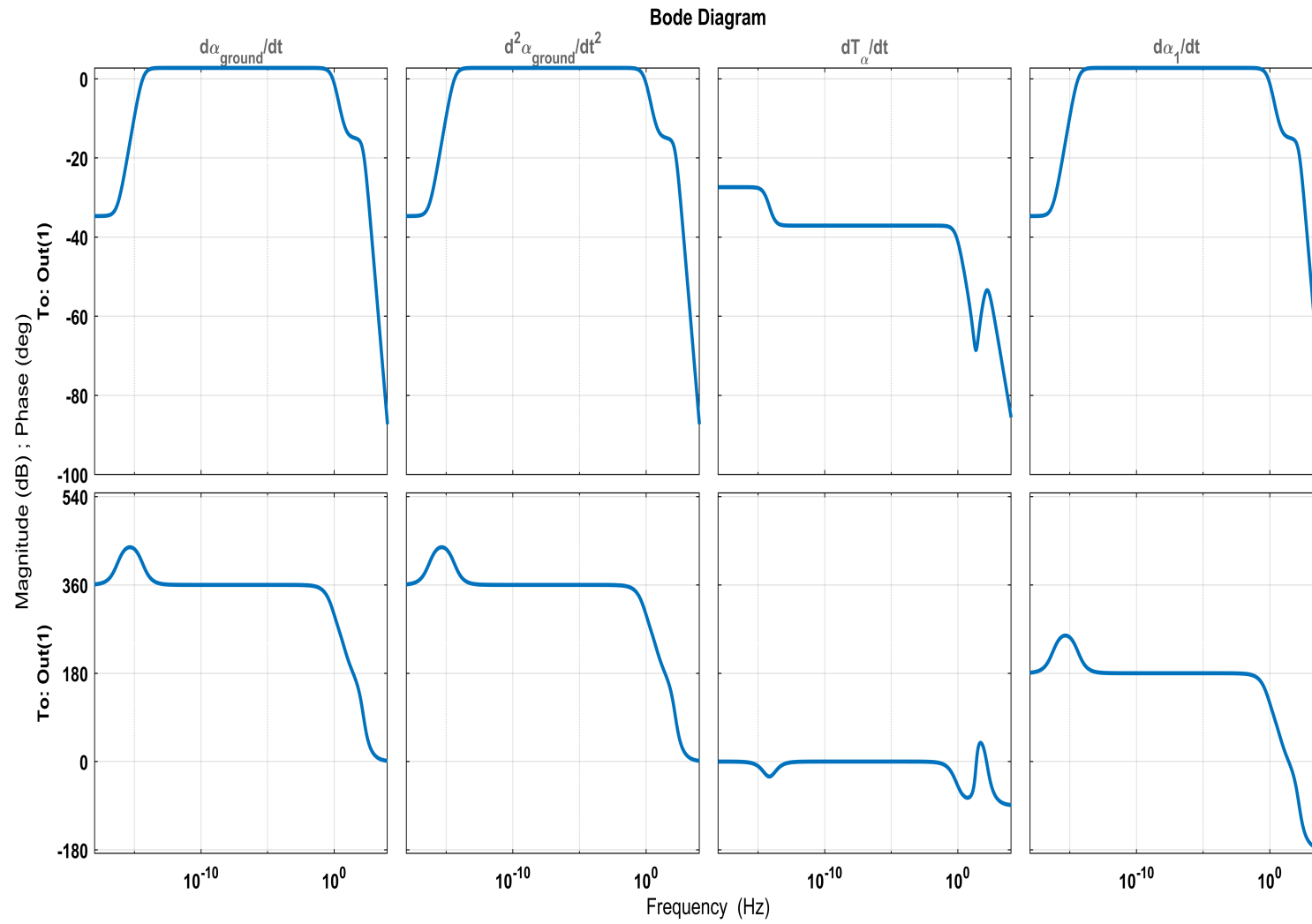
Figure 4.8 Analytical bode plots of α axis
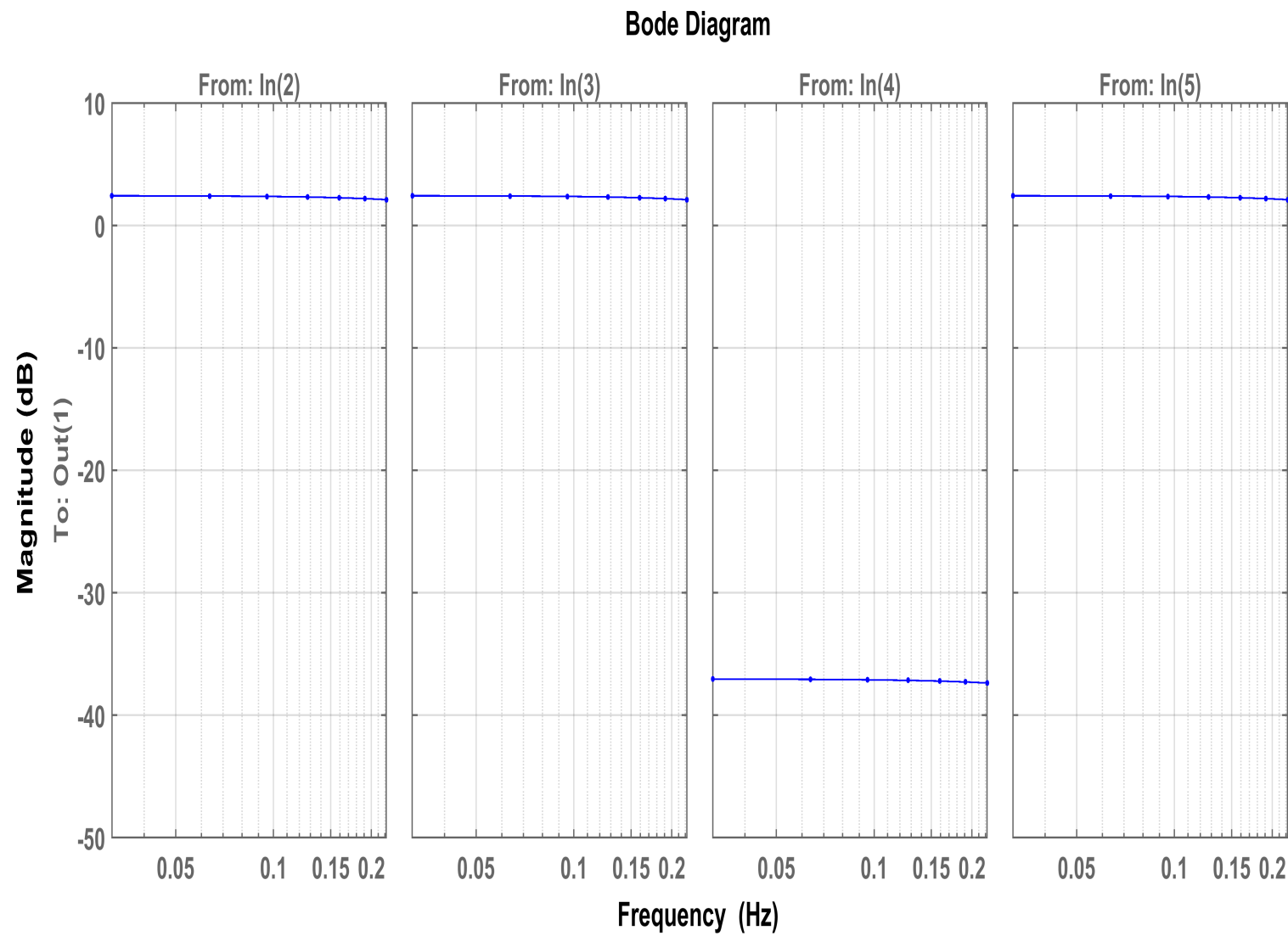
Figure 4.9 Experimental bode plots of α axis
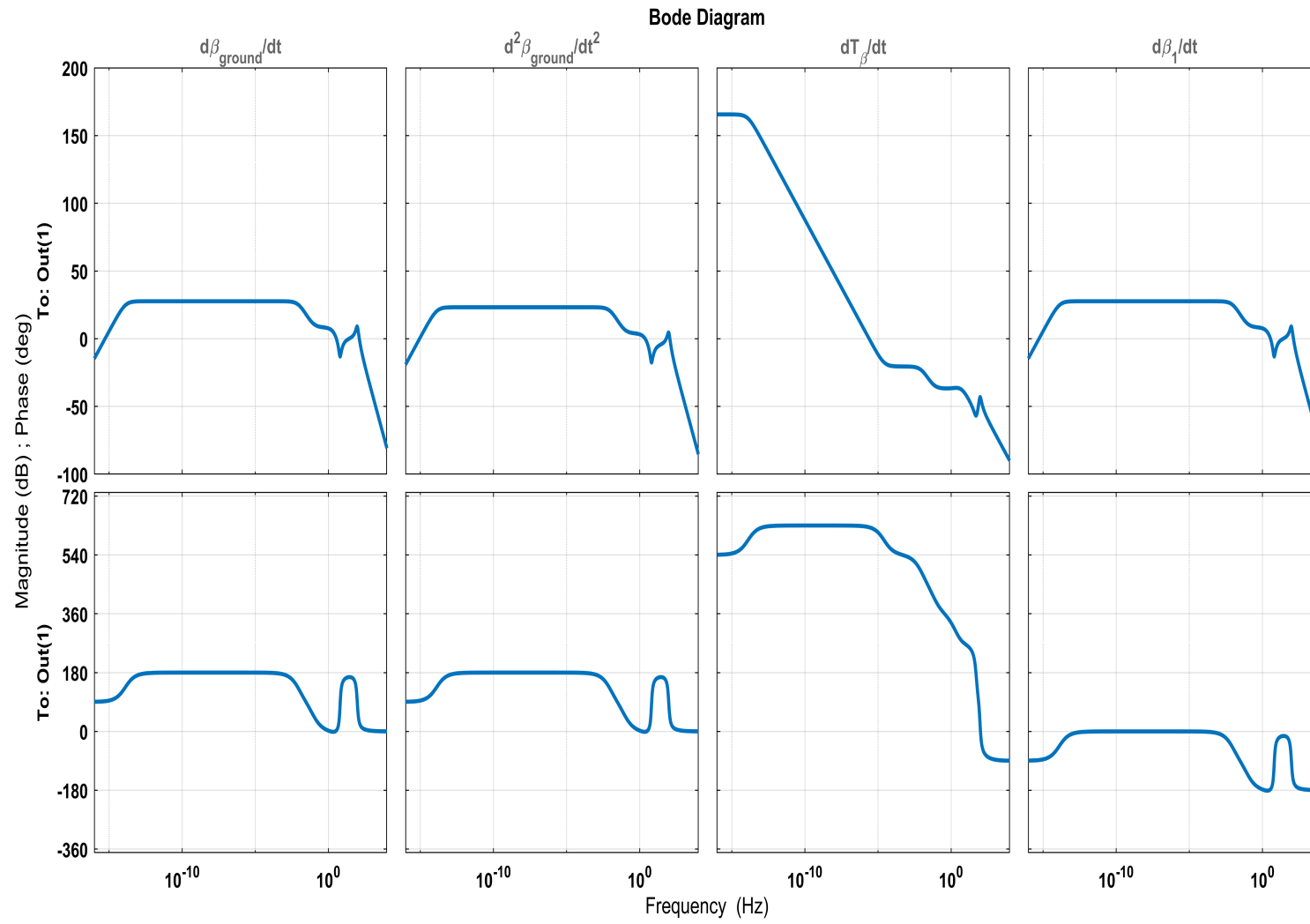
Figure 4.10 Analytical bode plots of β axis
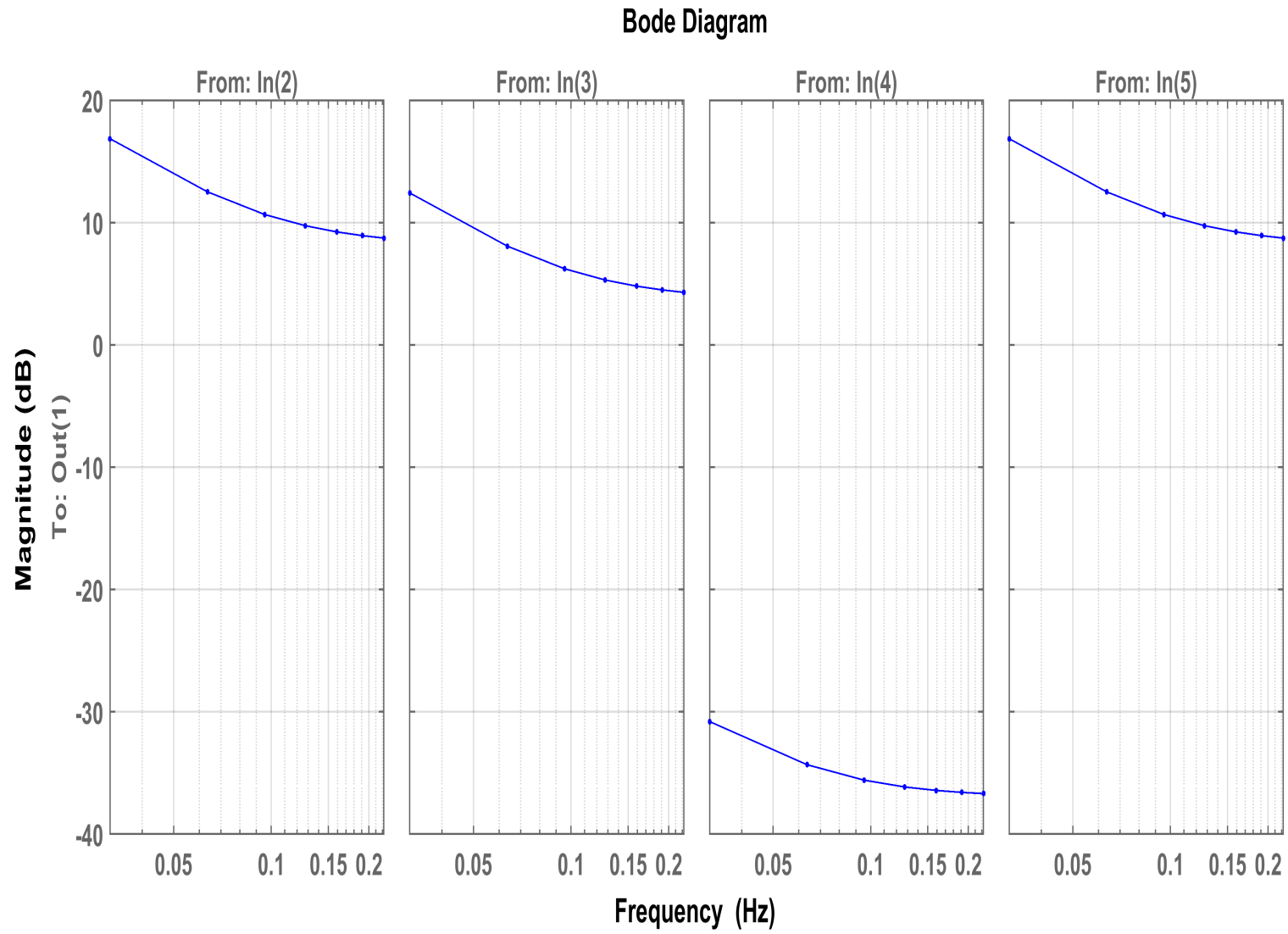
Figure 4.11 Experimental bode plots of β axis

Fig. 4.6, Fig. 4.7 Fig. 4.8, Fig. 4.9, Fig. 4.10 and Fig. 4.11 show the effect of w vector in 2.15 on C_2 vector in 2.24 at different frequencies. To obtain the effect of w vector on each parameter in C_2 vector both analytically and experimentally, C_2 vector needs to be reconstructed as including only one integer inside. Analytical and experimental bode plots of each parameter are given in Appendix-B.

4.2 Experiment Configurations

The coordinates of the applied disturbance for both ground and direct disturbance are $O(12\overrightarrow{X} - 12\overrightarrow{Y})\ cm$. O is the geometric center of $40\ cm$ diameter circular middle mass and isolation stage. The magnitude is $+2\ mm$ position change for direct disturbance, whereas it is $-2\ mm$ position change for ground disturbance. The total value is $2 - (-2) = 4\ mm$.
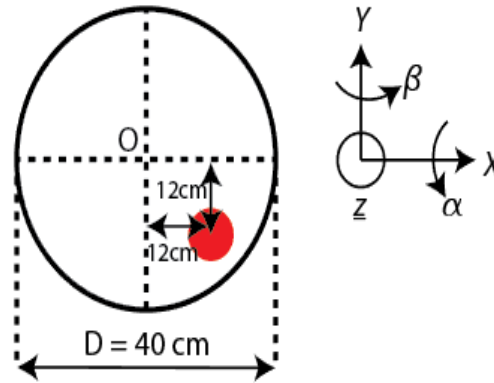
Figure 4.12 The exact position of both ground and direct disturbance

As obtained from the bode magnitude and phase plots, each exis have some critical zones in terms of frequency shifting and magnitude amplification. This range is between 0-0.4 frequency band. Therefore, the experiments are conducted by four steps in this range. $0.4\ Hz$, $0.2\ Hz$, $0.15\ Hz$ and $0.1\ Hz$ disturbances.

4.3 Experiment : LMI $\mathcal{H}_2$ Full State-Feedback Zero Power Controller Performance in the Absence of Disturbances

During zero-power control, the main objective is to keep all axis-current values around 0 as much as possible while the effect of ground and direct disturbances varying at different magnitude and frequencies is being suppressed. Therefore, even for the no-disturbance case, position reference tracking around 0 for each axis may not succeed, which is absolutely expected, as shown in Fig. 4.16, Fig. 4.17, and Fig. 4.18.

Axis-current values oscillating around 0 are given in Fig. 4.13, Fig. 4.14 and Fig. 4.15.

Also, as shown in Fig. 4.6, Fig. 4.8, Fig. 4.10, reference signal has no impact on the controlled output. Therefore, there is no need to investigate reference signal and the controlled output relation at this point. The relations between disturbances and the controlled output are given in these figures as well.
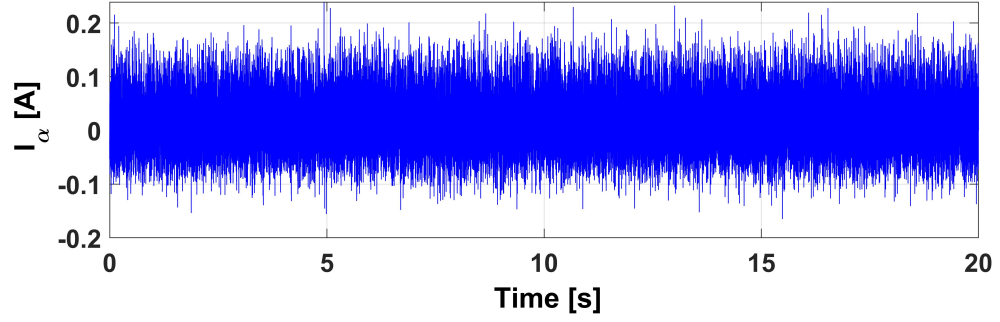
Figure 4.13 I_α for zero power with no disturbance case
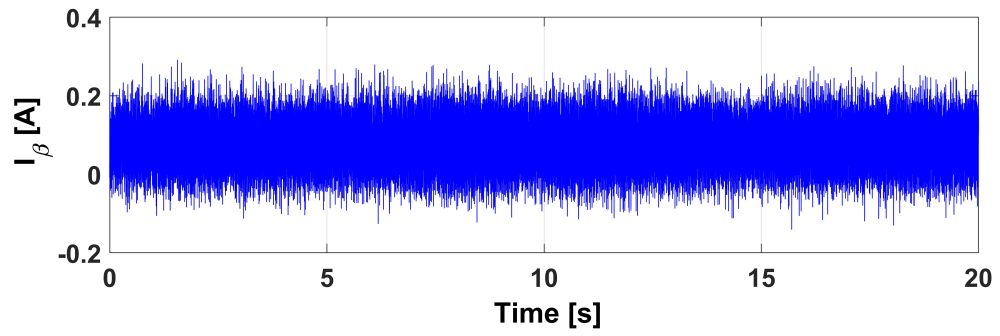
Figure 4.14 I_β for zero power with no disturbance case
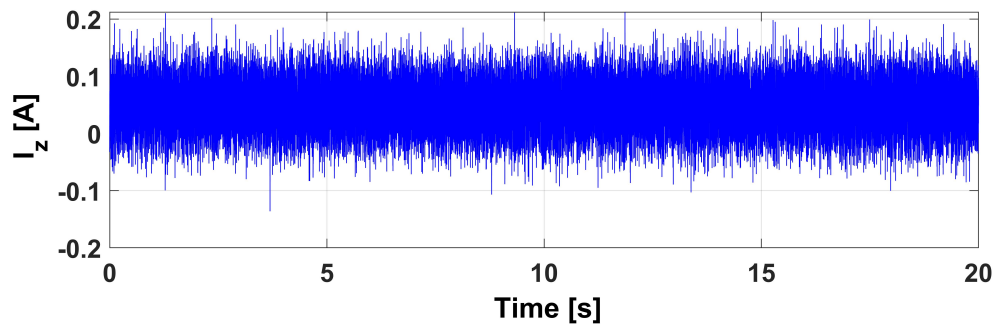
Figure 4.15 I_z for zero power with no disturbance case
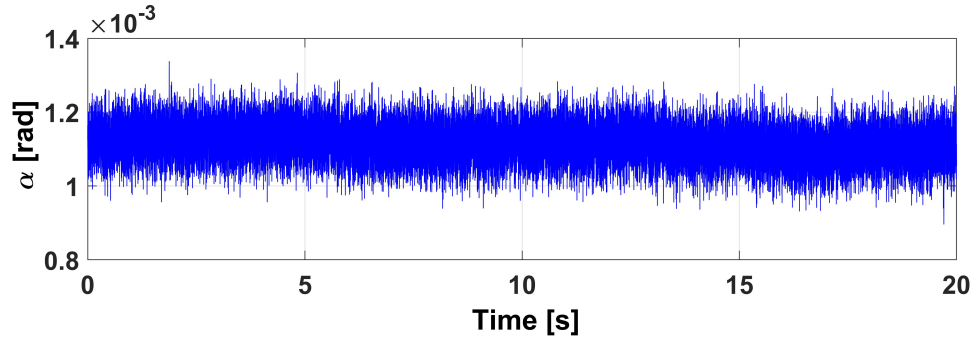
Figure 4.16 α for zero power with no disturbance case
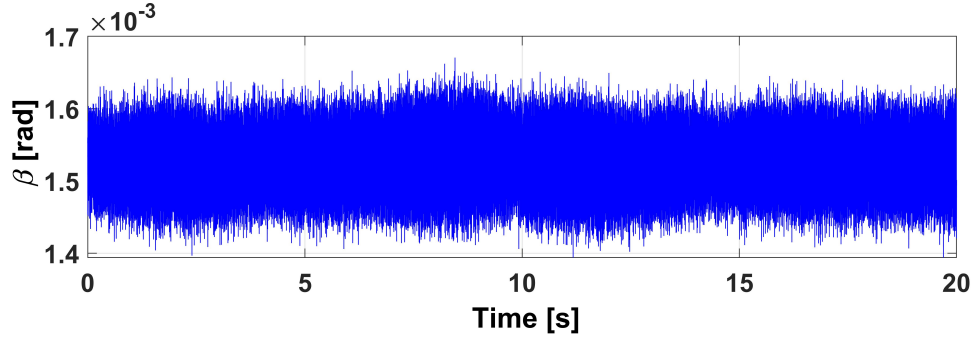
Figure 4.17 β for zero power with no disturbance case
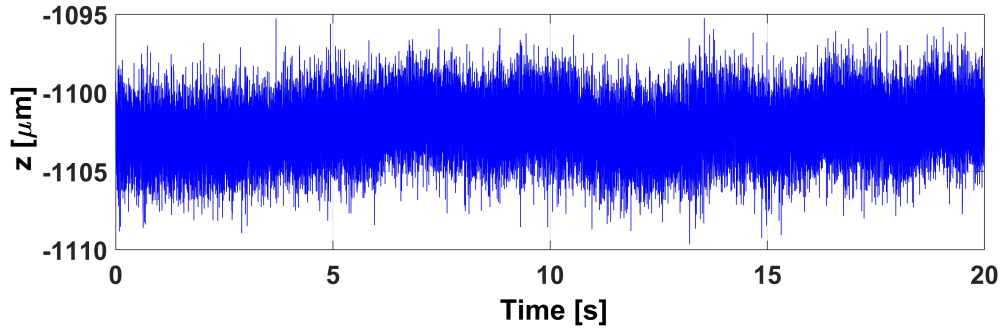
Figure 4.18 z for zero power with no disturbance case

Norm values of current parameters for no disturbancse case are given in Fig. 4.1. These values will later be compared to the norm values occurring for disturbance cases to understand energy efficiency performance of the system.

Table 4.1 Norm values of current parameters for no disturbance case

Parameter	Value
I_α	0.321240
I_β	0.321212
I_z	0.80111

4.4 Experiment : LMI $\mathcal{H}_2$ Full State-Feedback Zero Power Controller Performance at 0.4 Hz Multi-Directional Disturbances

From the bode plots previously given, the critical frequency point in terms of frequency shifting and magnitude amplification has been chosen as 0.4 *Hz* in this experiment. Thus, the responses for ground disturbance, direct disturbance and both disturbances cases have been compared at this frequency.

As can be seen in Fig. 4.19, the system shows perfect minimum-compliance behavior against the 2 *mm* ground disturbance. The air gap changes only 20 *μm*. For 2 *mm* direct disturbance, the change for the aip gap is only 50 *μm*. At both disturbance case, the total air gap change is around 100 *μm*.

The norm values of the translational air gaps for the experiment are given in Table. 4.2 and the norm values of the translational axis currents for the experiment are given in Table. 4.3. The values go up while the disturbance factor increases.

The norm values in Table. 4.2 change from 100.00121 to 2523.24592 and the norm values in Table. 4.3 change from 2.12291 to 4.92912.

The norms can somehow be named as the functions of the required energy to deal with the applied mechanic disturbances. While the number of the disturbances increases, the amount of the required energy goes up. However, the coil currents are not the only source to deal with these disturbances. Permanent magnets can as if they are equivalent energy sources as well.

While the frequency of the disturbances increase, the amount of the required energy decreases as the bode plots given previously suggest. This issue will be shown in a detailed way in the next experiment.

From Fig. 4.19, Table 4.2 and Table 4.3, it can also be seen that the system shows almost perfect zero-power behavior in the absence of the disturbances. Moreover, the system's energy consumption is comparatively low, while the system is being affected by the disturbances.

Table 4.2 Norm values of z parameters for 0.4 Hz disturbance case

Disturbance Type	Norm z
No Disturbance	100.00121
Ground Disturbance	200.53921
Direct Disturbance	1202.53312
Multi Directional Disturbances	2523.24592
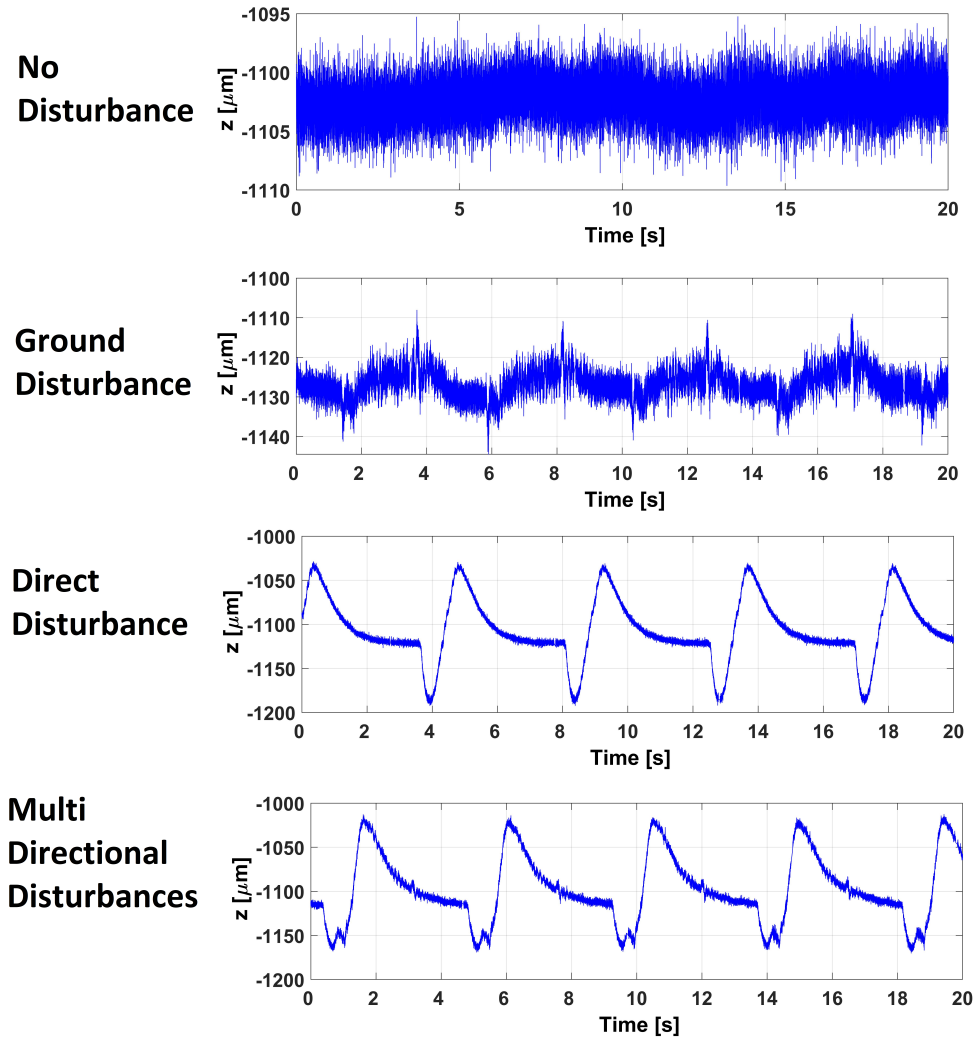
Figure 4.19 z for zero power with 0.4 Hz disturbance case

Table 4.3 Norm values of I_z parameters for 0.4 Hz disturbance case

Disturbance Type	Norm z
No Disturbance	2.12291
Ground Disturbance	2.92392
Direct Disturbance	4.52898
Multi Directional Disturbances	4.92912
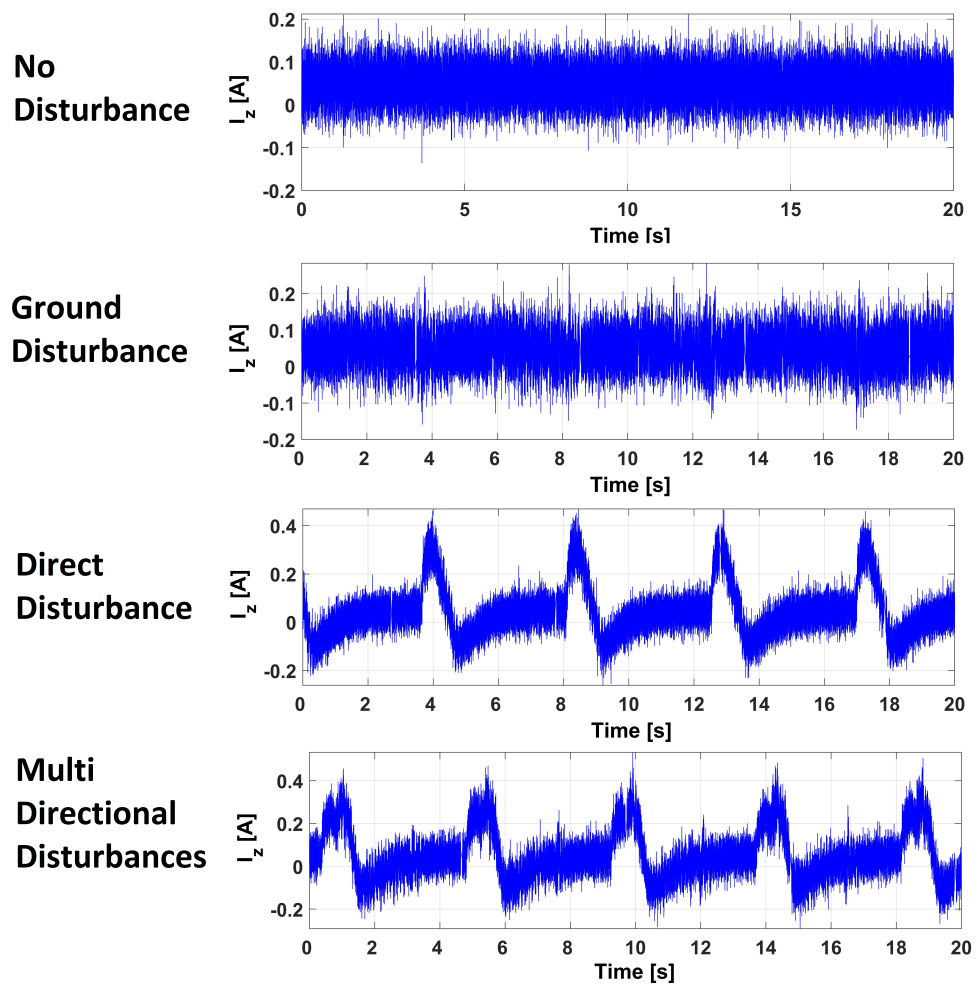
Figure 4.20 I_z for zero power with 0.4 Hz disturbance case

Due to the fact that the disturbances are applied as displacements, the stiffness parameter can not directly be measured. Aforementioned minimum-compliance behavior can also be seen for rotational gap and rotational current values in Fig. 4.21 and Fig. 4.23.

The norm values for rotational gaps and rotational currents for α axis are given in Table 4.4 and Table 4.5. Whereas, the norm values for rotational gaps and rotational currents for β axis are given in Table 4.6 and Table 4.7

From Fig. 4.21, Fig. 4.23 Table 4.4, Table 4.5, Table 4.6, Table 4.7, it can be seen that the movements for rotational axes show almost perfect zero-power behavior in the absence of the disturbances. Even though the mechanic disturbance is being applied as 2 *mm* translational position change on *z* axis, it generates torque due on each rotational axis to its position. Yet, rotational stiffness parameters can not be measured. Though, it can be said that the system's minimum-compliance performance on rotational axis is satisfying. The system's energy consumption for each rotational axis is comparatively low, while the system is being affected by the disturbances.

The norm values in Table. 4.4 change from 120.52231 to 2232.23211 and the norm values in Table. 4.5 change from 2.35342 to 5.22311.

Table 4.4 Norm values of α parameters for 0.4 Hz disturbance case

Disturbance Type	Norm α
No Disturbance	120.52231
Ground Disturbance	210.32542
Direct Disturbance	1322.35341
Multi Directional Disturbances	2232.23211

Table 4.5 Norm values of I_α parameters for 0.4 Hz disturbance case

Disturbance Type	Norm α
No Disturbance	2.35342
Ground Disturbance	3.35439
Direct Disturbance	4.66542
Multi Directional Disturbances	5.22311

The norm values in Table. 4.6 change from 130.54542 to 2992.23121 and the norm values in Table. 4.7 change from 3.45421 to 5.92912.
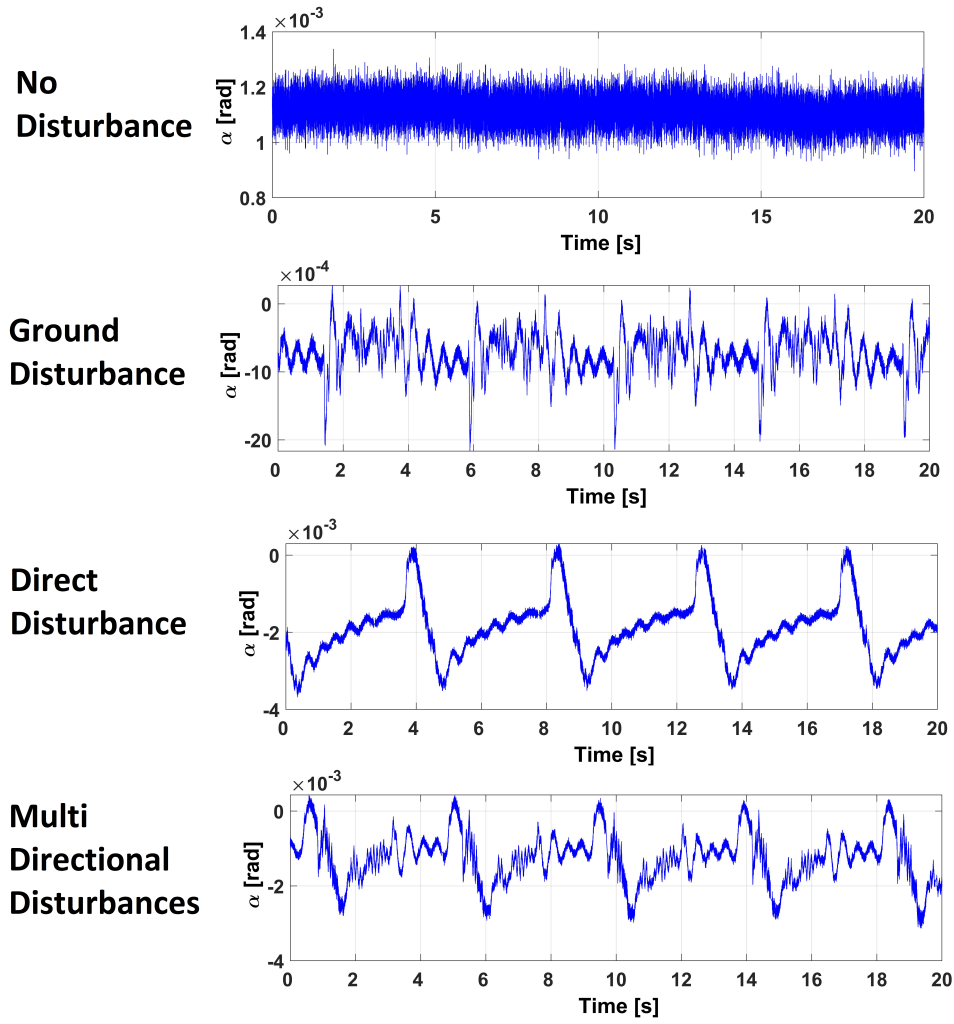
Figure 4.21 α for zero power with 0.4 Hz disturbance case

Table 4.6 Norm values of β parameters for 0.4 Hz disturbance case

Disturbance Type	Norm β
No Disturbance	130.54542
Ground Disturbance	210.45421
Direct Disturbance	1423.45421
Multi Directional Disturbances	2992.23121

Table 4.7 Norm values of I_β parameters for 0.4 Hz disturbance case

Disturbance Type	Norm β
No Disturbance	3.45421
Ground Disturbance	4.22321
Direct Disturbance	4.52898
Multi Directional Disturbances	5.92912
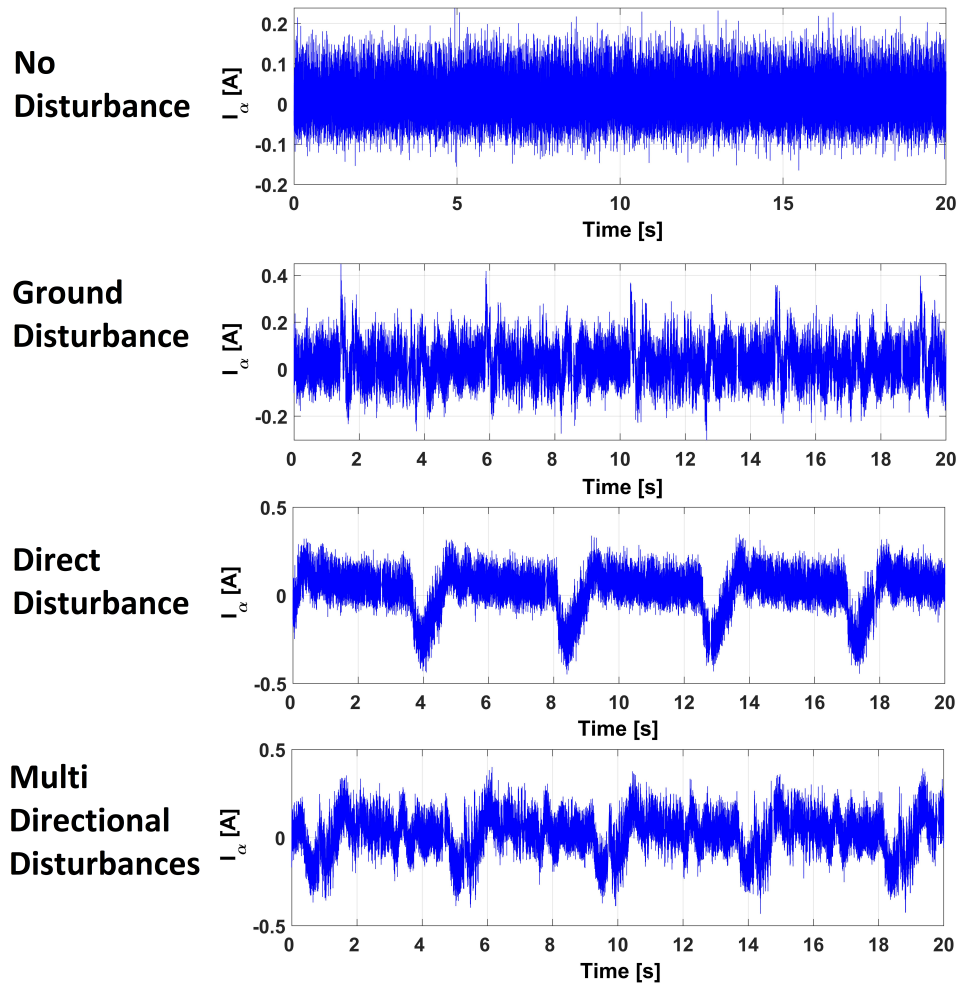
Figure 4.22 I_α for zero power with 0.4 Hz disturbance case
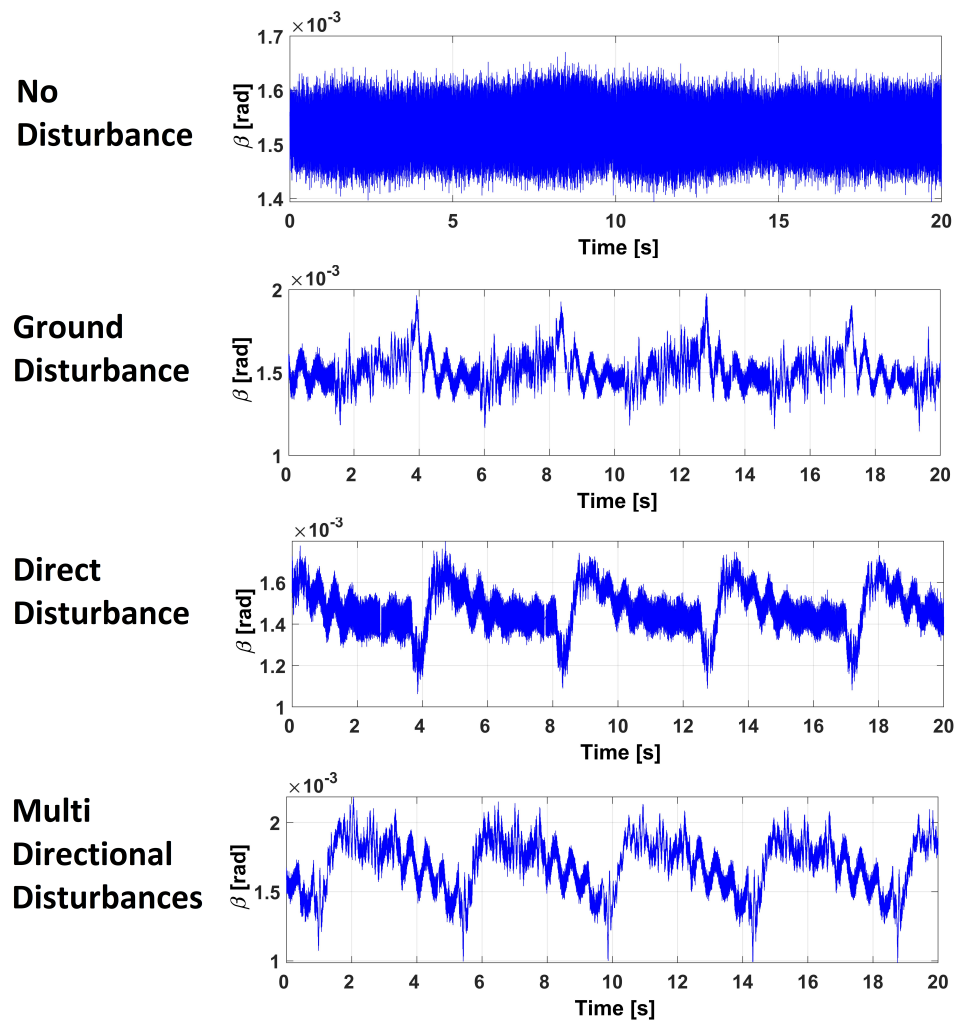
Figure 4.23 β for zero power with 0.4 Hz disturbance case
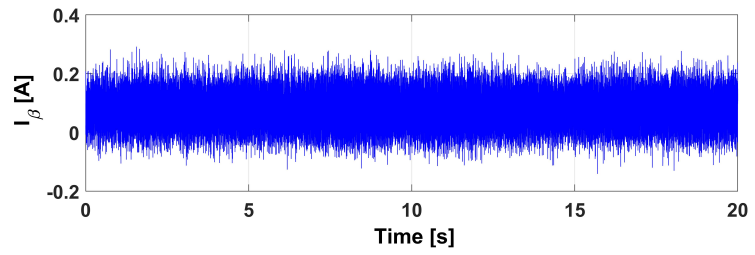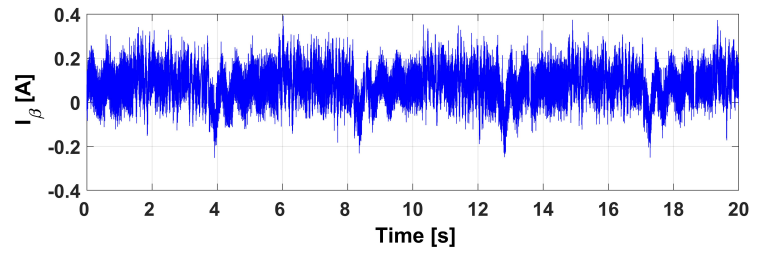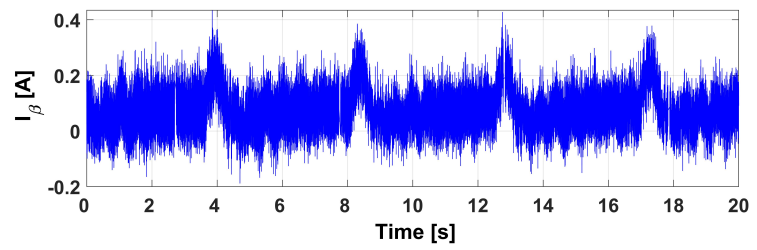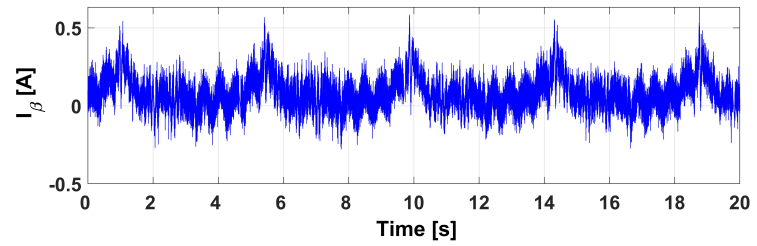
Figure 4.24 I_β for zero power with 0.4 Hz disturbance case

4.5 Experiment : LMI $\mathcal{H}_2$ Full State-Feedback Zero Power Controller Performance for Variable Frequency Disturbances

To show the relation between the disturbances and the controlled output vector for each axis, the critical points in terms of frequency are being zoomed in the figures as follows. While frequency of disturbances increases, the effect on the controlled output dramatically decreases, as given in Fig. 4.25, Fig. 4.26, Fig. 4.27, Fig. 4.28, Fig. 4.29 and Fig. 4.30.

The controlled output vectors and the disturbance vectors for each three axis are written down as follows. At this point, one should remember that the state feed-back gains are synthesized to minimize the effect of the disturbance vectors on the parameters defined in the controlled output vector of each axis.

One important aspect is that; the bode plots give the relation between input and output at a specific frequency, which means that; whereas $0.1\,Hz$ disturbance forges more amount of current than $0.4\,Hz$ disturbance for a single sampling, $0.4\,Hz$ disturbance requires more amount of energy to be stabilized than $0.1\,Hz$ disturbance for a specific period of time. This issue can easily be observed from Fig. 4.31, Fig. 4.32, Fig. 4.33, Table 4.8, Table 4.9, Table 4.10, Table 4.11, Table 4.12 and Table 4.13.

$$w_z = \begin{bmatrix} z_{ref} & \frac{d\triangle z_{ground}}{dt} & \frac{d^2\triangle z_{ground}}{dt^2} & \frac{dF_d}{dt} & \frac{dz_1}{dt} \end{bmatrix}^T \tag{4.25}$$

$$w_\alpha = \begin{bmatrix} \alpha_{ref} & \frac{d\triangle \alpha_{ground}}{dt} & \frac{d^2\triangle \alpha_{ground}}{dt^2} & \frac{dT_\alpha}{dt} & \frac{d\alpha_1}{dt} \end{bmatrix}^T$$

$$w_\beta = \begin{bmatrix} \beta_{ref} & \frac{d\triangle \beta_{ground}}{dt} & \frac{d^2\triangle \beta_{ground}}{dt^2} & \frac{dT_\beta}{dt} & \frac{d\beta_1}{dt} \end{bmatrix}^T$$

$$\bar{z} = \begin{bmatrix} \frac{d^2\triangle z_2}{dt^2} + \triangle i_z + \int (0 - V_z)dt \end{bmatrix} \tag{4.26}$$

$$\bar{\alpha} = \begin{bmatrix} \frac{d^2\triangle \alpha_2}{dt^2} + \triangle i_\alpha + \int (0 - V_\alpha)dt \end{bmatrix}$$

$$\bar{\beta} = \begin{bmatrix} \frac{d^2\triangle \beta_2}{dt^2} + \triangle i_\beta + \int (0 - V_\beta)dt \end{bmatrix}$$
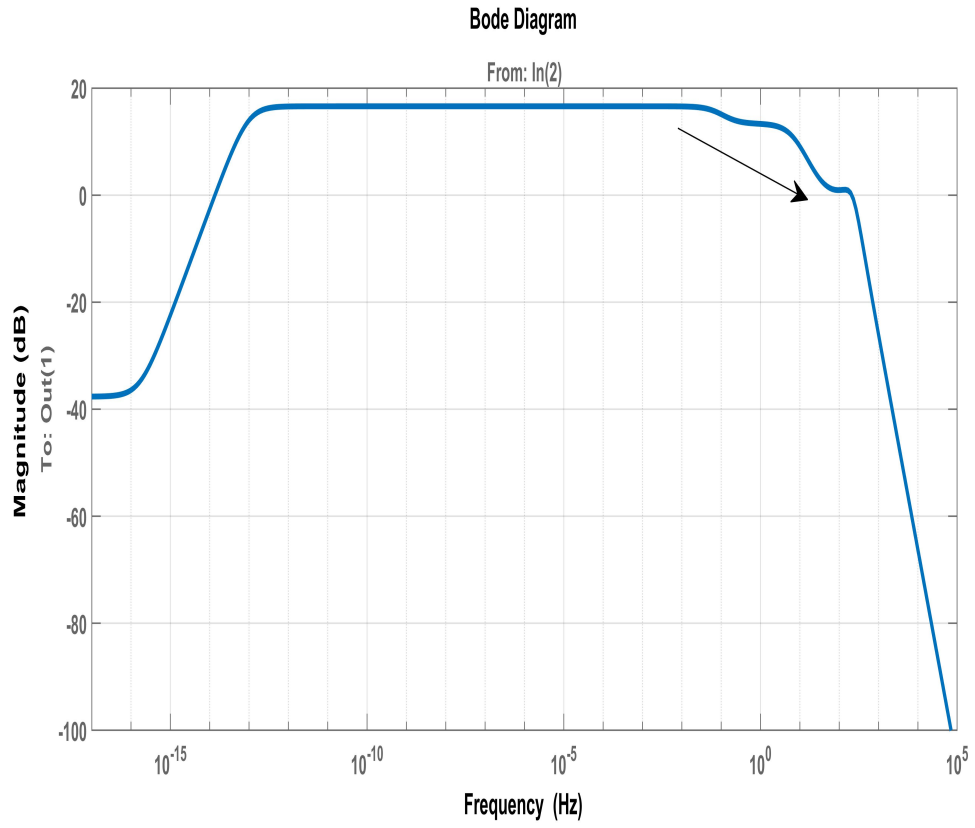
Figure 4.25 Magnitude gain relation between dz_{ground}/dt and $\bar{z}$
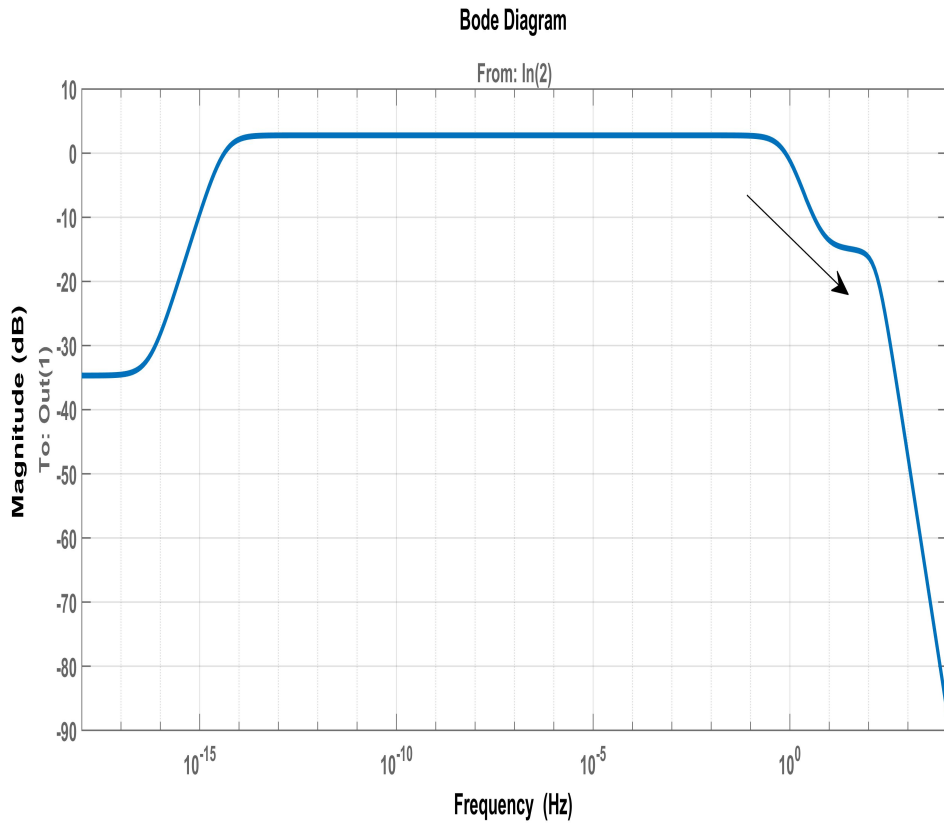
Figure 4.26 Magnitude gain relation relation between $d\alpha_{ground}/dt$ and $\bar{\alpha}$
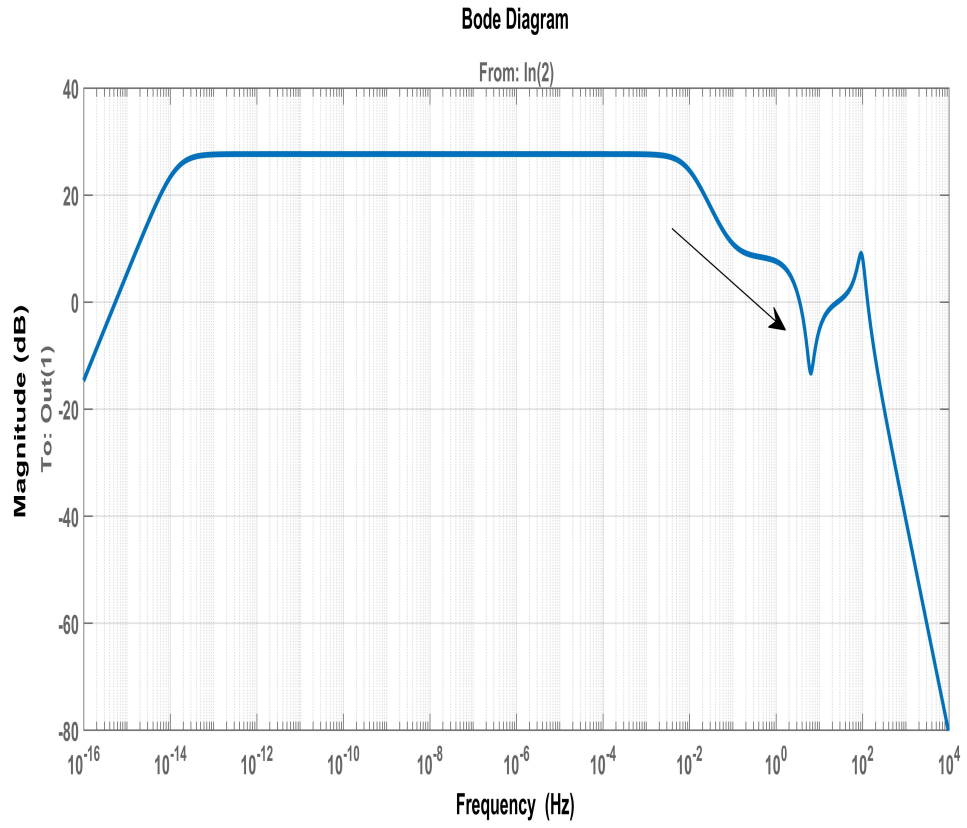
Figure 4.27 Magnitude gain relation between $d\beta_{ground}/dt$ and $\bar{\beta}$
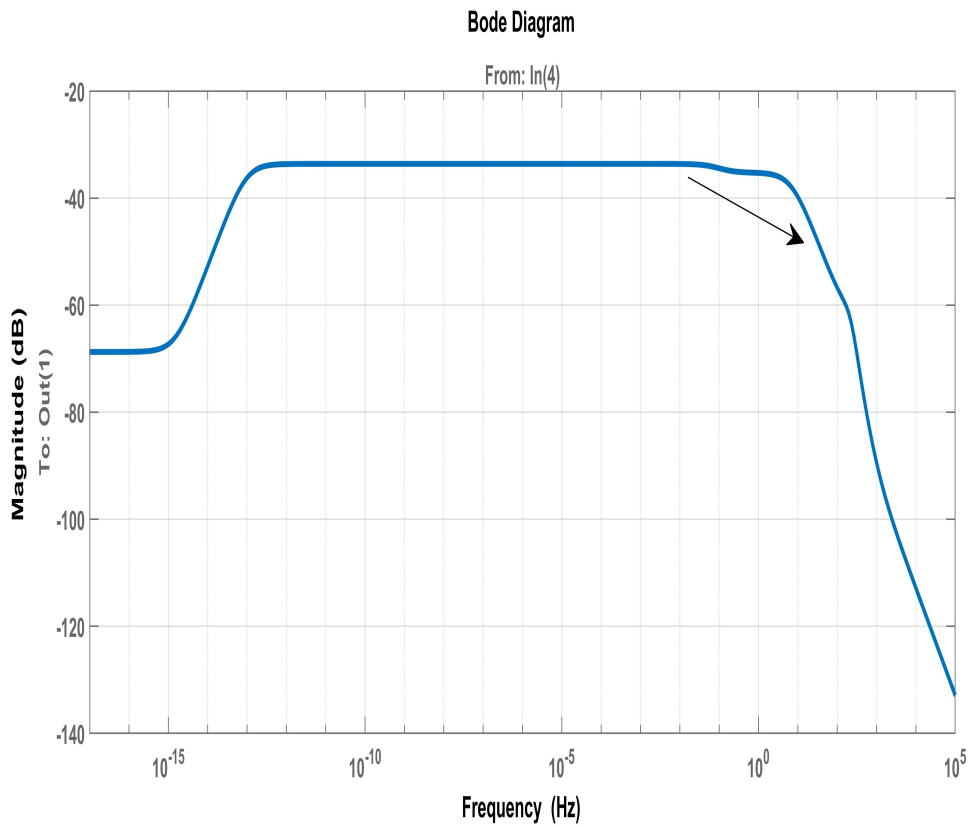
Figure 4.28 Magnitude gain relation between dF_d/dt and $\bar{z}$
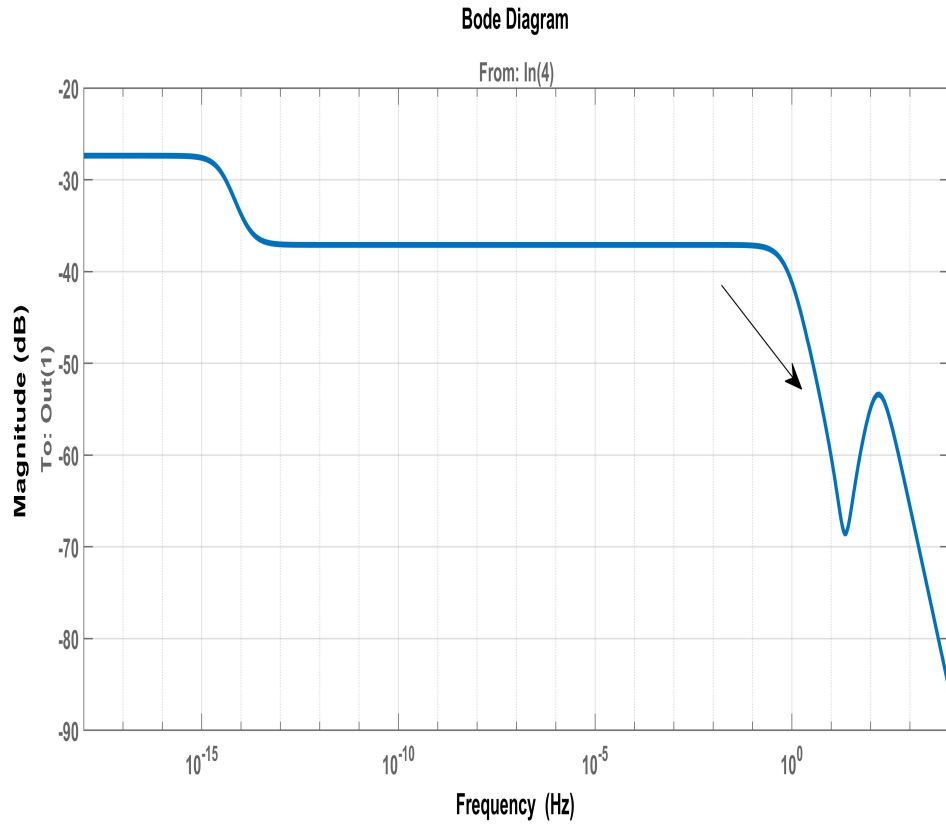
Figure 4.29 Magnitude gain relation between dT_α/dt and $\bar{\alpha}$
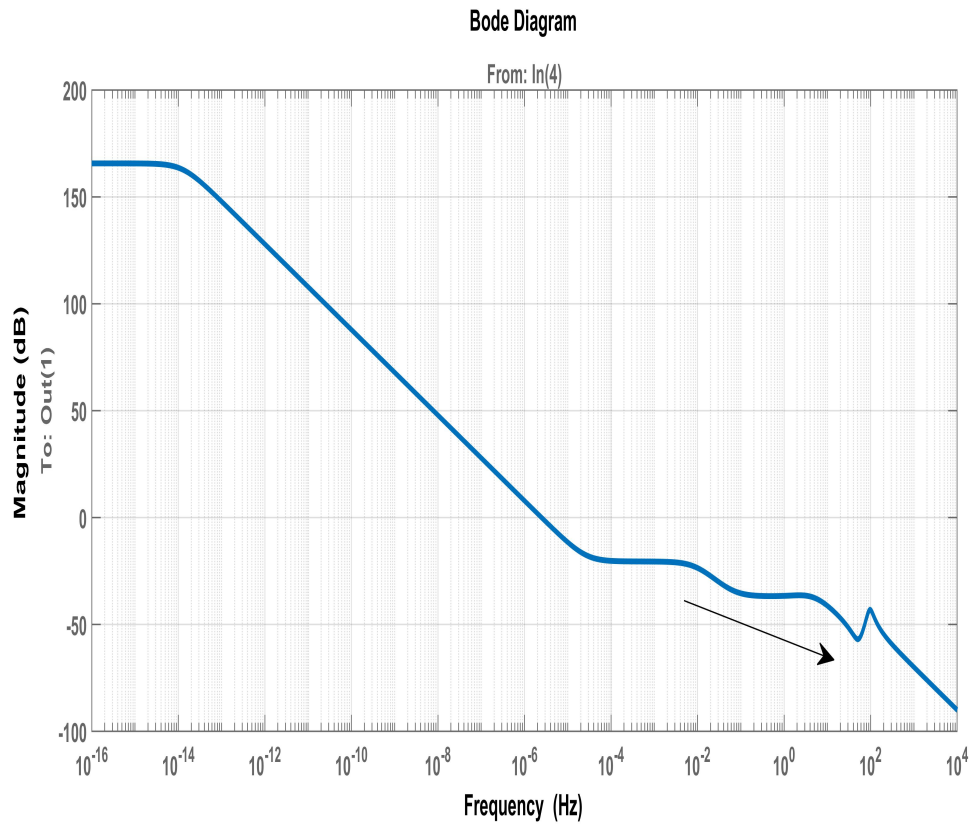
Figure 4.30 Magnitude gain relation between dT_β/dt and $\bar{\beta}$

54
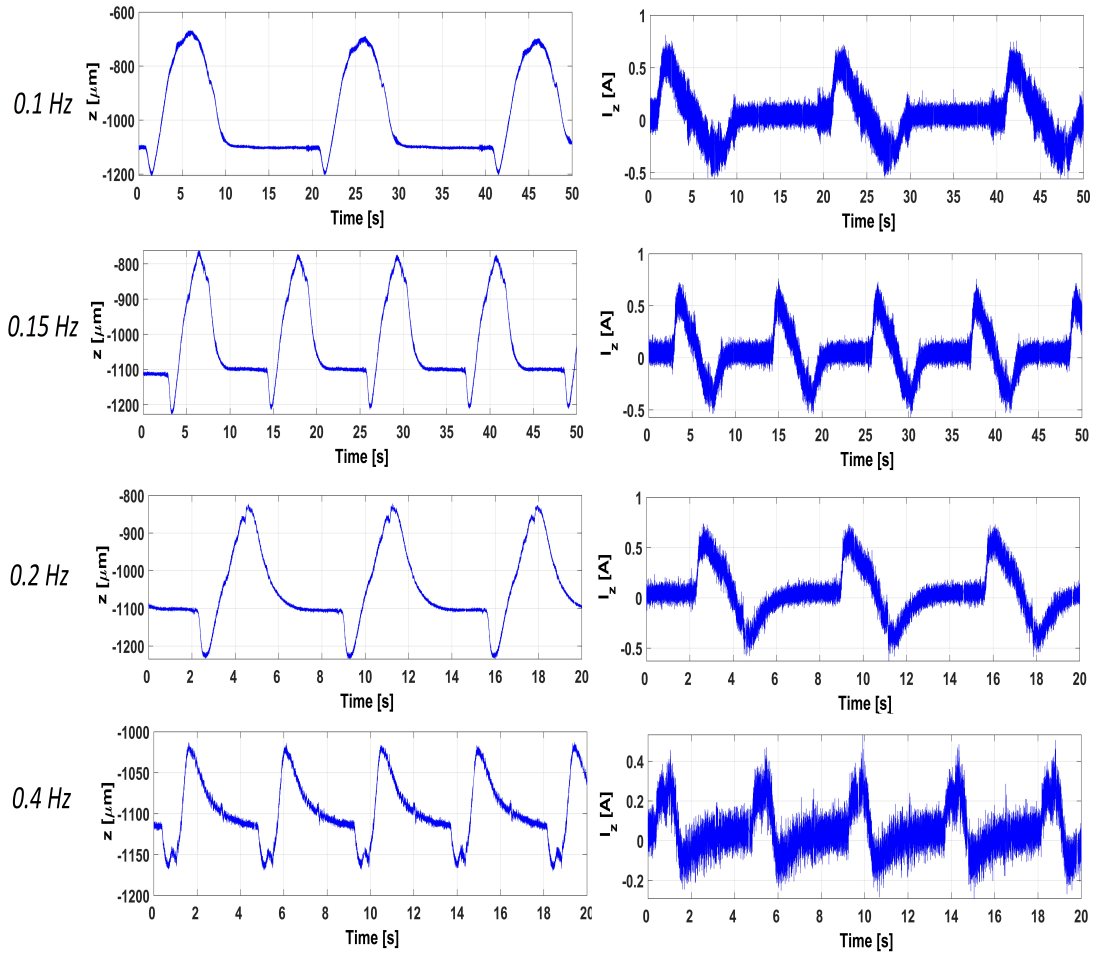
Figure 4.31 z for zero power with multi-directional variable disturbance case

Table 4.8 Norm values of z parameters for multi-directional variable disturbance case

Frequency	Norm z
0.1 Hz	1327.45442
0.15 Hz	1802.34321
0.2 Hz	2021.34321
0.4 Hz	2523.24592

Table 4.9 Norm values of I_z parameters for multi-directional variable disturbance case

Frequency	Norm I_z
0.1 Hz	2.23212
0.15 Hz	2.96705
0.2 Hz	3.34321
0.4 Hz	4.92912
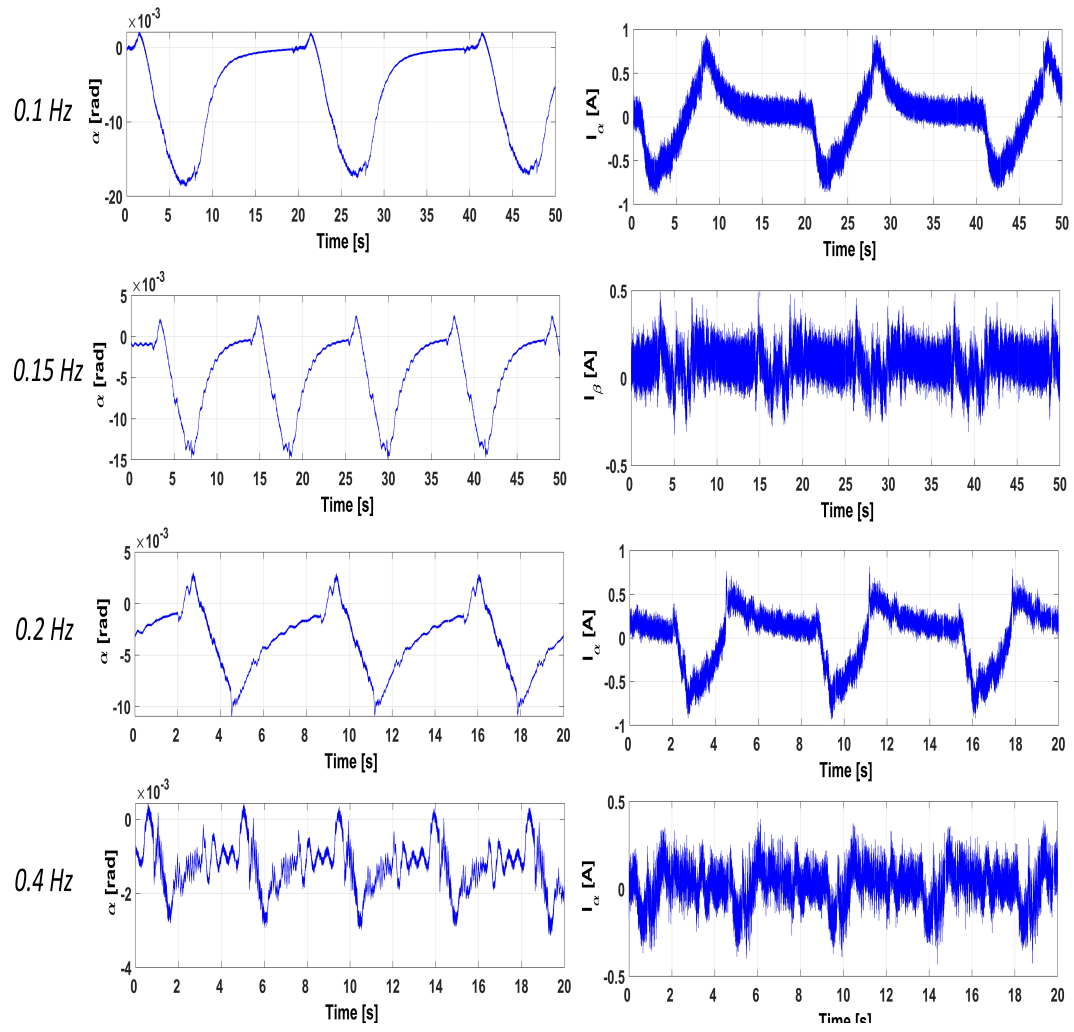
Figure 4.32 α for zero power with multi-directional variable disturbance case

Table 4.10 Norm values of α parameters for multi-directional variable disturbance case

Frequency	Norm α
0.1 Hz	1290.35292
0.15 Hz	1502.34692
0.2 Hz	1982.73912
0.4 Hz	2232.34938

Table 4.11 Norm values of I_α parameters for multi-directional variable disturbance case

Frequency	Norm I_α
0.1 Hz	2.94282
0.15 Hz	3.95329
0.2 Hz	4.53921
0.4 Hz	5.22311
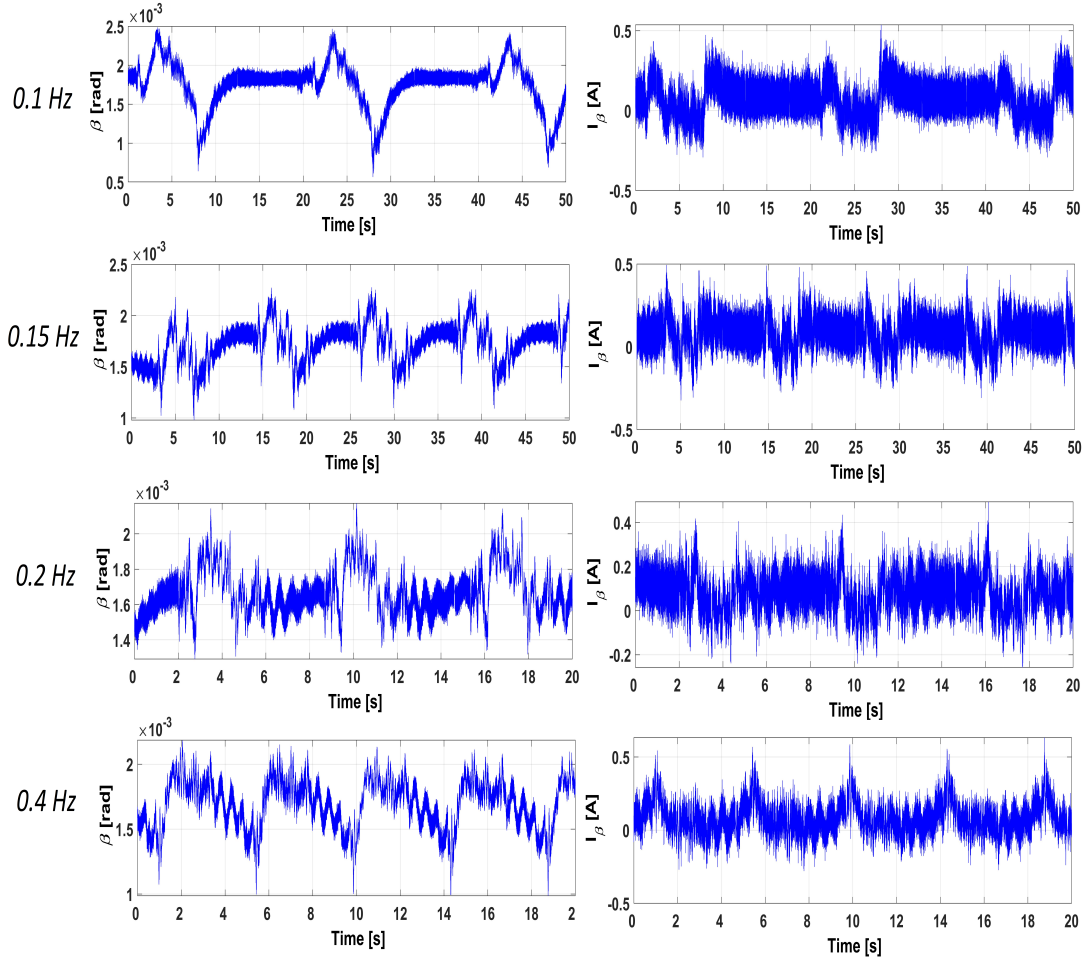
Figure 4.33 β for zero power with multi-directional variable disturbance case

Table 4.12 Norm values of β parameters for multi-directional variable disturbance case

Frequency	Norm β
0.1 Hz	1206.35932
0.15 Hz	1869.23592
0.2 Hz	2328.23912
0.4 Hz	2992.35342

Table 4.13 Norm values of I_β parameters for multi-directional variable disturbance case

Frequency	Norm I_β
0.1 Hz	3.12385
0.15 Hz	4.34212
0.2 Hz	5.00232
0.4 Hz	5.92912

4.6 Experiment : LMI $\mathcal{H}_2$ Full State-Feedback Zero Power Controller Performance with Direct Disturbance as Force

In this experiment, the system's pseudo-infinite stiffness against direct disturbance as force has been studied. The experiment has been conducted for $1\,kg$ direct disturbance on the geometric center of m_2 isolation mass. To prove the system's ability of acting as if it is a virtual spring that has pseudo-infinite stiffness, the force is applied at 4th second and unloaded at 8th second. As given in Fig. 4.28, Fig. 4.29 and Fig. 4.30 previously, the system behavior against to the step input as direct disturbance can be observed from the bode magnitude plot at $1\,Hz$. While the frequency increases, the bode magnitude plot decreases, which means that the system does not show extensive overshoot behavior against the direct disturbances. In Fig. 4.34, Fig. 4.35 and Fig. 4.36, it can be seen that the system shows almost perfect zero-power property with comparatively low settling-times against static direct disturbances.
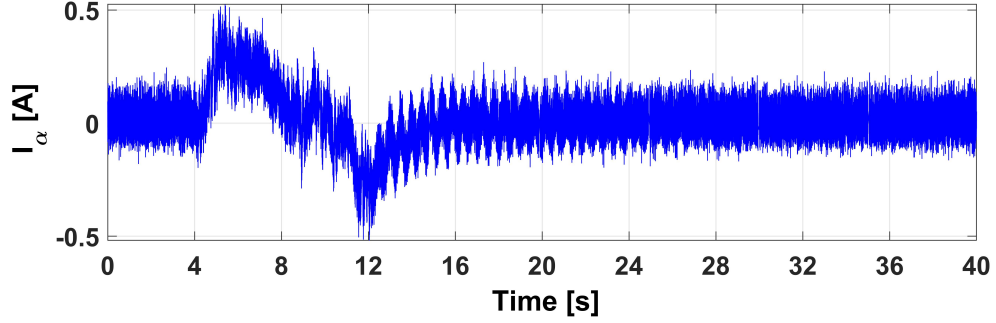
Figure 4.34 I_α for zero power with 1 kg direct disturbance case
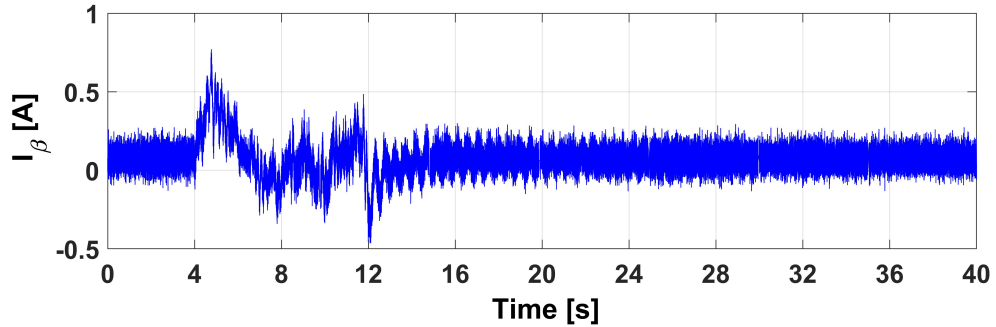
Figure 4.35 I_β for zero power with 1 kg direct disturbance case

One can observe that even though the force is applied to the geometric center of m_2 isolation mass, rotational axis currents still change. The main reason of this is that mechanic tolerance error in the setup's construction. From Fig. 4.34 and Fig. 4.35 and , it can be clearly seen that the system shows zero-power behavior against to torque parameter.

Obtaining the numeric value of positive stiffness parameter is not possible at this point. The main reason of this situation is that; $z_1 - z_{ground}$, $\alpha_1 - \alpha_{ground}$ and $\beta_1 - \beta_{ground}$
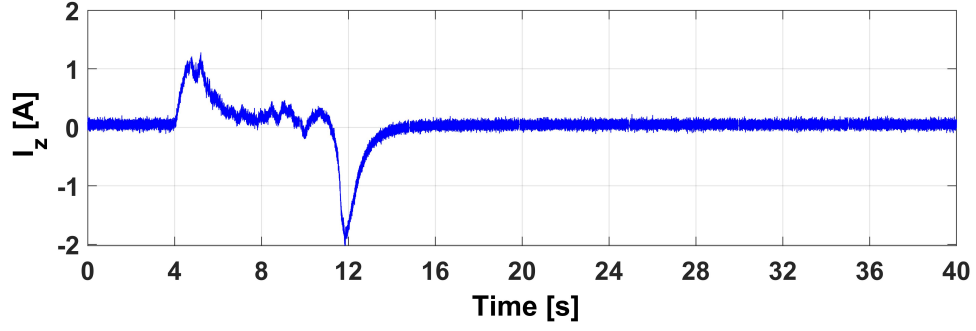
Figure 4.36 I_z for zero power with 1 kg direct disturbance case

measurements do not exist. However, due to the movement of lower mass is negligible against 1 kg force, negative stiffness can be assumed that it is pseudo-infinite stiffness for this case. Therefore, pseudo-infinite stiffness for each axis can be measured by from Fig. 4.37, Fig. 4.38 and Fig. 4.39. The average pseudo-infinite stiffness parameter for each axis can be obtained, and they are as follows; $k_{pz} = 20.000N/m$, $k_{p\alpha} = 40.000Nm/rad$ and $k_{p\beta} = 60.000Nm/rad$.

Table 4.14 Average stiffness for each axis

Axis	Stiffness value
z	20.000 N/m
α	40.000 Nm/rad
β	60.000 Nm/rad
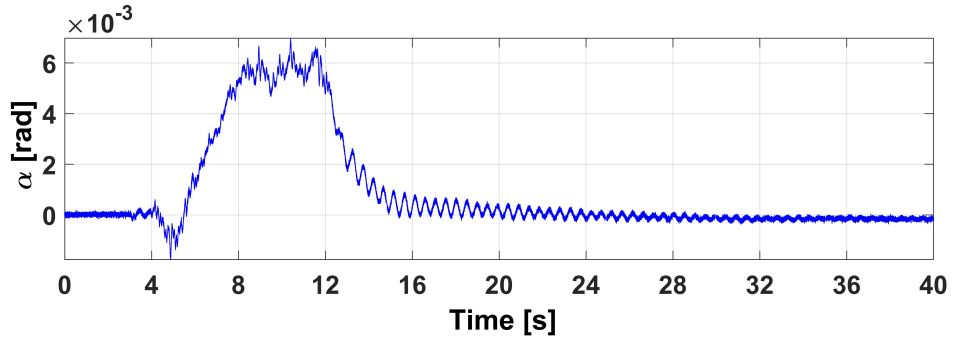
Figure 4.37 α for zero power with 1 kg direct disturbance case

Figure 4.38 β for zero power with 1 kg direct disturbance case

59
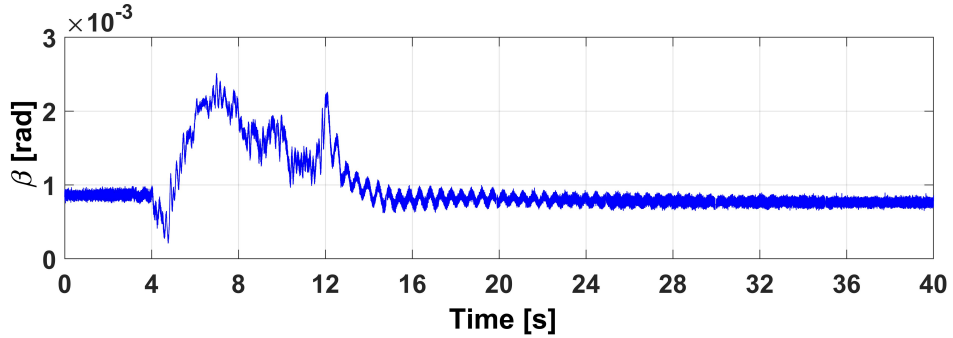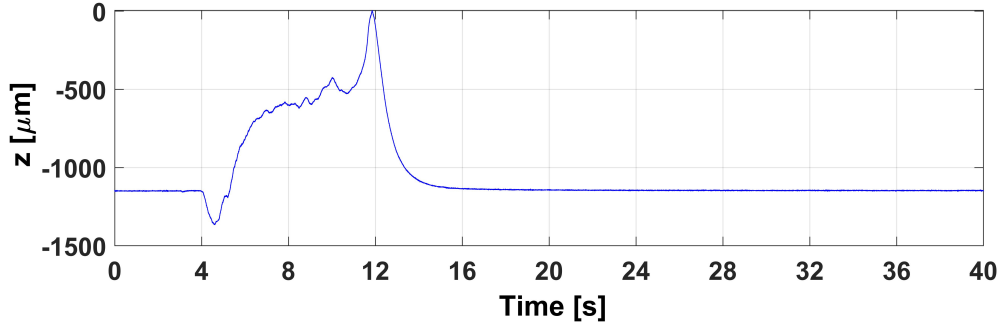
Figure 4.39 z for zero power with 1 kg direct disturbance case
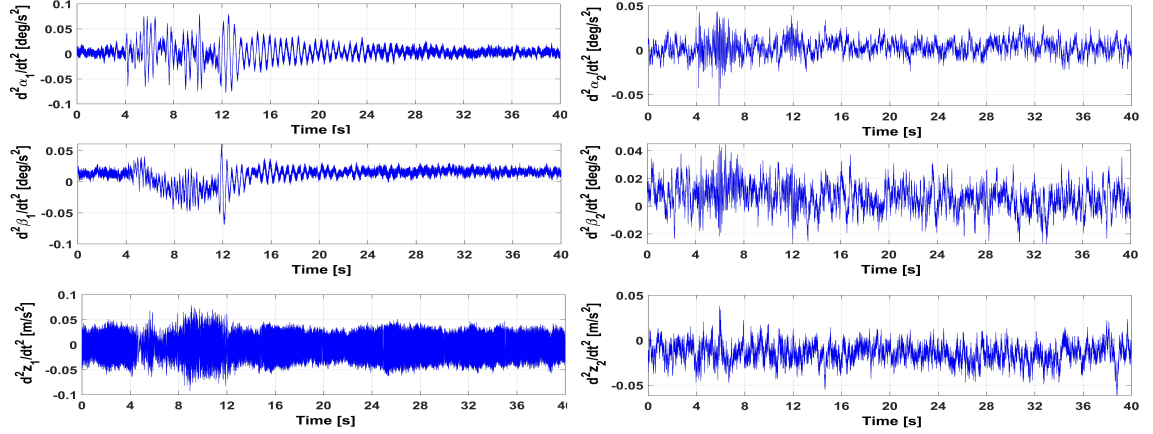
Figure 4.40 Acceleration parameters for zero power with 1 kg direct disturbance case

From Fig. 4.40, one can easily see that m_1 has higher frequency oscillations on each axis compared to m_2. This is an indirect result of vibration isolation of m_2 isolation mass. As mentioned before, the mechanic disturbance is applied only to m_2, whereas vibration isolation scenario is also designed for m_2. So, energy given by the disturbance is being transferred from m_2 to m_1 for vibration isolation, which means that the energy dissipation is being achieved by high frequency acceleration parameter changing on m_1. This issue can also be seen from norm values for each movement axis of m_1 and m_2 in Fig. 4.15.

Table 4.15 Norm values of acceleration parameters

Parameter	Value
$\ddot{\alpha}_1$	0.411239
$\ddot{\beta}_1$	0.422212
$\ddot{z}_1$	0.423122
$\ddot{\alpha}_2$	0.396312
$\ddot{\beta}_2$	0.387277
$\ddot{z}_2$	0.380291

60

5
Conclusion

In magnetic levitation discipline, a review has been conducted between the proposed control method and other control methods popularly used for vibration control applications. It has clearly been stated that the proposed method is more appropriate for vibration isolation applications in terms of multi-objectivity, degrees-of-freedom capability, energy efficiency and robustness at varying frequencies.

Synthesizing $\mathscr{H}_2$ controllers by using the outlined LMIs is a suitable and relatively easy, and applicable. For both displacement and force disturbances, pseudo-infinite stiffness with zero-power performances of LMI controllers for z, α and β axes have been tested and evaluated at some critical frequency values.

LMI controllers show satisfying performance under varying frequency disturbances with minimized $\mathscr{H}_2$ norm for each axis of 4-pole hybrid electromagnet. The system performs favorable outputs at varying frequencies for many different drastic scenarios, such as ground disturbance, direct disturbance and multi-directional disturbances.

Similar studies in this literature deal with only one directional disturbance for air gap reference tracking. This issue can easily be solved with current and gap feedback data, so acceleration feedback data is not commonly necessary. Another point, accelerometers are expensive devices for both industrial and academic researches. In this study, it has been stated and tested that acceleration feedback data can be very useful to deal with multi-directional disturbances. Moreover, it has been shown that using acceleration feedback data with air gap feedback data can stabilize air gap in micro scale on the isolation mass.

Due to the high non-linearity and coupling effects that belong to the real physical system, sensor equipment is used to measure each state in the state vector instead of using any observer structure.

One disadvantage of the proposed method is that; for this study, the magnitude of direct disturbance and the magnitude of ground disturbance are known, produced by

precise step motors. In magnetic levitation perspective, measuring direct disturbance magnitude can be achieved by measuring levitation gap in the absence of ground disturbance. Thus, measuring the magnitude of direct disturbance is not a complicated process. However, measuring the magnitude of ground disturbance is very difficult in real world situations. Because any measuring process requires "a reference point". If the reference point, which is ground in this case, moves, how can the ground disturbance be measured? Therefore, calculating pseudo-infinite stiffness success in real world situations is troublesome, requires different estimation methods.

The proposed system is applicable especially for space technologies requiring high precision vibration isolation with low energy consumption.

A
FEM Analysis Results

Table A.1 Iterations to investigate current, gap and force relation

#	i_z [A]	z [mm]	F_z [N]	#	i_z [A]	z [mm]	F_z [N]	#	i_z [A]	z [mm]	F_z [N]	#	i_z [A]	z [mm]	F_z [N]
1	-4	2	-74	26	-2	7	-17	51	1	2	316	76	3	7	86
2	-4	3	-42	27	-2	8	-11	52	1	3	198	77	3	8	67
3	-4	4	-26	28	-2	9	-8.3	53	1	4	130	78	3	9	53
4	-4	5	-16	29	-2	10	-6.3	54	1	5	92	79	3	10	43
5	-4	6	-11	30	-2	11	-4.1	55	1	6	67	80	3	11	35
6	-4	7	-7.4	31	-1	2	-189	56	1	7	50	81	4	2	473
7	-4	8	-3.2	32	-1	3	-111	57	1	8	39	82	4	3	353
8	-4	9	-2.4	33	-1	4	-72	58	1	9	30	83	4	4	257
9	-4	10	-1.6	34	-1	5	-49	59	1	10	24	84	4	5	187
10	-4	11	-0.5	35	-1	6	-35	60	1	11	19	85	4	6	140
11	-3	2	-101	36	-1	7	-25	61	2	2	379	86	4	7	108
12	-3	3	-57	37	-1	8	-18	62	2	3	252	87	4	8	84
13	-3	4	-35	38	-1	9	-14	63	2	4	169	88	4	9	68
14	-3	5	-23	39	-1	10	-10	64	2	5	120	89	4	10	56
15	-3	6	-16	40	-1	11	-8.3	65	2	6	88	90	4	11	45
16	-3	7	-10	41	0	2	252	66	2	7	67	91	5	2	503
17	-3	8	-7.1	42	0	3	153	67	2	8	52	92	5	3	393
18	-3	9	-4.7	43	0	4	97	68	2	9	41	93	5	4	297
19	-3	10	-3.3	44	0	5	68	69	2	10	33	94	5	5	228
20	-3	11	-1.3	45	0	6	50	70	2	11	26	95	5	6	170
21	-2	2	-140	46	0	7	36	71	3	2	429	96	5	7	132
22	-2	3	-81	47	0	8	27	72	3	3	303	97	5	8	105
23	-2	4	-50	48	0	9	21	73	3	4	212	98	5	9	84
24	-2	5	-34	49	0	10	16	74	3	5	152	99	5	10	69
25	-2	6	-24	50	0	11	12	75	3	6	112	100	5	11	57

Table A.2 Iterations to investigate current, gap and torque relation

#	$i_{\alpha,\beta}$ [A]	z [mm]	$T_{\alpha,\beta}$ [Nm]	#	$i_{\alpha,\beta}$ [A]	z [mm]	$T_{\alpha,\beta}$ [Nm]	#	$i_{\alpha,\beta}$ [A]	z [mm]	$T_{\alpha,\beta}$ [Nm]	#	$i_{\alpha,\beta}$ [A]	z [mm]	$T_{\alpha,\beta}$ [Nm]
1	-4	2	-9.75	26	-2	7	-4.51	51	1	2	7.54	76	3	7	8.98
2	-4	3	-9.22	27	-2	8	-4.24	52	1	3	6.64	77	3	8	8.87
3	-4	4	-8.15	28	-2	9	-3.10	53	1	4	5.52	78	3	9	8.54
4	-4	5	-7.61	29	-2	10	-2.90	54	1	5	4.51	79	3	10	8.21
5	-4	6	-6.25	30	-2	11	-0.62	55	1	6	4.23	80	3	11	7.82
6	-4	7	-5.62	31	-1	2	-5.24	56	1	7	3.51	81	4	2	7.62
7	-4	8	-4.42	32	-1	3	-4.52	57	1	8	3.32	82	4	3	7.32
8	-4	9	-3.22	33	-1	4	-4.33	58	1	9	2.52	83	4	4	7.21
9	-4	10	-2.54	34	-1	5	-3.81	59	1	10	2.33	84	4	5	6.80
10	-4	11	-1.47	35	-1	6	-3.55	60	1	11	1.21	85	4	6	6.67
11	-3	2	-9.17	36	-1	7	-2.84	61	2	2	8.21	86	4	7	6.54
12	-3	3	-8.15	37	-1	8	-2.62	62	2	3	7.51	87	4	8	6.19
13	-3	4	-7.22	38	-1	9	-2.31	63	2	4	7.22	88	4	9	5.79
14	-3	5	-6.64	39	-1	10	-1.22	64	2	5	6.21	89	4	10	5.62
15	-3	6	-5.51	40	-1	11	-0.21	65	2	6	5.52	90	4	11	5.42
16	-3	7	-4.39	41	0	2	0.81	66	2	7	4.25	91	5	2	5.34
17	-3	8	-3.28	42	0	3	0.65	67	2	8	3.64	92	5	3	5.25
18	-3	9	-2.45	43	0	4	0.52	68	2	9	2.52	93	5	4	4.99
19	-3	10	-1.58	44	0	5	0.45	69	2	10	2.22	94	5	5	4.91
20	-3	11	-0.55	45	0	6	0.42	70	2	11	2.11	95	5	6	4.87
21	-2	2	-7.16	46	0	7	0.38	71	3	2	8.52	96	5	7	3.99
22	-2	3	-6.52	47	0	8	0.25	72	3	3	8.42	97	5	8	3.78
23	-2	4	-6.23	48	0	9	0.22	73	3	4	7.88	98	5	9	3.64
24	-2	5	-5.51	49	0	10	0.15	74	3	5	7.76	99	5	10	3.25
25	-2	6	-5.20	50	0	11	0.12	75	3	6	6.56	100	5	11	3.12

Table A.3 Iterations to investigate current, gap and magnetic saturation

| #	$i_{\alpha,\beta}$ [A]	z [mm]	B_m [T]	#	$i_{\alpha,\beta}$ [A]	z [mm]	B_m [T]	#	$i_{\alpha,\beta}$ [A]	z [mm]	B_m [T]	#	$i_{\alpha,\beta}$ [A]	z [mm]	B_m [T]
1	-4	2	1.98	26	-2	7	1.23	51	1	2	1.52	76	3	7	0.67
2	-4	3	1.76	27	-2	8	1.20	52	1	3	1.44	77	3	8	0.61
3	-4	4	1.62	28	-2	9	1.15	53	1	4	1.39	78	3	9	0.54
4	-4	5	1.59	29	-2	10	0.62	54	1	5	1.35	79	3	10	0.51
5	-4	6	1.45	30	-2	11	0.51	55	1	6	1.29	80	3	11	0.49
6	-4	7	1.32	31	-1	2	1.69	56	1	7	1.22	81	4	2	0.41
7	-4	8	1.26	32	-1	3	1.55	57	1	8	1.22	82	4	3	0.35
8	-4	9	1.21	33	-1	4	1.42	58	1	9	0.44	83	4	4	0.25
9	-4	10	0.96	34	-1	5	1.39	59	1	10	0.32	84	4	5	0.18
10	-4	11	0.76	35	-1	6	1.25	60	1	11	0.22	85	4	6	0.12
11	-3	2	0.64	36	-1	7	1.19	61	2	2	1.32	86	4	7	0.06
12	-3	3	1.86	37	-1	8	1.05	62	2	3	1.21	87	4	8	0.04
13	-3	4	1.72	38	-1	9	0.91	63	2	4	1.12	88	4	9	0.02
14	-3	5	1.61	39	-1	10	0.86	64	2	5	0.91	89	4	10	0.01
15	-3	6	1.56	40	-1	11	0.61	65	2	6	0.82	90	4	11	0.00
16	-3	7	1.48	41	0	2	0.51	66	2	7	0.72	91	5	2	0.09
17	-3	8	1.32	42	0	3	0.45	67	2	8	0.61	92	5	3	0.07
18	-3	9	1.29	43	0	4	0.38	68	2	9	0.49	93	5	4	0.07
19	-3	10	0.65	44	0	5	0.35	69	2	10	0.20	94	5	5	0.06
20	-3	11	0.41	45	0	6	0.30	70	2	11	0.11	95	5	6	0.06
21	-2	2	1.72	46	0	7	0.28	71	3	2	1.21	96	5	7	0.03
22	-2	3	1.69	47	0	8	0.23	72	3	3	1.02	97	5	8	0.00
23	-2	4	1.54	48	0	9	0.20	73	3	4	0.92	98	5	9	0.00
24	-2	5	1.42	49	0	10	0.12	74	3	5	0.86	99	5	10	0.00
25	-2	6	1.39	50	0	11	0.07	75	3	6	0.72	100	5	11	0.00

B
Analytical and Experimental Bode Plots
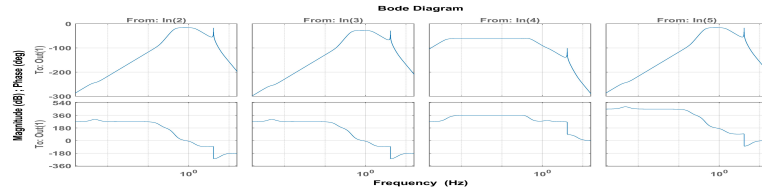
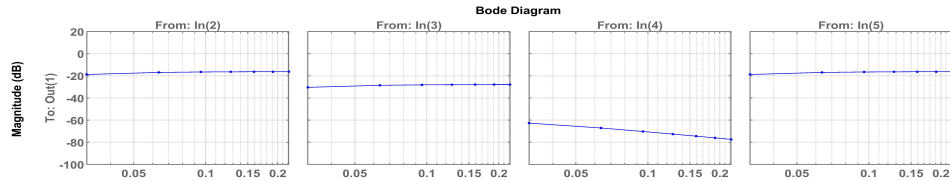**Figure B.1** Analytical bode plots for $\frac{d(z_{ref}-\triangle z)}{dt}$

Figure B.2 Experimental bode plots for $\frac{d(z_{ref}-\triangle z)}{dt}$
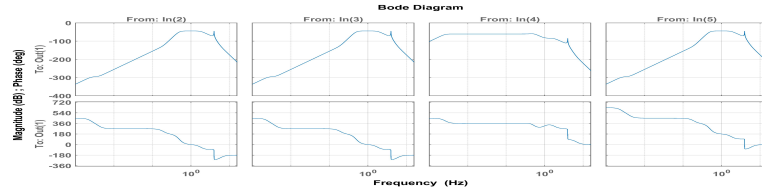

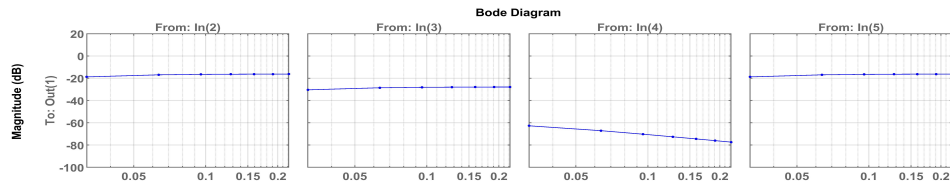**Figure B.3** Analytical bode plots for $\frac{d(\alpha_{ref}-\triangle \alpha)}{dt}$

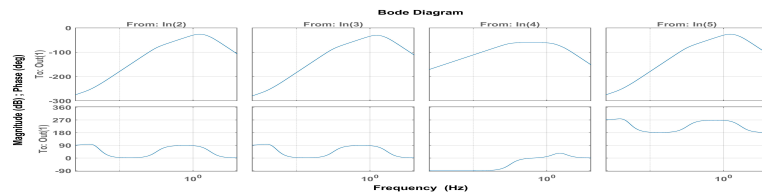**Figure B.4** Experimental bode plots for $\frac{d(\alpha_{ref}-\triangle \alpha)}{dt}$

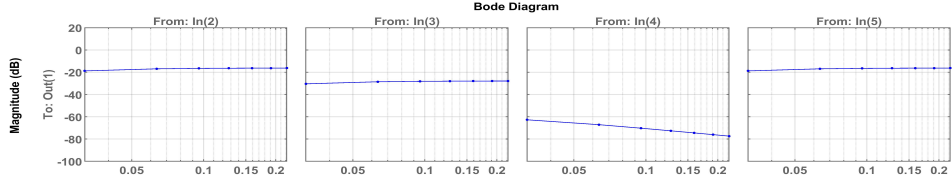**Figure B.5** Analytical bode plots for $\frac{d(\beta_{ref}-\triangle \beta)}{dt}$

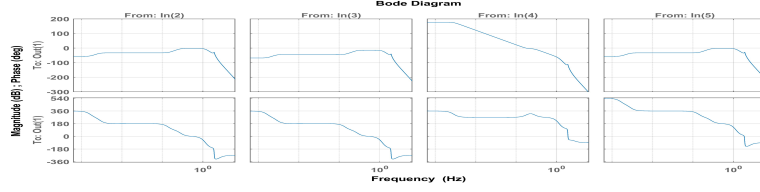**Figure B.6** Experimental bode plots for $\frac{d(\beta_{ref}-\triangle\beta)}{dt}$

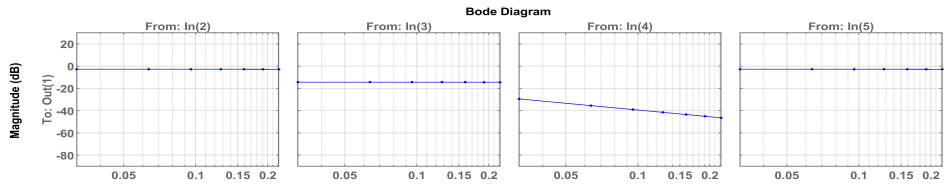**Figure B.7** Analytical bode plots for $z_{ref}-\triangle z$

Figure B.8 Experimental bode plots for $z_{ref}-\triangle z$
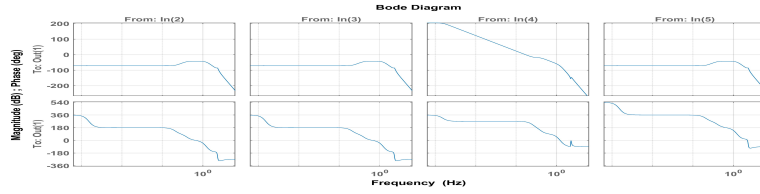

Figure B.9 Analytical bode plots for $\alpha_{ref}-\triangle\alpha$
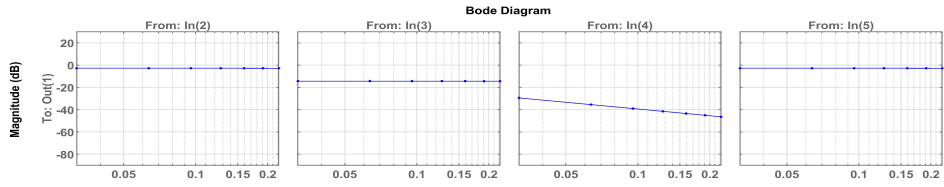

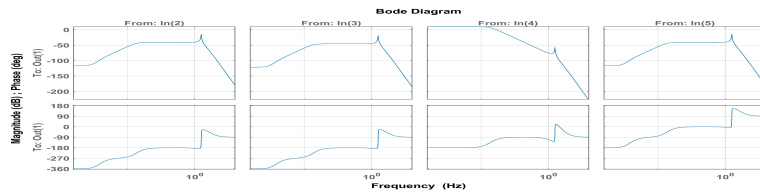**Figure B.10** Experimental bode plots for $\alpha_{ref}-\triangle\alpha$

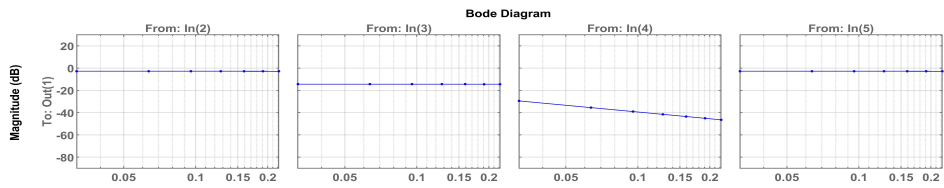

Figure B.11 Analytical bode plots for $\beta_{ref}-\triangle\beta$

Figure B.12 Experimental bode plots for $\beta_{ref}-\triangle\beta$
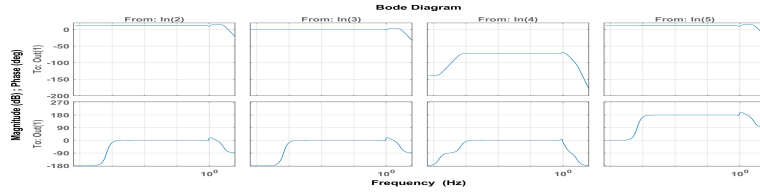
Figure B.13 Analytical bode plots for $\frac{d^2 \triangle z_1}{dt^2}$

Figure B.14 Experimental bode plots for $\frac{d^2 \triangle z_1}{dt^2}$

Figure B.15 Analytical bode plots for $\frac{d^2 \triangle \alpha_1}{dt^2}$

Figure B.16 Experimental bode plots for $\frac{d^2 \triangle \alpha_1}{dt^2}$

Figure B.17 Analytical bode plots for $\frac{d^2 \triangle \beta_1}{dt^2}$
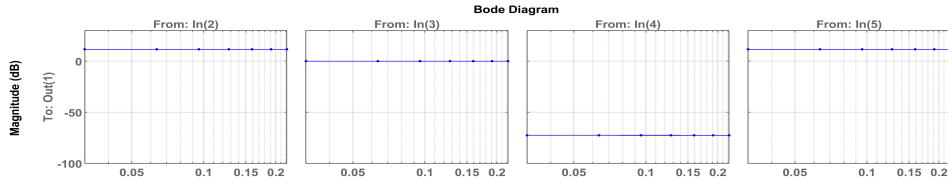
Figure B.18 Experimental bode plots for $\frac{d^2 \triangle \beta_1}{dt^2}$
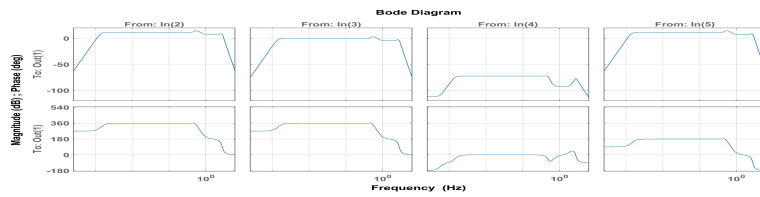
Figure B.19 Analytical bode plots for $\frac{d^2 \triangle z_2}{dt^2}$
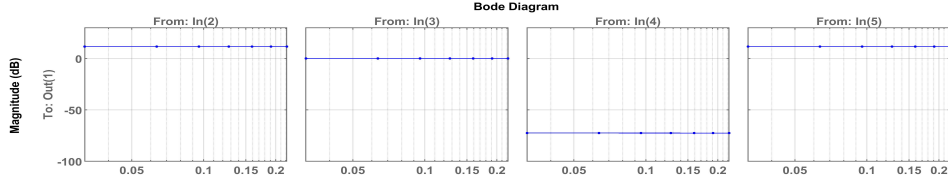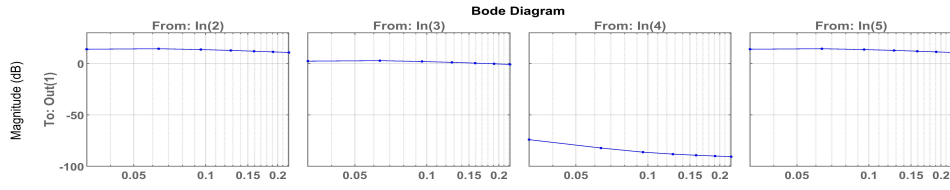
Figure B.20 Experimental bode plots for $\frac{d^2\triangle z_2}{dt^2}$
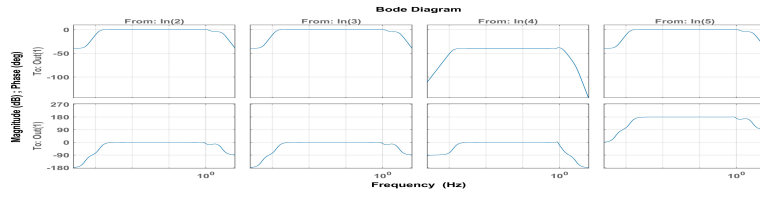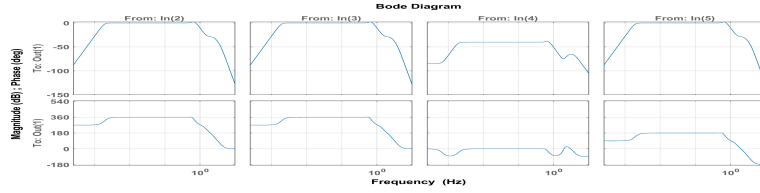

Figure B.21 Analytical bode plots for $\frac{d^2\triangle\alpha_2}{dt^2}$
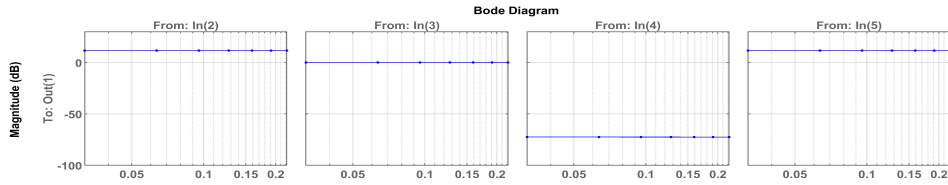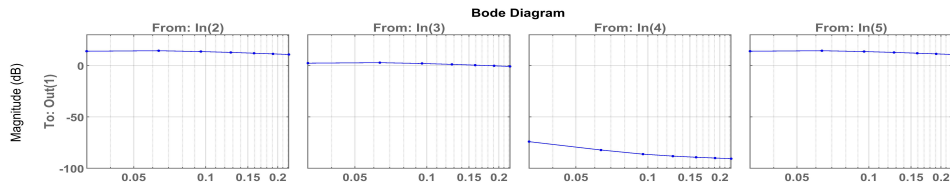

Figure B.22 Experimental bode plots for $\frac{d^2\triangle\alpha_2}{dt^2}$
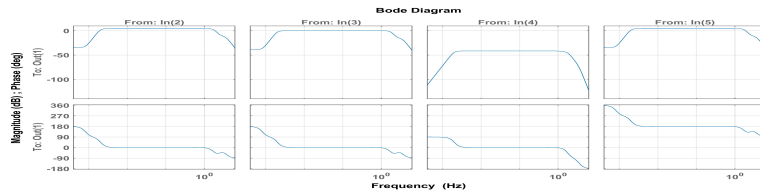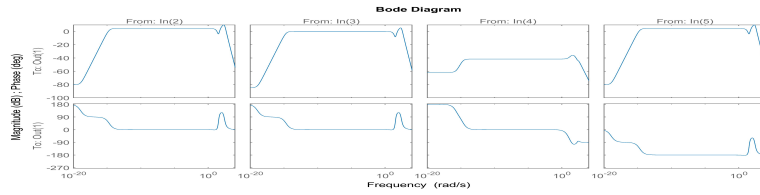

Figure B.23 Analytical bode plots for $\frac{d^2\triangle\beta_2}{dt^2}$
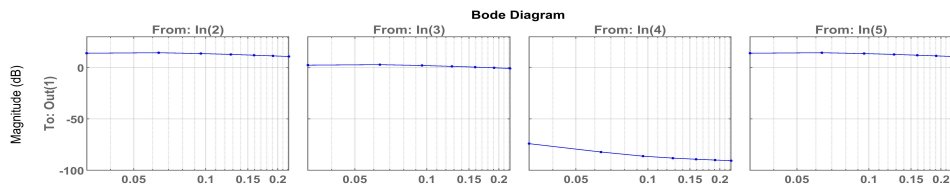
Figure B.24 Experimental bode plots for $\frac{d^2\triangle\beta_2}{dt^2}$
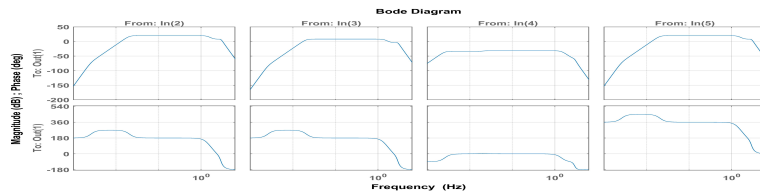
Figure B.25 Analytical bode plots for $\triangle i_z$
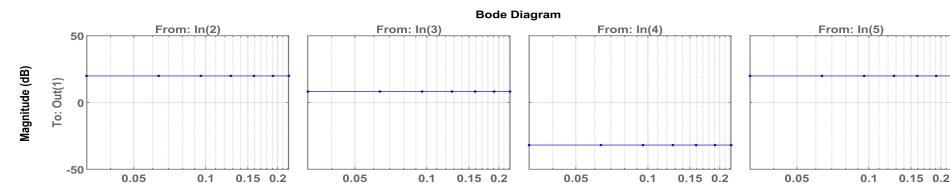
Figure B.26 Experimental bode plots for $\triangle i_z$

70
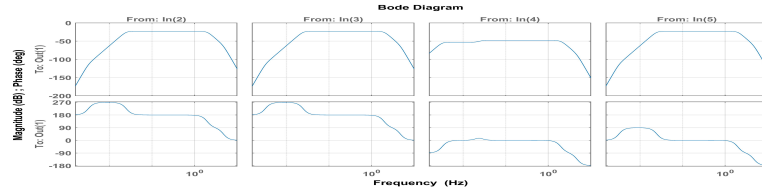
Figure B.27 Analytical bode plots for $\triangle i_\alpha$
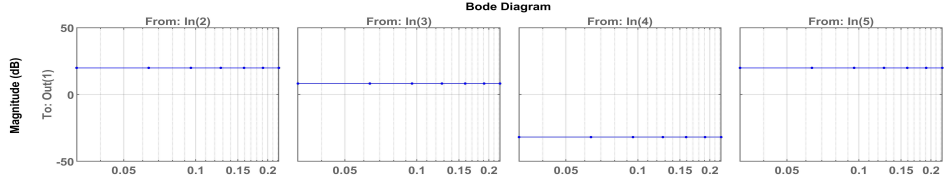
Figure B.28 Experimental bode plots for $\triangle i_\alpha$
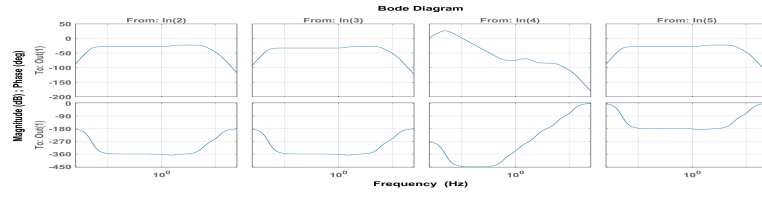
Figure B.29 Analytical bode plots for $\triangle i_\beta$
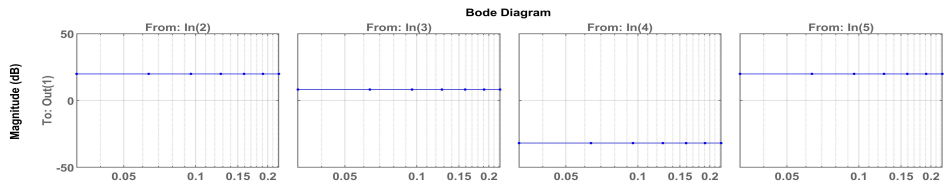
Figure B.30 Experimental bode plots for $\triangle i_\beta$
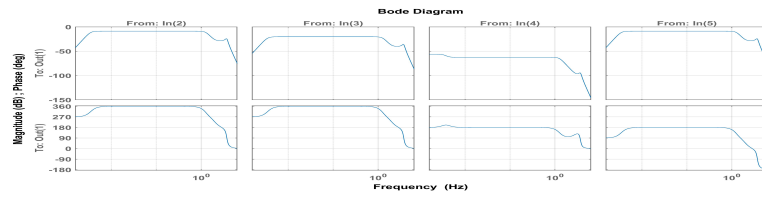
Figure B.31 Analytical bode plots for $\int (0 - V_z) dt$

Figure B.32 Experimental bode plots for $\int(0-V_z)dt$

Figure B.33 Analytical bode plots for $\int(0-V_\alpha)dt$

Figure B.34 Experimental bode plots for $\int(0-V_\alpha)dt$
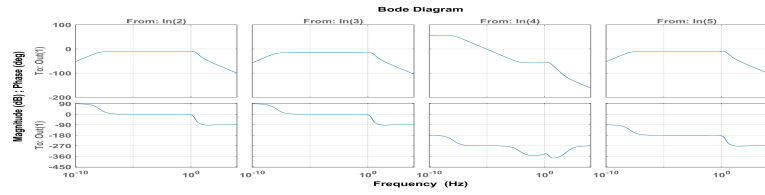
Figure B.35 Analytical bode plots for $\int(0-V_\beta)dt$
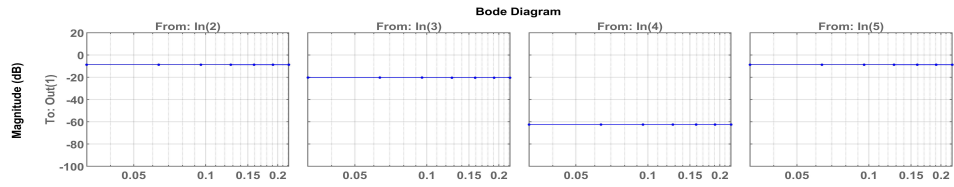
Figure B.36 Experimental bode plots for $\int(0-V_\beta)dt$

References

Adina et al. (2016). "State feedback and proportional-integral-derivative control of a magnetic levitation system". In: *IEEE 14th International Symposium on Intelligent Systems and Informatics (SISY), Subotica, Serbia*.

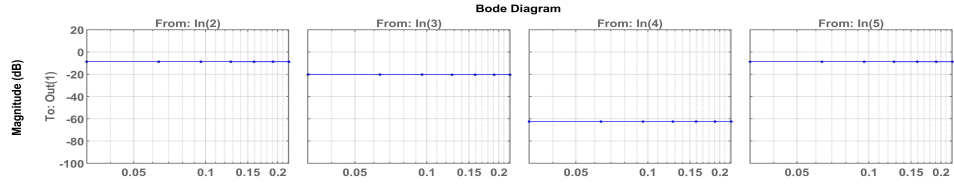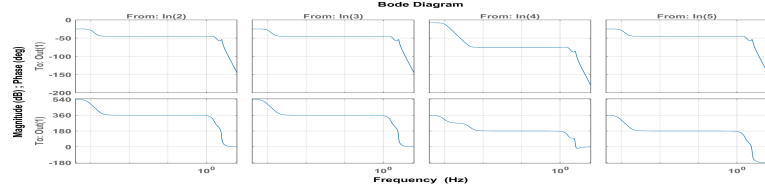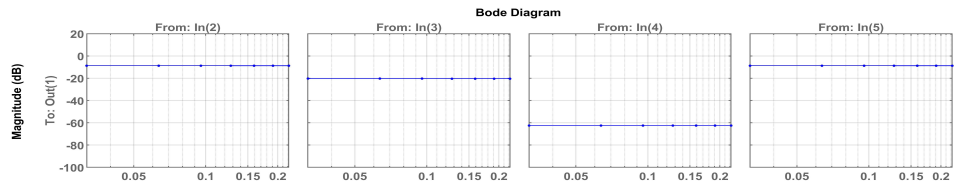Ahn, Hyeong-Joon, KangJo Hwang, and Duc Canh Nguyen (2017). "Eddy current damper for passive reaction force compensation of a linear motor motion stage". In: *Proceedings of the Institution of Mechanical Engineers, Part I: Journal of Systems and Control Engineering* 231.5, pp. 360–366. DOI: 10.1177/0959651816650568.

Ahsan, M., N. Masood, and F. Wali (Sept. 2013). "Control of a magnetic levitation system using non-linear robust design tools". In: *2013 3rd IEEE International Conference on Computer, Control and Communication (IC4)*, pp. 1–6. DOI: 10.1109/IC4.2013.6653741.

Atlihan, M., M. Bucak, and K. Erkan (Sept. 2015). "Horizontal I-PD position control of a levitated hybrid electromagnet driven by 3 phase ac long stator L-PMSM". In: *2015 Intl Aegean Conference on Electrical Machines Power Electronics (ACEMP), 2015 Intl Conference on Optimization of Electrical Electronic Equipment (OPTIM) 2015 Intl Symposium on Advanced Electromechanical Motion Systems (ELECTROMOTION)*, pp. 545–551. DOI: 10.1109/OPTIM.2015.7427055.

Baig and Mahmood (Dec. 2016). "Robust control design of a magnetic levitation system". In: *19th International Multi-Topic Conference (INMIC), Islamabad, Pakistan*.

Boyd, S. et al. (1994). *Linear Matrix Inequalities in System and Control Theory*. Society for Industrial and Applied Mathematics. DOI: 10.1137/1.9781611970777. URL: https://epubs.siam.org/doi/abs/10.1137/1.9781611970777.

Chiang et al. (Apr. 2013). "Integral backstepping sliding mode control of a magnetic ball suspension system". In: *2013 IEEE 10th International Conference on Power Electronics and Drive Systems (PEDS)*, pp. 44–49. DOI: 10.1109/PEDS.2013.6526986.

Cho, Kato, and Spilman (Feb. 1993). "Sliding mode and classical controllers in magnetic levitation systems". In: *IEEE Control Systems Magazine* 13.1, pp. 42–48. ISSN: 1066-033X. DOI: 10.1109/37.184792.

Chunfang and Jian (May 2012). "Design of second-order sliding mode controller for Electromagnetic Levitation Grip used in CNC". In: *2012 24th Chinese Control and Decision Conference (CCDC)*, pp. 3282–3285. DOI: 10.1109/CCDC.2012.6244520.

Coelho, João Paulo, José Boaventura-Cunha, and Paulo B. de Moura Oliveira (2015). "Extended Stability Conditions for CDM Controller Design". In: *CONTROLO'2014 – Proceedings of the 11th Portuguese Conference on Automatic Control*. Ed. by António Paulo Moreira, Aníbal Matos, and Germano Veiga. Cham: Springer International Publishing, pp. 171–182. ISBN: 978-3-319-10380-8.

DS1007, dSPACE (2019). "DS1007". In: *https://www.dspace.com, accessed 6 April 2019*.

Erkan, K., B. Acarkan, and T. Koseki (May 2007). "Zero-Power Levitation Control Design for a 4-Pole Electromagnet on the Basis of a Transfer Function Approach". In: *2007 IEEE International Electric Machines Drives Conference*. Vol. 2, pp. 1751–1756. DOI: 10.1109/IEMDC.2007.383695.

Erkan, K., B. Okur, et al. (Apr. 2011). "Experimental evaluation of zero-power levitation control by transfer function approach for a 4-pole hybrid electromagnet". In: *2011 IEEE International Conference on Mechatronics*, pp. 23–28. DOI: 10.1109/ICMECH.2011.5971299.

Erkan and Koseki (Mar. 2006). "Fuzzy model based nonlinear control of an active oscillation suppression system comprised of mechanically flexible elements and triple configuration of u-shaped electromagnets". In: *9th IEEE International Workshop on Advanced Motion Control, Istanbul, Turkey*.

Erkan, Yalçın, and Garip (2017). "Three-axis gap clearance I-PD controller design based on coefficient diagram method for 4-pole hybrid electromagnet". In: *Automatika* 58.2, pp. 147–167. DOI: 10.1080/00051144.2017.1382649. URL: https://doi.org/10.1080/00051144.2017.1382649.

Ertugrul and Erkan (May 2016). "First order integral sliding mode control of the magnetically levitated 4-pole type hybrid electromagnet". In: *International Conference on Engineering and Natural Sciences (ICENS), Sarajevo, Bosnia and Herzegovina*.

Hakan Yazici Rahmi Guclu, Ibrahim B. Kucukdemiral and M. N. Alpaslan Parlakci (2012). "Robust Delay-Dependent $\mathcal{H}_\infty$ Control for Uncertain Structural Systems With Actuator Delay". In: *Journal of Dynamic Systems, Measurement, and Control* 11.1-4, pp. 625–653. DOI: http://dx.doi.org/10.1115/1.4005500.

Hamamci, S. E. and M. Koksal (June 2003). "Robust controller design for TITO processes with coefficient diagram method". In: *Proceedings of 2003 IEEE Conference on Control Applications, 2003. CCA 2003*. Vol. 2, 1431–1436 vol.2. DOI: 10.1109/CCA.2003.1223224.

Hamamci, S. E. and A. Ucar (2002). "A robust model-based control for uncertain systems". In: *Transactions of the Institute of Measurement and Control* 24.5, pp. 431–445. DOI: 10.1191/0142331202tm065oa.

Hoque et al. (2011). "A three-axis vibration isolation system using modified zero-power controller with parallel mechanism technique". In: *Mechatronics* 21.6, pp. 1055–1062. ISSN: 0957-4158. DOI: https://doi.org/10.1016/j.mechatronics.2011.05.002.

Jiangheng and Koseki (2001). "3 degrees of freedom control of semi-zero-power magnetic levitation suitable for two-dimensional linear motor". In: *Proceedings of the Fifth International Conference on Electrical Machines and Systems, ICEMS, Shenyang, China*.

Koksal, M. and S. E. Hamamci (June 2003). "Robust temperature control of MSF desalination plants with coefficient diagram method". In: *Proceedings of 2003 IEEE Conference on Control Applications, 2003. CCA 2003*. Vol. 2, 1437–1442 vol.2. DOI: 10.1109/CCA.2003.1223225.

Kumar, A and V Kumar (Oct. 2015). "Performance analysis of Interval Type-2 FSM controller applied to a magnetic levitation system". In: *International Conference on Soft Computing Techniques and Implementations (ICSCTI), Faridabad, India*.

Liu, Chunchuan et al. (2015). "Recent advances in micro-vibration isolation". In: *Mechanical Systems and Signal Processing* 56-57, pp. 55–80. ISSN: 0888-3270. DOI: `https://doi.org/10.1016/j.ymssp.2014.10.007`.

Liu et al. (2000). "3 Degrees of Freedom Control Zero-Current Magnetic Levitation for Flexible Transport System". In: *The 16th International Conference on Magnetically Levitated Systems and Linear Drives, Rio de Janeiro, Brazil*.

Lofberg, J. (2004). "YALMIP : a toolbox for modeling and optimization in MATLAB". In: *2004 IEEE International Conference on Robotics and Automation (IEEE Cat. No.04CH37508)*, pp. 284–289. DOI: `10.1109/CACSD.2004.1393890`.

Md. Emdadul Hoque Takeshi Mizuno, Yuji Ishino and Masaya Takasaki (2010). "A six-axis hybrid vibration isolation system using active zero-power control supported by passive weight support mechanism". In: *Journal of Sound and Vibration* 329.17, pp. 3417–3430. ISSN: 0022-460X. DOI: `https://doi.org/10.1016/j.jsv.2010.03.003`.

Micro-Epsilon (2019). "DT3001-U4M-SA". In: *https://www.micro-epsilon.com/download/manuals/ass–eddyNCDT-3001-U4–en.pdf, accessed 6 April 2019*.

Mizuno, Takeshi et al. (2007). "Vibration isolation system combining zero-power magnetic suspension with springs". In: *Control Engineering Practice* 15.2, pp. 187–196. ISSN: 0967-0661. DOI: `https://doi.org/10.1016/j.conengprac.2006.06.001`.

Nath, Samantaray, and Chaudhury (June 2015). "Magnetic ball levitation system control using sliding mode control and fuzzy PD+I control: a comparative study". In: *International Conference on Energy, Power and Environment: Towards Sustainable Growth (ICEPE), Shillong, India*.

Nesterov, Y. and A. Nemirovskii (1994). *Interior-Point Polynomial Algorithms in Convex Programming*. Society for Industrial and Applied Mathematics. DOI: `10.1137/1.9781611970791`.

NTComponents (2019). "LEM LTS 25-NP". In: *http://www.ntcomponents.com/Part-Detail/LTS25-NP/1/3212860.html, accessed 6 April 2019*.

PADT, Inc, Eric Miller, and Jeff Strain (2016). *Introduction to the ANSYS Parametric Design Language (APDL) - Second Edition*. 2nd. USA: CreateSpace Independent Publishing Platform. ISBN: 1537133993, 9781537133997.

Raja, C. V. N. et al. (2015). "Design and analysis of position controlled eddy current based nonlinear magnetic levitation system using LMI". In: *2015 International Conference on Control Communication Computing India (ICCC)*, pp. 137–142. DOI: `10.1109/ICCC.2015.7432882`.

Rodriguez, H., H. Siguerdidjane, and R. Ortega (Sept. 2000). "Experimental comparison of linear and nonlinear controllers for a magnetic suspension". In: *Proceedings of the 2000. IEEE International Conference on Control Applications. Conference Proceedings (Cat. No.00CH37162)*, pp. 715–719. DOI: `10.1109/CCA.2000.897518`.

Rosu, M. et al. (2018). "IEEE Press Series on Power Engineering". In: *Multiphysics Simulation by Design for Electrical Machines, Power Electronics and Drives*. IEEE. ISBN: 9781119103462. DOI: `10.1002/9781119103462.oth`. URL: `https://ieeexplore.ieee.org/document/8233737`.

Sarmad, M. et al. (Jan. 2016). "Sampled data robust control for a magnetic levitation system — Some practical considerations". In: *2016 13th International Bhurban*

Conference on Applied Sciences and Technology (IBCAST), pp. 154–160. DOI: 10.1109/IBCAST.2016.7429870.

Shahadat, M. M. Z. et al. (2010). "Active horizontal suspension system using negative stiffness control". In: *ICCAS 2010*, pp. 1946–1951.

Singh, B. and V. Kumar (Oct. 2015). "A real time application of model reference adaptive PID controller for magnetic levitation system". In: *2015 IEEE Power, Communication and Information Technology Conference (PCITC)*, pp. 583–588. DOI: 10.1109/PCITC.2015.7438065.

Sturm, Jos F. (1999). "Using SeDuMi 1.02, A Matlab toolbox for optimization over symmetric cones". In: *Optimization Methods and Software* 11.1-4, pp. 625–653. DOI: 10.1080/10556789908805766.

Su and Li (Mar. 2016). "Supervisory fuzzy model control for magnetic levitation system". In: *IEEE 13th International Conference on Networking, Sensing, and Control (ICNSC), Mexico City, Mexico*.

Tascikaraoglu Kucukdemiral, Imura (2014). "Robust Moving Horizon Control of Discrete Time-Delayed Systems with Interval Time-Varying Delays". In: *Mathematical Problems in Engineering* 2014. DOI: https://doi.org/10.1155/2014/462983.

TE (2019). "TE Connectivity 4020". In: *https://www.te.com/usa-en/product-CAT-PPA0052.html, accessed 6 April 2019*.

Ucar, A. and S. E. Hamamci (Dec. 2000). "A controller based on coefficient diagram method for the robotic manipulators". In: *ICECS 2000. 7th IEEE International Conference on Electronics, Circuits and Systems (Cat. No.00EX445)*. Vol. 2, 777–780 vol.2. DOI: 10.1109/ICECS.2000.912992.

Unni et al. (2016). "PID, fuzzy and LQR controllers for magnetic levitation system". In: *International Conference on Cogeneration, Small Power Plants and District Energy (ICUE), Bangkok, Thailand*.

Verma, S. K., S. Yadav, and S. K. Nagar (Dec. 2015). "Optimal fractional order PID controller for magnetic levitation system". In: *2015 39th National Systems Conference (NSC)*, pp. 1–5. DOI: 10.1109/NATSYS.2015.7489095.

Wang, M., M.O.T. Cole, and P.S. Keogh (2017). "New LMI based gain-scheduling control for recovering contact-free operation of a magnetically levitated rotor". In: *Mechanical Systems and Signal Processing* 96, pp. 104–124. ISSN: 0888-3270. DOI: https://doi.org/10.1016/j.ymssp.2017.04.008.

Yakushi, Koseki, and Sone (2000). "3 degree-of-freedom zero power magnetic levitation control by a 4-pole type electromagnet". In: *International Power Electronics Conference, Tokyo, Japan*.

Yalçın, Sever, and Erkan (2018). "Observer-based $\mathcal{H}_2$ controller design for a vibration isolation stage having hybrid electromagnets". In: *Journal of Low Frequency Noise, Vibration and Active Control* 37.4, pp. 1134–1150. DOI: 10.1177/1461348418782170.

Zhang, Xian, and Ma (Sept. 2015). "Continuous Robust Tracking Control for Magnetic Levitation System With Unidirectional Input Constraint". In: *IEEE Transactions on Industrial Electronics* 62.9, pp. 5971–5980. DOI: 10.1109/TIE.2015.2434791.

Zhu, Tao et al. (2015). "Vibration isolation using six degree-of-freedom quasi-zero stiffness magnetic levitation". In: *Journal of Sound and Vibration* 358, pp. 48–73. ISSN: 0022-460X. DOI: https://doi.org/10.1016/j.jsv.2015.07.013.

Publications From the Thesis

Contact Information: bariscanyalcin@gmail.com

Papers

1. Yalçın BC, Sever M, Erkan K "Observer-based $\mathcal{H}_2$ controller design for a vibration isolation stage having hybrid electromagnets", JOURNAL OF LOW FREQUENCY NOISE, VIBRATION AND ACTIVE CONTROL, vol.37(4), 2018. DOI : 10.1177/1461348418782170.

Conference Papers

1. Yalçın BC, Bozkurt AF, Erkan K, "Experimental Validation of Linear Matrix Inequality based $\mathcal{H}_2$ Full State Feedback Controllers on a 3-DoF 4-Pole Hybrid Electromagnetic Vibration Isolation Stage", IEEE Mechatronics 2019, 18-20 March 2019, ILMENAU, GERMANY.

Projects

1. Design and Control of 3-DOF Vibration Isolation Stage Using Hybrid Electromagnetic Levitation, Research Fund of YTU, Project Number FDK-2018-3250.

Awards

1. European Embedded Control Institute - Overseas PhD Student Grant, 2017, Paris, France.

2. European Embedded Control Institute - Overseas PhD Student Grant, 2019, Paris, France.